

Anisotropic EEG/MEG volume conductor modeling based on Diffusion Tensor Imaging

**Dissertation
Zur Erlangung des akademischen Grades
Doktoringenieur (Dr.-Ing.)**

**vorgelegt der Fakultät für Informatik und Automatisierung
der Technischen Universität Ilmenau**

**von Dipl.-Ing. Daniel Güllmar
geboren am 10. Juli 1976 in Sondershausen**

Tag der Einreichung: 2. Mai 2008

Tag der wissenschaftlichen Aussprache: 21. Juli 2008

Gutachter: 1. Prof. Dr.-Ing. habil. Jens Haueisen
 2. Prof. Dr. rer. nat. med. habil. Jürgen R. Reichenbach
 3. Dr.-Ing. Thomas Knösche

urn:nbn:de:gbv:ilm1-2008000082

Zusammenfassung

Die vorliegende Arbeit befasst sich mit der Volumenleitermodellierung auf Basis der Finiten Elemente für EEG/MEG Untersuchungen unter Einbeziehung von Anisotropieinformation, die mit Hilfe der Magnetresonanzdiffusionstensorbildgebung (MR-DTI) gewonnen wurde. Im ersten Teil der Arbeit wurde der Einfluss unvollständig bestimmter Wichtungsparmter (b-Matrix) auf die zu rekonstruierenden Diffusionstensoren untersucht. Die Unvollständigkeit bezieht sich dabei auf die Tatsache, dass im Allgemeinen nur die starken Diffusionsgradienten zur Berechnung der b-Matrix herangezogen werden. Es wurde gezeigt, dass besonders bei Aufnahmen mit hoher räumlicher Auflösung der Anteil der Bildgradienten an der b-Matrix nicht mehr vernachlässigbar ist. Weiterhin wurde gezeigt, wie man die b-Matrizen korrekt analytisch bestimmt und damit einen systematischen Fehler vermeidet. Für den Fall, dass nicht ausreichend Informationen zur Verfügung stehen um die analytische Bestimmung durchzuführen, wurde eine Lösung vorgeschlagen, die es mit Hilfe von Phantommessungen ermöglicht eine parametrisierte b-Matrix zu bestimmen. Der zweite Teil widmet sich der Erstellung hochaufgelöster realistischer Volumenleitermodelle detailliert beschrieben. Besonders die Transformation der Diffusionstensordaten in Leitfähigkeitstensoren. Zudem wurde eine Vorgehensweise beschrieben, die es erlaubt, einen T1-gewichteten MR-Datensatz vollautomatisch in fünf verschiedene Gewebesegmente (weiches Gewebe, graue und weiße Substanz, CSF und Schädelknochen) zu unterteilen. Der dritte Teil der Arbeit befasst sich mit dem Einfluss der anisotropen Leitfähigkeit in der weißen Hirnsubstanz auf EEG und MEG unter Verwendung eines Tier- sowie eines Humanmodells. Um den Einfluss der verschiedenen Methoden der Transformation von DTI Daten in Leitfähigkeitsdaten zu untersuchen, wurden verschiedenen Modelle sowohl mit gemessener als auch mit künstlicher Anisotropie erstellt. In der Tiermodellstudie wurden EEG und in der Humanmodellstudie EEG und MEG Simulationen sowohl mit den anisotropen Modellen als auch mit einem isotropen Modell durchgeführt und miteinander verglichen. Dabei wurde gefunden, dass sowohl der topographische Fehler (RDM) als auch der Magnitudenfehler stark durch das Einbeziehen von Anisotropieinformationen beeinflusst wird. Es wurde auch gezeigt, dass sowohl die Position als auch die Orientierung einer dipolaren Quelle in Bezug auf das anisotrope Segment einen großen Effekt auf die untersuchten Fehlermaße hat.

Abstract

In this work anisotropic electric tissue properties determined by means of diffusion tensor imaging were modeled into high resolution finite element volume conductors. In first part of the work the influence of not considering imaging gradient in the calculation of the b-matrices on the correct determination of diffusion tensor data is shown and it was found that especially with high resolution imaging protocols the contributions of the imaging gradients is not negligible. It was also shown how correct b-matrices considering all applied gradients can be calculated correctly. For the case that information about the sequence are missing an experimental approach of determining a parameterized b-matrix using phantom measurements is proposed. In the second part the procedure of generating anisotropic volume conductor models is regarded. The main focus of this part was to facilitate the derivation of anisotropy information from DTI measurements and the inclusion of this information into an anisotropic volume conductor. It was shown, that it is possible to generate a sophisticated high resolution anisotropic model without any manual steps into five different tissue layers. The third part studied the influence of anisotropic white matter employing an animal as well as a human model. To compare the different ways of converting the anisotropy information from DTI into conductivity information, different models were investigated, having artificial as well as measured anisotropy. In the animal study the EEG and in the human study the EEG and MEG forward solution was studied using the anisotropic models and compared to the solution derived using an isotropic model. It was found that both, the topography error (RDM) as well as the magnitude error (MAG), are significantly affected if anisotropy is considered in the volume conductor. It was also shown, that the position as well as the orientation of the dipole with respect to white matter has a large effect on the amount of the error quantities. Finally, it is claimed that if one uses high resolution volume conductor models for EEG/MEG studies, the anisotropy has to be considered, since the average error of neglecting anisotropy is larger than the accuracy which can be achieved using such models.

Abbreviations

ADC	apparent diffusion coefficient
AP	anterior-posterior
BEM	boundary element method
BET	brain extraction tool
CDI	current density imaging
CNS	central nervous system
CSF	cerebrospinal fluid
DTI	diffusion tensor imaging
ECD	equivalent current dipole
ECoG	cortical electroencephalogram
EEG	electroencephalography / electroencephalogram
EIT	electric impedance tomography
EPI	echo planar imaging
EPT	electric property tomography
FA	fractional anisotropy
FE	finite element
FEM	finite element method
FOV	field of view
GM	gray matter
IS	inferior-superior
LR	left-right
MAG	magnitude difference
MC	magnitude change
MEG	magnetoencephalography / magnetoencephalogram
MPRAGE	magnetization prepared rapid gradient echo
MRI	magnetic resonance imaging
NMR	nuclear magnetic resonance
PFG	pulsed field gradient
PGSE	pulsed gradient spin echo
RA	relative anisotropy
RDM	relative difference measure

SEP	somatosensory evoked field
SEP	somatosensory evoked potential
SL	slice thickness
SQUID	super-conducting quantum interference device
TA	acquisition time (duration)
TE	echo time
TR	repetition time
TRSE	twice refocusing spin echo
VR	volume ratio
WM	white matter

Contents

1. Introduction	3
1.1. History of brain research	3
1.2. Anatomy and physiology of the human brain	5
1.3. Electro- and magnetoencephalography	8
1.3.1. Electroencephalography (EEG)	8
1.3.2. Magnetoencephalography (MEG)	10
1.3.3. EEG/MEG topography and imaging	11
1.4. Anatomical and functional magnetic resonance imaging	12
1.5. Scope of the thesis	15
2. MRI of diffusion	17
2.1. Basic principles of magnetic resonance imaging	17
2.1.1. Spin and magnetic moment	17
2.1.2. Spatial encoding	21
2.2. Diffusion and nuclear magnetic resonance	23
2.2.1. Observing diffusion by using magnetic field gradients	23
2.2.2. Correlating signal attenuation with diffusion	26
2.3. The b-matrix	30
2.3.1. b-Matrix calculation	30
2.3.2. Experimental estimation of cross-term errors	40
2.4. Diffusion tensor imaging	50
2.4.1. MR diffusion weighted sequences	50
2.4.2. Determination of the diffusion tensor	52
2.4.3. Scalar measures	54
3. Volume conductor modeling	57
3.1. Introduction	57
3.2. Measurement of tissue conductivity	58
3.2.1. Invasive methods	58
3.2.2. Non-invasive methods	59
3.3. Effective medium approach	60

3.4. Volume conductor construction	64
3.4.1. MRI data segmentation	64
3.4.2. Spatial coregistration	68
3.4.3. FE mesh generation	70
3.4.4. Conductivity tensor preparation	71
4. EEG/MEG FEM-Simulations	73
4.1. Introduction	73
4.1.1. General approach	73
4.1.2. The electric forward problem	74
4.1.3. The magnetic forward problem	75
4.1.4. The lead-field approach	75
4.1.5. The inverse procedure	76
4.1.6. Simulations studies	77
4.2. Sensitivity analysis using a rabbit head model	77
4.2.1. Objectives	77
4.2.2. Material and methods	78
4.2.3. Results	84
4.2.4. Discussion	92
4.3. Sensitivity analysis using a human head model	95
4.3.1. Objectives	95
4.3.2. Material and Methods	96
4.3.3. Results	101
4.3.4. Discussion	113
5. Conclusion and Outlook	121
List of Tables	139
List of Figures	141
A. Appendix	I

1. Introduction

1.1. History of brain research

A long time ago people started to investigate the most complex part of the body - the brain - which controls the Central Nervous System (CNS) and virtually regulates all human activity. It contains some one hundred billion neurons, which are capable of electrical and chemical communication with tens of thousands of other nerve cells, which in turn rely on some quadrillion synaptic connections for their communication [1].

The earliest record of the word *brain* is dated to the 17th century BC - the Edwin Smith's Surgical Papyrus [2] (Fig. 1.1), which describes the symptoms, diagnosis, and prognosis of patients wounded in the head.



Fig. 1.1.: Plates vi and vii of the Edwin Smith Papyrus, the first known occurrence of the word *brain*.

In the second half of the first millennium BC, the Ancient Greeks developed different views of the function of the brain and it is said that they were the first who considered the brain to be the place where the mind is located [3]. While Hippocrates (460–370 B.C.) believed the brain to be the seat of intelligence, Aristotle thought that, while the heart was the seat of intelligence, the brain was a cooling mechanism for the blood [4].

1. Introduction

During the Roman Empire, the Greek anatomist Galen of Pergamon (129–201 A.D.) dissected the brains of sheep, monkeys, dogs, swine, among other non-human mammals [3]. He concluded that, as the cerebellum was more dense than the brain, it must control the muscles, while as the cerebrum was soft, it must be where the senses were processed. Galen further theorized that the brain functioned by movement of fluids through the ventricles [4]. Galen’s writings on anatomy were the mainstay of the medieval physician’s university curriculum, but they had suffered greatly from stasis and intellectual stagnation.

In the 1530s, however, Belgian anatomist and physician Andreas Vesalius (1514–1564) took on a project to translate many of Galen’s Greek texts into Latin. Vesalius’s most famous work, *De humani corporis fabrica* (1543), was greatly influenced by Galen’s writing and form (Fig. 1.2). Seeking to revive Galen’s methods and outlook, Vesalius turned to human cadaver dissection as an evolution of Galen’s natural philosophy. Galen’s writings enjoyed a revival at the hands of Vesalius, who promoted Galen and expounded on him through books and hands-on demonstrations [5]. The work of Vesalius also corrected Greek medical errors and revolutionized medicine.

In the beginning of the 17th century great progress was made in describing the anatomy of the human brain. Besides Vesalius, especially Thomas Willis (1621–1675) contributed with his work *Cerebri anatomi* (1664), which was the first separate work on anatomy of the nervous system. In the subsequent centuries most macroscopic structures were termed like *pons varoli* (Constanzo Varolio, 1543–1575), a structure located in the brain stem, *lateral sulcus* or *Sylvian fissure* (Franciscus Sylvius, 1614–1672), one of the most prominent structures, which divides the frontal lobe and parietal lobe above from the temporal lobe below, or *interventricular foramina* (Alexander Monro secundus, 1733–1817), the channels, which connect the two lateral ventricles with the third ventricle.

In the 18th century the exploration of microscopic structures started and people like Johannes Evangelista Purkinje (1787–1869) discovered the cerebellar Purkinje cells, one of the largest neurons in the human brain. In 1840 Jules G. F. Baillarger (1809–1890) was the first physician, who discovered that the cerebral cortex was divided into six layers of alternate white and gray laminae and in 1837, Theodor Schwann (1810–1882) developed the cell theory [6]. This theory accepted the first two tenets of modern cell



Fig. 1.2.: Cover picture of Vesalius’ *De humani corporis fabrica* (1543).

theory – (1) *every living body is essentially a mass of cellular tissue* [7] and (2) *the cell is the fundamental element of organization* [8].

In all epochs of great advances in neurological research a preceding advance in technology can be recognized. Despite the long history of brain research, the tools, which were used in the past, are still used like surgical instruments or the microscope; however, new tools are developed to discover more than we already know. Actually, we are in the computer era and the basics of brain anatomy from macro to micro are well known, as are the elementary neuronal cell functions. However, the complex connections of macroscopic and microscopic anatomy and their functions are still not completely understood. Computers are nowadays used to investigate the higher functions of the human brain including the cortical network and to understand healing processes and pathologies. Some anatomic and physiological facts of the human brain are briefly described in the next section.

1.2. Anatomy and physiology of the human brain

The brain, which is the largest part of the human head, is seated in the skull. Between brain and bone we find the *meninges*, a system of membranes which envelops the central nervous system. The meninges consist of three layers: the *dura mater*, the *arachnoid mater*, and the *pia mater* (from outside to inside). The primary function of the meninges and of the cerebrospinal fluid (CSF), which occupies the space between pia and arachnoid mater, is to protect the central nervous system. The dura mater is coadunated at the sutures, immovable joints formed by bony ossification, with Sharpey's fibres permitting some flexibility. The skull is covered by scalp, which is usually described as having five layers, which can be remembered with the mnemonic "SCALP". The skin on the head from which head hair grows, the connective tissue, a thin layer of fat and fibrous tissue which lies beneath the skin, the aponeurosis (or galea aponeurotica), a tough layer of dense fibrous tissue which runs from the frontalis muscle anteriorly to the occipitalis posteriorly, the loose areolar connective tissue layer which provides an easy plane of separation between the upper three layers and the pericranium. The latter is the periosteum of the skull bones and provides nutrition to the bone and the capacity for repair.

The bulbous cerebral cortex is composed of convoluted grey matter internally supported by deep brain white matter. The two hemispheres of the brain are separated by a prominent central fissure and are connected to each other by the corpus callosum. The cerebellum is found at the back of the brain. Brain stem structures are almost completely enveloped by the cerebellum and telencephalon, with the medulla oblongata projecting through the foramen magnum to merge with the spinal cord. The brain is

1. Introduction

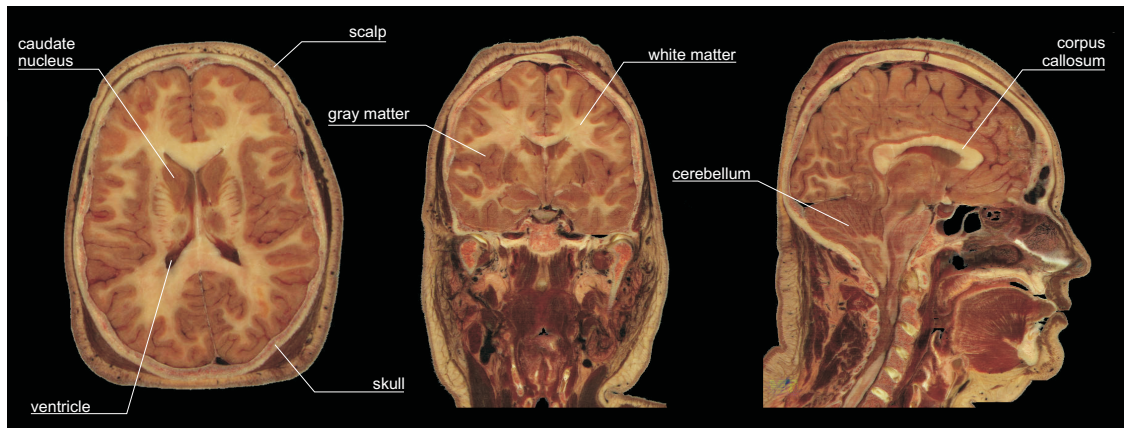


Fig. 1.3.: Axial, coronal and sagittal sections of a human head - visible human dataset.

suspended in cerebrospinal fluid (CSF), which also fills spaces called ventricles inside it. The dense fluid protects the brain and spinal cord from shock. Fluid movement within the brain is limited by the blood-brain barrier and the blood-cerebrospinal fluid barrier.

The blood supply to the brain involves the paired carotid arteries that enter the brain and communicate in the circle of Willis before branching out to their destinations. Further blood supply comes via the vertebral arteries. Blood drains from the brain through a network of sinuses that drain into the right and left internal jugular veins.

The two main tissue types in the human brain – white and gray matter – consist for the most part of neurons. While neurons in the gray matter are unmyelinated, neurons in white matter are coated by an electrically insulating phospholipid layer – myelin. Myelinated neurons are white in appearance, hence the "white matter" of the brain. The main consequence of a myelin layer is an increase in the speed at which impulses propagate along the myelinated fiber. Along unmyelinated fibers, impulses move continuously as waves, but, in myelinated fibers, they hop or "propagate by saltation". Myelin increases resistance across the cell membrane by a factor of 5,000 and decreases capacitance by a factor of 50. Myelination also helps to prevent the electrical current from leaving the axon. When a peripheral fiber is severed, the myelin sheath provides a track along which regrowth can occur. Unmyelinated fibers and myelinated axons of the mammalian central nervous system do not regenerate.

The neurons are electrically excitable cells in the nervous system that process and transmit information. Neurons are typically composed of a soma, or cell body, a dendritic tree and an axon (cf. Figure 1.4). The majority of vertebrate neurons receive input on the cell body and dendritic tree, and transmit output via the axon. The communication between the neurons operates via chemical and electrical synapses, in a

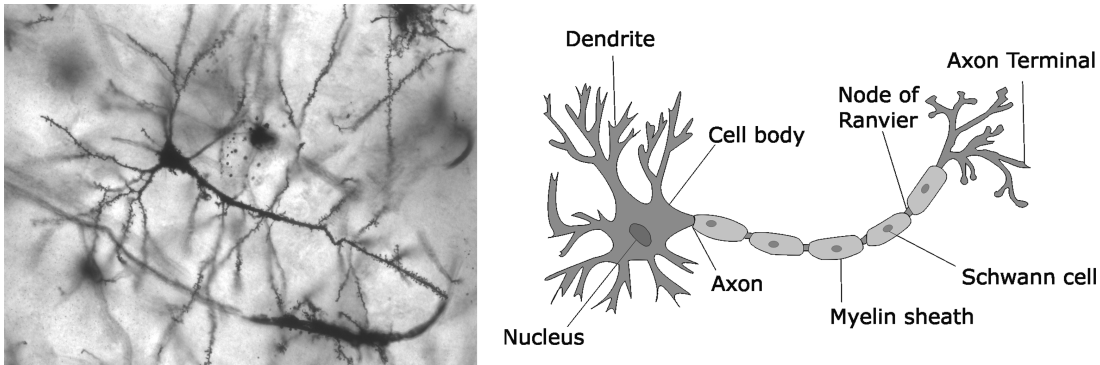


Fig. 1.4.: Golgi stained pyramidal neuron in the hippocampus of an epileptic patient, 40x magnification [9] (left). Structure of a typical neuron (right)

process known as synaptic transmission, or neurotransmission. When a nerve impulse arrives at the synapse, it releases neurotransmitters, which influence another neuron, either in an inhibitory way or in an excitatory way. This next neuron is connected to many more neurons, and if the total of excitatory influences is more than the inhibitory influences, it will also "fire", that is, it will create a new action potential at its axon hillock, in this way passing on the information to yet another next neuron, or resulting in an experience or an action. Action potentials are triggered when an initial depolarization reaches the threshold. This threshold potential varies, but generally is about 15 millivolts more positive than the cell's resting membrane potential, occurring when the inward sodium current exceeds the outward potassium current.

In unmyelinated axons, action potentials propagate as an interaction between passively spreading membrane depolarization and voltage-gated sodium channels. When one patch of cell membrane is depolarized enough to open its voltage-gated sodium channels, sodium ions enter the cell by facilitated diffusion. Once inside, positively-charged sodium ions "nudge" adjacent ions down the axon by electrostatic repulsion (analogous to the principle behind Newton's cradle) and attract negative ions away from the adjacent membrane. As a result, a wave of positivity moves down the axon without any individual ion moving very far. Once the adjacent patch of membrane is depolarized, the voltage-gated sodium channels in that patch open, regenerating the cycle. The process repeats itself down the length of the axon, with an action potential regenerated at each segment of membrane.

Action potentials propagate faster in axons of larger diameter, other things being equal. They typically travel with conducting speeds ranging from 10–100 m/s. The main reason is that the axial resistance of the axon lumen is lower with larger diameters, because of an increase in the ratio of cross-sectional area to membrane surface area. As the membrane surface area is the key factor impeding action potential propagation in an unmyelinated axon, increasing this ratio is a particularly effective way of increasing

1. Introduction

conduction speed.

An extreme example of an animal using axon diameter to speed action potential conduction is found in the Atlantic squid. The squid giant axon controls the muscle contraction associated with the squid's predator escape response. This axon can be more than 1 mm in diameter, and is presumably an adaptation to allow very fast activation of the escape behavior. The velocity of nerve impulses in these fibers is among the fastest in nature. Squids are notable examples of organisms with unmyelinated axons; the first experiments to determine the mechanism by which impulses travel along axons, involving the detection of a potential difference between the inside and the surface of a neuron, were undertaken in the 1940s by Alan Hodgkin and Andrew Huxley using squid giant axons because of their relatively large axon diameter. Hodgkin and Huxley won the 1963 Nobel Prize in Physiology or Medicine for their work on the electrophysiology of nerve action potentials.

In the autonomic nervous system in mammals, postganglionic neurons are unmyelinated. The small diameter of these axons (about $2\text{ }\mu\text{m}$) results in a propagatory speed of approximately 1 m/s , as opposed to approximately 18 m/s in myelinated nerve fibers of comparable diameter, thus highlighting the effect of myelination on the speed of transmission of impulses.

Overall the anatomic structures of the head and especially of the brain and their physiology are very complex and it is necessary to employ more than a single technique to investigate the complex scenario. A single action potential for example can be measured with the recording techniques of electrophysiology, whereas postsynaptic potentials from a large number of neurons can be measured by means of Electro- and Magnetocencephalography (EEG/MEG). However, in order to describe the source of the postsynaptic "firing" measured by EEG and/or MEG, it is necessary to have knowledge of the underlying anatomy, which always differs from subject to subjects. Hence, imaging methods like magnetic resonance imaging (MRI) have to be used in addition.

1.3. Electro- and magnetoencephalography

1.3.1. Electroencephalography (EEG)

Richard Caton (1842–1926), a physician practicing in Liverpool, presented his findings about electrical phenomena of the exposed cerebral hemispheres of rabbits and monkeys in the British Medical Journal in 1875. In 1890, Beck published an investigation of spontaneous electrical activity of the brain of rabbits and dogs which included rhythmic oscillations altered by light. In 1912, Russian physiologist, Vladimir Vladimirovich Pravdich-Neminsky published the first EEG and the evoked potential of

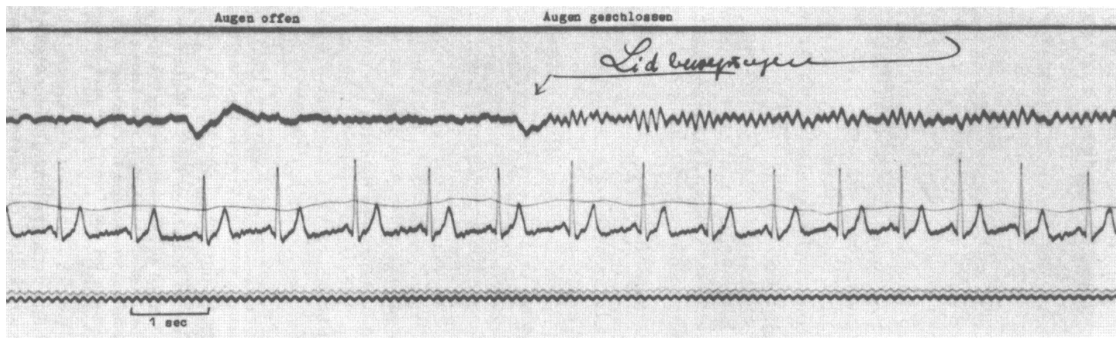


Fig. 1.5.: EEG registration by Hans Berger from 1928, one year before his first publication about EEG [11].

the mammalian (dog) [10]. In 1914, Cybulsky and Jelenska-Macieszyna photographed EEG-recordings of experimentally induced seizures. German physiologist Hans Berger (1873–1941) began his studies of the human EEG in 1920. He gave the device its name and is sometimes credited with inventing the EEG, though others had performed similar experiments. His work was later expanded by Edgar Douglas Adrian. In 1934, Fisher and Lowenback first demonstrated epileptiform spikes. In 1935 Gibbs, Davis and Lennox described interictal spike waves and the 3 cycles/s pattern of clinical absence seizures, which began the field of clinical electroencephalography. Subsequently, in 1936 Gibbs and Jasper reported the interictal spike as the focal signature of epilepsy. The same year, the first EEG laboratory opened at Massachusetts General Hospital. Franklin Offner (1911–1999), professor of biophysics at Northwestern University developed a prototype of the EEG which incorporated a piezoelectronic inkwriter called a Crystograph (the whole device was typically known as the Offner Dynograph). In the 1950s, English physician William Grey Walter developed an adjunct to EEG, called EEG topography which allowed for the mapping of electrical activity across the surface of the brain. This enjoyed a brief period of popularity in the 1980s and seemed especially promising for psychiatry.

In conventional scalp EEG, the recording is obtained by placing electrodes on the scalp with a conductive gel, usually after preparing the scalp area by light abrasion to reduce impedance. Electrode placement is accomplished by measuring the scalp. Electrode locations and names are specified by the international 10–20 system. This system ensures a system of placement that is reliable and reproducible. Although EEG is rarely used anymore as the primary method of localizing tumors, it is the primary method of localizing the onset of partial seizures.

1. Introduction

Each electrode is connected to one input of a differential amplifier (one amplifier per pair of electrodes); a reference electrode is connected to the other input of each differential amplifier. These amplifiers amplify the voltage between the active electrode and the reference (typically 1,000–100,000 times, or 60–100 dB of voltage gain). The resulting voltage signal is filtered by a high-pass filter and a low-pass filter, typically set at 0.5 Hz and 35–70 Hz, respectively. The high-pass filter typically filters out slow artifact, such as electrogalvanic signals, whereas the low-pass filter filters out high-frequency artifacts, such as electromyographic signals. An additional notch filter is typically used to remove artifact caused by electrical power lines. Since time dependent electric fields are accompanied by magnetic fields neuronal activity can also be measured using magnetoencephalography (MEG).

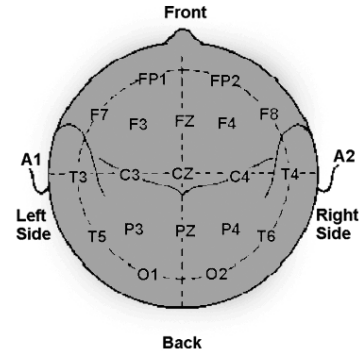


Fig. 1.6.: Illustration of international 10-20 system - top view.

1.3.2. Magnetoencephalography (MEG)

Magnetoencephalography (MEG) was first measured by David Cohen in 1968 [12], before the availability of the superconducting interference devices (SQUIDs), using a copper induction coil as the detector. To reduce the magnetic background noise, the measurements were performed in a magnetically shielded room. However, the insensitivity of this detector resulted in poor, noisy MEG signals, which were difficult to use. Then, later at Massachusetts Institute of Technology (MIT), he built a better shielded room, and used one of the first SQUID detectors (just developed by Zimmerman [13]) to again measure MEG [14]. This time the signals were almost as clear as the EEG, and stimulated the interest of physicists who had begun looking for uses of SQUIDs. Thus, the MEG entered the arena and various types of spontaneous and evoked MEG were measured.

At first only a single SQUID detector was used, to successively measure the magnetic field at a number of points around the subject's head. This was slow and cumbersome, and in the 1980's, MEG manufacturers began to increase the number of sensors in the dewar to cover a larger area of the head, using a correspondingly larger dewar. Present-day MEG dewars are helmet-shaped and contain as many as 300 sensors, covering most of the head. In this way, MEG of a subject or patient can now be acquired and accumulated rapidly and efficiently.

The MEG (and EEG) signals stem from the net effect of ionic currents flowing in the dendrites of neurons during synaptic transmission. In accordance with Maxwell's

equations, any electrical current will produce a magnetic field, which is oriented orthogonal to the electric field. It is this field which is measured with MEG. The net currents can be thought of as current dipoles which are currents defined to have an associated position, orientation, and magnitude, but no spatial extent. According to the right-hand rule, a current dipole gives rise to a magnetic field that flows around the axis of the dipole vector component.

In order to generate a signal that is detectable, approximately 50,000 active neurons are needed. Since current dipoles must have similar orientations to generate magnetic fields that reinforce each other, it is the layer of pyramidal cells in the cortex, which are oriented perpendicular to the brain surface, that give rises to measurable magnetic fields. Furthermore, it is often bundles of these neurons located in the sulci of the cortex with orientations parallel to the surface of the head that create measurable portions of their magnetic fields outside of the head. Researchers are investigating various signal processing methods to find ways that will allow detection of deep brain (i.e., non-cortical) signals, but as of yet there is no clinically useful method available currently.

Because the magnetic signals produced by the brain are on the order of a few femtoeslas ($1 \text{ fT} = 10^{-15} \text{ T}$), shielding from external magnetic signals, including the Earth's magnetic field, is necessary. An appropriate magnetically shielded room can be constructed of aluminum and *Mu*-metal (a nickel-iron alloy that has very high magnetic permeability) for reducing high-frequency and low-frequency noise, respectively. Moreover, noise cancellation algorithms can reduce both low-frequency and high-frequency noise. Modern systems have a noise floor of around 2 to $3 \text{ fT}/\sqrt{\text{Hz}}$ above 1 Hz.

1.3.3. EEG/MEG topography and imaging

EEG brain topography was invented by William Grey Walter, who, in 1936, proved that, by using a larger number of electrodes pasted to the scalp, each one having a small size, and a triangulation algorithm, it was possible to identify abnormal electrical activity in brain areas around a tumor, and diminished activity within the lesion. Impressed with the possibilities of building two-dimensional maps of EEG activity over the brain surface, Grey Walter invented the *toposcope* in 1951 [15]. This was a remarkably complex device and showed Grey Walter's impressive inventiveness and skills (besides being a physician, he was also an engineer). The toposcope projects electrical data visually on a spacial co-ordinate system using cathode ray tubes (similar to a TV tube), each of them connected to a pair of electrodes attached to the skull. The electrodes (and their corresponding tubes) were arranged in a two-dimensional geometrical array, such that each tube was able to depict the intensity of the several rhythms which compose the

1. Introduction

EEG in a particular area of the brain (the frontal, parietal and occipital lobes, etc.). This array of CRT tubes, were photographed face up, so that a kind of phosphorescent spiral display showed simultaneously which kind of rhythm was present in a particular part of the brain.

Besides describing the recorded surface potential or magnetic field pattern of multi-sensor acquisitions, it is also possible to reconstruct a dipolar source or equivalent current dipole (ECD). This procedure is known as EEG/MEG imaging and requires to solve the inverse problem. To solve the inverse problem involves repeated simulation of the field distribution in the head for a given dipole in the brain – the so-called forward problem. The forward problem, in turn, requires a known volume conductor, that should model the electromagnetic properties of the investigated subject as accurate as possible. In case of the human head the most simple volume conductor is a sphere or multi-layered spheres [16] [17], with the advantage that an analytic solution can be derived. To better take into account the shape of the scalp, skull and the convoluted brain, *Boundary Element Method* (BEM) head models were developed [18] [19] [20] [21]. With BEM models volume conductor properties are approximated by realistically shaped compartments of isotropic and homogeneous conductivities. The anisotropy and structure of the real tissue surrounding the electric sources to be reconstructed are neglected with these models. These effects can be treated by finite element methods (FEMs) [22] [23] [24], which, however, suffer from large computational effort. Nevertheless, the actual development in computer technology facilitates FEM calculations on standard computer hardware. As the name *volume conductor* implies, knowledge of tissue conductivities are necessary to generate such models. In the case of head modeling, tissue conductivities of usually five different types (scalp/skin, skull, csf, gray and white matter) have to be known. In general, conductivity values are taken from literature which were measured in-vivo or in-vitro in animals and humans by using invasive methods [25, 26, 27, 28]. Unfortunately, these values differ between various publications [29] and a method to measure conductivities in-vivo non-invasively is still unknown. The common way to generate realistic head models is to segment high resolution magnetic resonance volume scans to generate a mesh based on these segmented data.

1.4. Anatomical and functional magnetic resonance imaging

Magnetic resonance imaging (MRI) is a non-invasive method to acquire cross sections of an object. MRI is based on the principles of nuclear magnetic resonance (NMR), a spectroscopic technique used by scientists to obtain microscopic chemical and physical

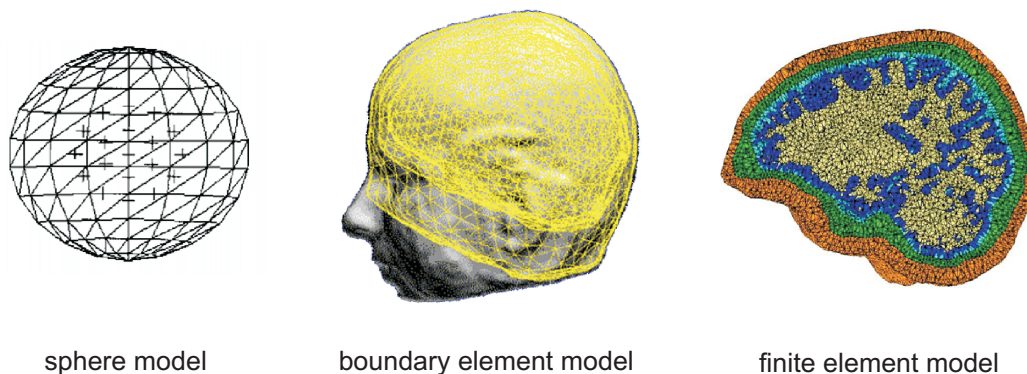


Fig. 1.7.: Different conductivity head models. From left to right: spherical model [30], BEM model and FEM model [31].

information about molecules. MRI started out as an imaging technique, that produces a spatially resolved map of the NMR signal in a thin slice through the human body. MRI has advanced beyond a tomographic imaging technique to a volume imaging technique.

The history of MRI starts with Felix Bloch and Edward Purcell, who were both awarded with the Nobel Prize in 1952 for discovering the magnetic resonance phenomenon independently in 1946. In the period between 1950 and 1970, NMR was developed and mainly used for chemical and physical molecular analysis. In 1971 Raymond Damadian showed that the nuclear magnetic relaxation times of tissues and tumors differed, thus motivating scientists to consider magnetic resonance for the detection of disease. In 1973 the X-ray-based computerized tomography (CT) was introduced by Hounsfield. Magnetic resonance imaging was first demonstrated on small test tube samples that same year by Paul Lauterbur [32]. He applied a back projection technique for image reconstruction similar to that used in CT. In 1975 Richard Ernst proposed magnetic resonance imaging using phase and frequency encoding, and the Fourier Transform [33]. This technique is the basis of current MRI techniques. A few years later, in 1977, Raymond Damadian demonstrated MRI based on the so-called field-focusing nuclear magnetic resonance. In this same year, Peter Mansfield developed the echo-planar imaging (EPI) technique [34], which was further improved in later years to produce images at video rates (30 ms/image).

Edelstein and coworkers demonstrated imaging of the body using Ernst’s technique in 1980. A single image could be acquired in approximately five minutes by this technique. By 1986, imaging time per slice was reduced to about five seconds, without sacrificing too much image quality. The same year researchers were developing the NMR microscope, which allowed approximately 10 mm resolution on approximately one cm-sized samples. In 1987 echo-planar imaging was used to perform real-time movie imaging of

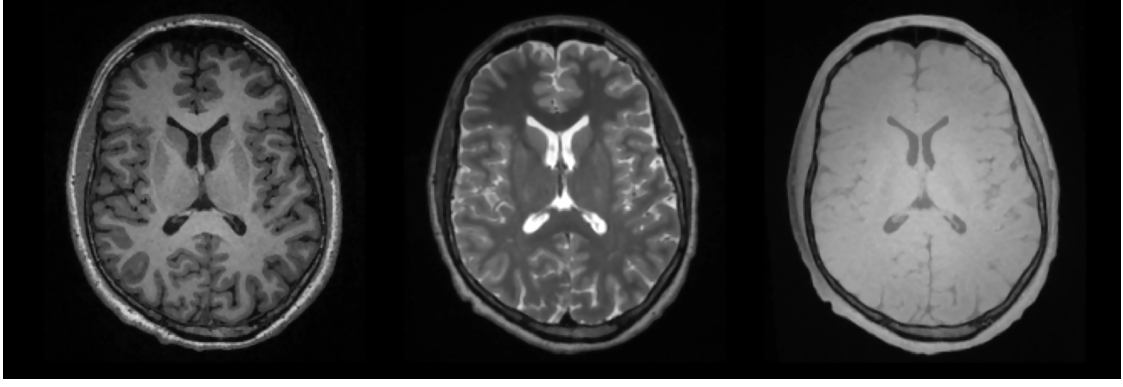


Fig. 1.8.: Axial slice acquired with T1, T2 and PD weighted MR imaging.

a single cardiac cycle [35]. In this same year Charles Dumoulin was perfecting magnetic resonance angiography (MRA), which allowed imaging of flowing blood without the use of contrast agents [36].

The basic concept of magnetic resonance imaging (MRI) uses three different types of magnetic fields: a homogeneous static field (B_0), a high frequency (rotating field (B_1)) and time-varying magnetic fields of controlled spatial non-uniformity (gradients fields). The static magnetic field is usually produced by an superconducting magnet and ranges from 0.5 up to 8 Telsa for human application and even up to 17 T for animal investigations.

If an object is placed into the magnetic field, the object is magnetized and the spins in this object can be excited by the high frequency B_1 field. After excitation two different relaxation processes occur - T1- and T2-relaxation. T1 relaxation refers to the processes which let the spins return to the thermodynamic equilibrium state in the magnet after excitation. The second relaxation process, T2, describes the evolution of the precessing spins after an RF-pulse. The measured signal depends on both relaxation processes, where by changing the echo time (TE, time from excitation until readout) and the repetition time (TR, time between two excitations) one is able to manipulate the contribution of the two processes and to tailor the image contrast between different tissue types. The spatial encoding is realized by additional linear gradient fields (x, y and z direction), which lead to resonance frequencies as a function of position. Based on these MR images it is possible to perform tissue segmentation, which in turn can be used to create realistic volume conductor models with BEM or FEM. With FEM, it is possible to include information on anisotropic tissue properties, however T1, T2 or PD weighted images do not provide any directional information about the tissue geometry.

The diffusion contrast in MRI is almost as old as the MR technique itself. In 1956 H.C. Torrey published a revised Bloch equation under conditions of inhomogeneity in

the magnetic field and considered the process of diffusion [37]. This revised equation provides also the basis for spatial encoding in MRI, however, its potential was not recognized at this time. Ten years later in 1965 E.O. Stejskal and J.E. Tanner [38] proposed a NMR experiment based on Torrey's work and demonstrated the possibility to quantify diffusivity by means of MR. The used pulse sequence is often referred to as *Stejskal-Tanner pulsed field gradient spin echo* (PFG-SE) sequence. In 1990 D. LeBihan was the first to show the usefulness of diffusion weighted imaging, especially for the detection of acute stroke [39]. Four years later he showed in collaboration with P.J. Basser and J. Mattiello [40], that it is possible to measure the diffusivity in different directions in order to obtain a diffusion tensor. This was the first MR technique which allowed to gain information about microscopic structures at a macroscopic scale and is nowadays known as diffusion tensor imaging (DTI). Based on this works, Tuch et al. [41, 42] proposed a cross-property relation between diffusion and conductivity tensor data, which can be used to generate anisotropic conductivity models, which may improve the quality of the forward solution in EEG/MEG experiments and solve recent problems in electromagnetic source imaging.

1.5. Scope of the thesis

The scope of this thesis is to model anisotropic electric tissue properties into high resolution finite element head models by means of diffusion tensor imaging and investigate the influence of neglecting or considering brain anisotropy in the head on the forward and inverse solution in EEG/MEG. The complete work is separated into three main parts. The first main part (chapter 2) covers the technique of diffusion weighted magnetic resonance imaging. Starting from the basic principles of magnetic resonance and diffusion weighted imaging, this chapter focuses on the exact calculation of diffusion tensor data. It is shown how the simplification (by only considering diffusion gradients) in determining the diffusion weighting or b-matrices influence the diffusion tensor calculation and how analytical and experimental correction can be applied.

The second part (chapter 3) addresses the generation of anisotropic volume conductor models. Starting with an overview of techniques to measure the conductivity of tissue in-vivo the procedure of obtaining anisotropic conductivity data from diffusion tensor data is shown in detail. This chapter also covers the approach of generating high resolution FEM head models step by step.

The third part (chapter 4) introduces the topic of sensitivity analysis. It describes how anisotropic conductivity influences the forward and inverse solutions in EEG and MEG experiments based on different simulations using animal and human head models with data derived from MRI acquisitions.

1. Introduction

2. MRI of diffusion

2.1. Basic principles of magnetic resonance imaging

2.1.1. Spin and magnetic moment

The fundamental property that enables MRI is spin. Spin is a more abstract property than for example electrical charge or mass, but is just as fundamental. All elementary particles, protons, electrons and neutrons, possess a spin. Individual unpaired elementary particles each possesses a spin of $\frac{1}{2}$. When different elementary particles together form an atom the resulting particle will have both an electronic spin and a nuclear spin. For instance, the deuterium atom, 2H , consisting of one unpaired electron, one unpaired proton and one unpaired neutron will have an electronic spin of $\frac{1}{2}$ and a ground state nuclear spin of 1. If two or more particles have spins with opposite signs they can pair up to eliminate the observable signs of spin. This is the case for helium, but almost every element in the periodic table has at least one isotope with a non-zero nuclear spin. To easier understand spin one can think of it as if the particle rotates around its own

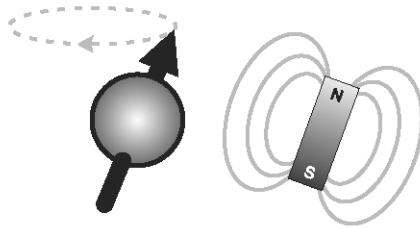


Fig. 2.1.: Nuclear spin causing the particle to behave like a tiny magnet.

axis. If the particle has an unpaired nuclear spin it causes the particle to behave like a tiny magnet with a north and south pole, see Fig. 2.1. This will generate a magnetic moment vector \vec{m} that is parallel to the rotation axis. The direction of this moment is usually randomly distributed so that the total magnetic moment average over many particles is zero, as can be seen schematically in Fig. 2.2. However, when a group of spins is placed in an external magnetic field the direction of each spin vector will be affected and the spins will align themselves with the external field, just like a magnet would. This is illustrated in Fig. 2.3 for the case of spin $\frac{1}{2}$. The spin vector will align

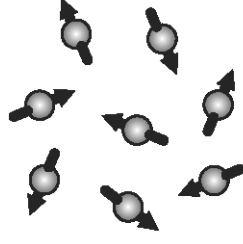


Fig. 2.2.: Randomly distributed spins with zero total magnetic moment.

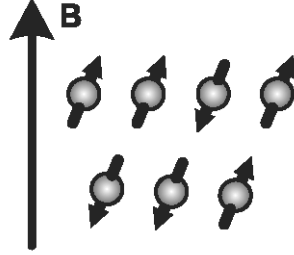


Fig. 2.3.: Spins aligned parallel or anti-parallel with the external magnetic field.

in one of two possible orientations, parallel or anti-parallel to the outer field, giving rise to a low energy state and a high energy state which are separated by an energy difference ΔE . According to the laws of thermal dynamics the number of spins in the lower energy level slightly outnumbers the number of spins in the upper level. The difference is very small, but significant and is given by Boltzmann statistics

$$\frac{N^-}{N^+} = e^{-\frac{\Delta E}{kT}} \quad (2.1)$$

where N^- represents the number of spins in the upper energy level, N^+ the number of spins in the lower energy level, k is Boltzmann's constant and T is the absolute temperature in Kelvin.

Transition

If the particles are placed in an external magnetic field B of strength B_0 , they can absorb a photon and undergo a transition between the two energy states. A particle in the lower energy level that absorbs a photon will end up in the upper energy level. However, not every photon can be absorbed by a particle. The energy of a photon must exactly match the energy difference between the two energy levels. The energy E of a photon is related to its frequency ν , by Planck's constant

$$E = h\nu \quad (2.2)$$

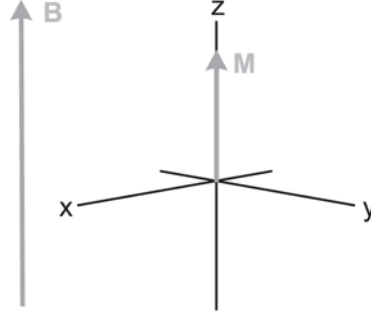


Fig. 2.4.: Net macroscopic magnetization pointing in the direction of the main magnetic field.

A particle with a net spin placed in the magnetic field of strength B_0 can absorb a photon of frequency ν if

$$\nu = \gamma B_0 \quad (2.3)$$

where γ is the gyromagnetic ratio, which is different for different types of particles. These two equations can be combined into one equation describing the energy of the photon needed to cause a transition between the two spin states

$$E = h\gamma B_0 \quad (2.4)$$

When the energy of a photon matches the energy difference ΔE between the two spin states, absorption of energy occurs. The frequency causing a transition between the two spin energy levels of a nucleus is called the Larmor frequency, or resonance frequency, and is characteristic for each nucleus.

Resonance

It is cumbersome to understand MRI on a microscopic scale. At a macroscopic level it is convenient to replace the individual spin vectors by a single magnetization vector representing the spin of all the particles experiencing the same external magnetic field strength. In an MRI scanner at room temperature there is approximately the same number of particles aligned with the external magnetic field B as counter aligned. The aligned state, i.e. the lower energy level, is favored with about one extra particle for every one-million compared to the high energy state. This results in a net or macroscopic magnetization M pointing in the direction of the main magnetic field B , as shown in Fig. 2.4. In MRI an RF (radio frequency) pulse, an oscillating magnetic field of appropriate frequency and duration, is applied to the sample (or body). This pulse is much weaker than the strong external magnetic field, B_0 . The exposure to the

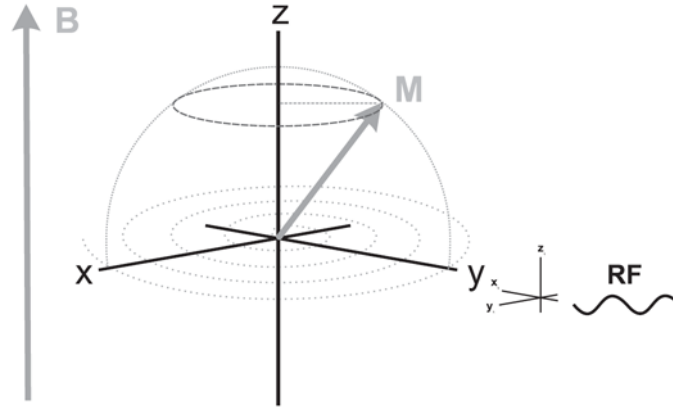


Fig. 2.5.: RF pulse applied through a rotating reference frame causing the net macroscopic.

RF pulse causes the net magnetization to spiral away from the strong B field. The magnetization vector, M , rotates from a longitudinal position, parallel to the z -axis, a distance proportional to the time length of the RF pulse. After a certain length of time, the net magnetization vector has rotated 90 degrees and will lie in the x - y plane, as illustrated in Fig. 2.5. The net magnetization also starts to dephase since different particles will experience a slightly different magnetic field. This is usually referred to as the dephasing.

Relaxation

When the RF pulse is removed, the particles begin to return to their natural alignment within the external magnetic field, i.e. from the upper to the lower energy state. This is associated with a loss of stored excess energy to surrounding particles, which in turn can be detected by a coil in the MRI scanner. In clinical MRI the RF pulse is typically chosen to coincide with the Larmor frequency of the hydrogen nucleus, the proton (hydrogen imaging). The energy release is then an estimate of the number of hydrogen nuclei, which in principle corresponds to the amount of water. The T_1 relaxation gives information on the chemical surrounding of the water and the T_2 relaxation reflects the surroundings of each individual atom, which gives a different contrast. With these variables it is possible to separate tissues since they will show different characteristics in T_1 and T_2 relaxation time. Images acquired using the different relaxation are usually called, respectively, T_1 weighted and T_2 weighted.

2.1.2. Spatial encoding

The transverse magnetization in NMR experiments is detected by using coils. The precessing magnetization vector acts like a tiny generator and induces a voltage in the receiving coil. The induced voltage amplitude is typically in the range of μV and proportional to the detected magnitude of the transverse magnetization. The magnitude of the magnetization and therefore of the received signal depends on the spin density which can further fluctuate spatially. Thus, the signal is a function of the position vector \vec{r} . However, in MRI the signal is received from the whole measuring volume not from single points which makes an integration over the volume necessary [43]:

$$S(t) = S_0 \cdot \int_V M_T(\vec{r}, t = 0) d\vec{r} \cdot e^{-i\gamma B_0 t} \cdot e^{-\frac{t}{T_2}} \quad (2.5)$$

where S_0 denotes the proportional factor between the magnetization and the signal. In order to obtain magnetic resonance images, it is necessary to know the location of the signal in the measured volume, in other words spatial encoding has to be applied. The encoding by linear field gradients produces spatial dependent resonance frequencies. These linear magnetic field gradients are created by three orthogonal gradient coils and are commonly specified by their function into slice selection, phase and frequency encoding gradients, respectively.

Slice selection

The first step toward spatial encoding is to apply a linear gradient, say in z-direction, and an RF excitation pulse with a certain bandwidth and amplitude simultaneously. The magnitude and duration of the RF-pulse controls the angle by which the magnetization is tipped out of the z-direction, and is known as flip angle. In the presence of this gradient the resonance frequency becomes spatial dependent along the z-axis with

$$\omega(z) = \omega_0 + \gamma G_z z \quad (2.6)$$

The slice thickness $\Delta z = |z_1 - z_2|$ is then defined by

$$\Delta z = \frac{|\omega(z_1) - \omega(z_2)|}{\gamma G_z} = \frac{\Delta \omega}{\gamma G_z}. \quad (2.7)$$

To obtain a rectangular slice profile, the bandwidth $\Delta \omega_{RF}$ of the RF-pulse has to match the corresponding resonance frequencies. For small flip angles the slice profile in the frequency domain corresponds to the Fourier Transform (FT) of the RF-pulse envelope, so that a sinc-shaped envelope will result in a rectangular frequency bandwidth and

2. MRI of diffusion

therefore in a uniform slice profile.

Frequency encoding

Frequency encoding is performed during signal readout by applying a time-invariant linear field gradient in x-direction. Thus, the precession frequency of the excited spins depends on the location along the x-direction

$$\omega(x) = \omega_0 + \gamma G_x x. \quad (2.8)$$

Hence, the recorded signal during the readout time contains different frequencies, which allow the positioning of the signal origin along the x-axis. The bandwidth of the received signal depends on the strength of the applied readout gradient. The difference between the lowest and highest frequency is defined as:

$$\Delta\omega = \omega(x_h) - \omega(x_l) = \gamma G_x \cdot (x_h - x_l). \quad (2.9)$$

The received encoded signal $S(t_x)$ during the readout time t_x contains different frequencies, which allow the positioning of the signal origin along the x-axis. The received signal is expressed as

$$S(t) = S(t) \int_x e^{-i\gamma G_x x t_x} dx, \quad (2.10)$$

where $S(t)$ is given by Eq. (2.5).

Phase encoding

To achieve a signal encoding in the remaining y-direction a second gradient, the phase encoding gradient (G_y), has to be switched on for a certain period of time (t_y). This method of the 2D Fourier NMR imaging was first introduced by [33] and the current approach to phase encoding was given by [44]. During the time t_y , where G_y is switched on, the spins along the y-axis are precessing with different frequencies and accumulate different phases, which corresponds to their location in y-direction. After t_y the phase encoding gradient is turned off and the spin precession frequency is the same as before, but the phase dependence $\phi(y)$ remains and is given by

$$\phi(y) = \phi_0 + \gamma G_y y t_y. \quad (2.11)$$

The signal can not be spatially resolved by simply one phase encoding step, because the superimposed signal will contain no different frequencies in y-direction. To overcome this, the phase encoding has to be repeated many times by changing G_y in small steps

ΔG_y , which also changes the phase and amplitude of the superimposed signal. The signal $S(t_x, G_y)$ encoded now in both directions can then be written as

$$S(t_x, G_y) = S(t) \int_x \int_y e^{-i\gamma(G_x x t_x + G_y y t_y)} dx dy. \quad (2.12)$$

It is also possible to apply an additional phase encoding in the z -direction as it is used for 3D-imaging [45]. There, a thick slab is excited by the slice selection process, which can then be divided into very thin partitions due to the phase encoding. This allows a much higher spatial resolution in z -direction as compared to typical 2D-imaging.

2.2. Diffusion and nuclear magnetic resonance

2.2.1. Observing diffusion by using magnetic field gradients

If a spatial dependent field gradient is applied in addition to the static magnetic field B_0 , the resonance frequency becomes spatial depended.

$$\omega(r) = \gamma B_0 + \gamma(\vec{g} \cdot \vec{r}) \quad (2.13)$$

where \vec{g} is defined by

$$\vec{g} = \frac{\partial B_z}{\partial x} \hat{\mathbf{i}} + \frac{\partial B_z}{\partial y} \hat{\mathbf{j}} + \frac{\partial B_z}{\partial z} \hat{\mathbf{k}} \quad (2.14)$$

$\hat{\mathbf{i}}$, $\hat{\mathbf{j}}$ and $\hat{\mathbf{k}}$ are unit vectors of the laboratory frame of reference. The important fact is that if a linear gradient of known magnitude is imposed throughout the sample, the Larmor frequency becomes a spatial label with respect to the direction of the gradient. In MR imaging systems, which can produce equally strong magnetic field gradients in each of the x , y and z directions, it is possible to measure diffusion along any of the x , y or z -directions or combinations thereof. We can see from Eq. (2.13) that the cumulative phase shift is given by

$$\phi(t) = \gamma B_0 t + \gamma \int_0^t \vec{g} \cdot \vec{r} dt' \quad (2.15)$$

Where the first term on the right-hand side corresponds to the phase shift due to the static field, and the second term presents the phase shift due to the effects of the gradient. Thus, from Eq. (2.15) we can see, that the degree of dephasing due to gradient pulse is proportional to the type of the nucleus (i.e., γ), the strength of the gradient (i.e., g), the duration of the gradient (i.e., t), and the displacement of the spin along the direction of the gradient. The most common approach to measure diffusion is a simple

2. MRI of diffusion

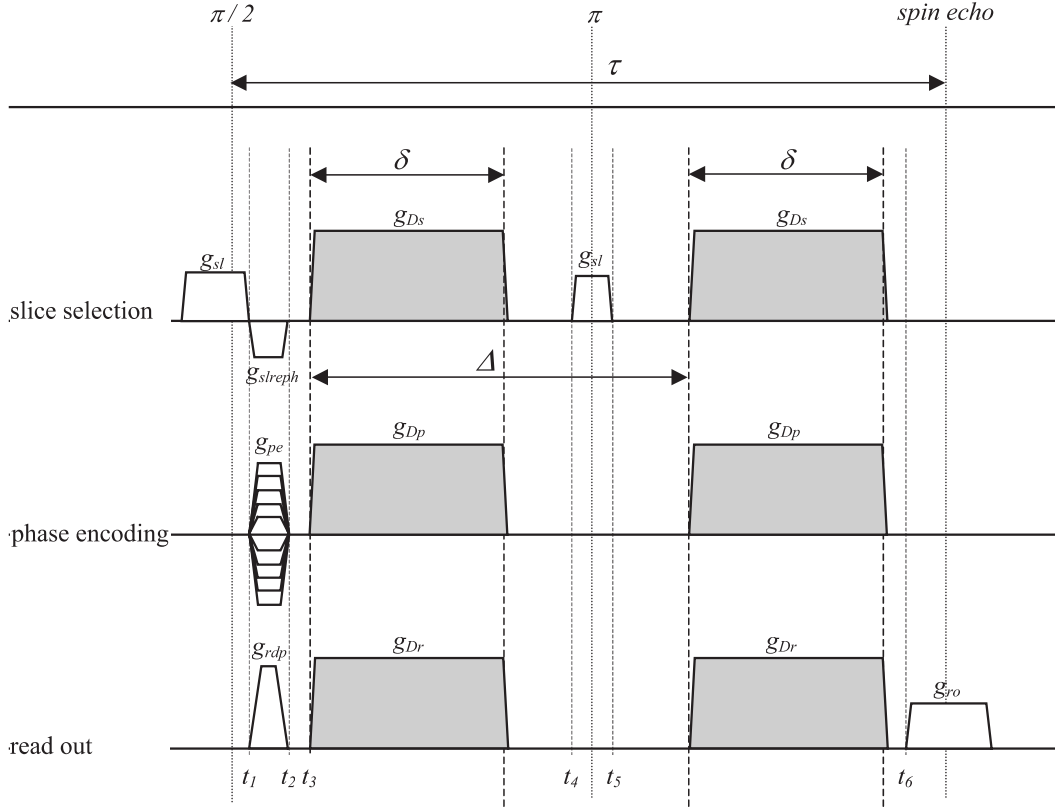


Fig. 2.6.: Schematics of the PGSE sequence with a echo time of 100 ms and a maximum diffusion gradient strength of 18 mTm. The diagram contains imaging gradients (white) as well as diffusion gradients (gray). The large diffusion gradients are defined by their strength g_D , duration δ and temporal separation Δ .

modification of the Hahn spin-echo pulse sequence [46], in which rectangular gradient pulses of the duration δ are inserted before and after the 180° -pulse (the “Stejskal and Tanner sequence”) [38]. The sequence is schematically show in Fig. 2.6. Imagine that we have an ensemble of diffusing spins at thermal equilibrium (that means that the net magnetization is oriented along the z -axis). The $\pi/2$ pulse in a PGSE sequence rotates the magnetization that is parallel to the static B_0 field into the x - y -plane. During the application of the first gradient pulse of duration δ and strength g the spins undergo an additional phase shift (in addition to the phase dispersion caused by the static inhomogeneities of the main field).

$$\phi_i(t) = \gamma B_0 t + \gamma \vec{g} \cdot \int_0^{t_i+\delta} \vec{r}_i(t') dt' \quad (2.16)$$

The term g was taken out of the integral in Eq. (2.16) since we are considering a constant amplitude gradient. The 180° pulse applied after half of the echo time ($\frac{\tau}{2}$) reverses the sign of the phases; this means that the sign of the phase angle, or equiv-

alently the sign of the applied gradients, is inverted. Consequently, application of the second gradient pulse at time $t_1 + \Delta$ (cf. Fig. 2.6) cancels the additional phase shift induced by the first gradient pulse. However, this process is only completely reversible in the absence of translational diffusion (the effects of T_2 are ignored). If the spins moved along the direction of the gradient during the time interval Δ , the additional phase shift will not be completely refocused, resulting in signal attenuation. At the end of the echo sequence, the total phase shift of the spin i relative to being located at $\vec{r} = (0, 0, 0)'$ is given by

$$\begin{aligned}\phi_i(\tau) &= \left(\gamma B_0 t + \gamma \vec{g} \cdot \int_0^{t_i+\delta} \vec{r}_i(t') dt' \right) - \left(\gamma B_0 t + \gamma \vec{g} \cdot \int_{t_i+\Delta}^{t_i+\Delta+\delta} \vec{r}_i(t') dt' \right) \\ &= \gamma \vec{g} \cdot \left(\int_0^{t_i+\delta} \vec{r}_i(t') dt' - \int_{t_i+\Delta}^{t_i+\Delta+\delta} \vec{r}_i(t') dt' \right)\end{aligned}\quad (2.17)$$

Since we are concerned with an ensemble of nuclei (with different start and end positions) in NMR, the echo signal at $t = \tau$ (i.e., $S(\tau)$) is given by

$$S(\tau) = S(\tau)_{g=0} \int_{-\infty}^{\infty} P(\phi, \tau) e^{i\phi} d\phi. \quad (2.18)$$

Where $P(\phi, \tau)$ is the (relative) phase-distribution function which is a normalized function given by

$$\int_{-\infty}^{\infty} P(\phi, \tau) d\phi = 1. \quad (2.19)$$

$S(\tau)_{g=0}$ is the signal in the absence of a field gradient. If we consider only the real component of $S(\tau)$ and recalling De Moivre's theorem,

$$e^{i\phi} = \cos \phi + i \sin \phi \quad (2.20)$$

we have

$$S(\tau) = S(\tau)_{g=0} \int_{-\infty}^{\infty} P(\phi, 2\tau) \cos \phi d\phi. \quad (2.21)$$

From Eq.(2.17), it can be seen that the phase shift due to static field cancels. In the absence of diffusion, the phase shifts due to the two gradient pulses (or, conversely, in the presence of diffusion but with $g = 0$) will also cancel; thus, $\phi_i = 0$ for i , and as $\cos \phi = 1$ in Eq. [2.21], a maximum signal will be recorded. However, if we have diffusion, then the displacement function $\vec{r}_i(t)$ is time dependent and the phase shifts accumulated by an individual nucleus due to the action of the gradient pulses in the first and second $\tau/2$ period. The degree of miscancellation increases with increasing displacement due to diffusion along the gradient axis. These random phase shifts resulting from the diffusion

2. MRI of diffusion

are averaged over the whole ensemble of nuclei that contribute to the NMR signal. Hence, the observed NMR signal is not phase shifted but attenuated, and the greater the diffusion is, the larger is the observed attenuation of the echo signal. Similarly, as the gradient strength is increased in the presence of diffusion the echo signal attenuates. Net flow, on the other hand, causes a net phase shift of the echo signal instead of diffusion-induced “blurring” of the phases which results in a diminution (reduction) of the echo signal. In the discussion above, we did not consider the relaxation process that occurs during the echo sequence. Thus, in the absence of gradients, we would have the signal at $t = \tau$ equal to

$$S(\tau)_{g=0} = S(0) e^{-\frac{\tau}{T_2}} \quad (2.22)$$

Where $S(0)$ is the signal without attenuation due to relaxation - that is, the signal that would be observed immediately after the $\pi/2$ pulse. We assume here that the observed signal originates from a single species (i.e., the observed signal results from a population with a single relaxation time). In the presence of diffusion and gradient pulses, the attenuation due to relaxation and the attenuation due to diffusion and the applied gradient pulses are independent, and so we can write,

$$S(\tau)_{g=0} = S(0) e^{-\frac{\tau}{T_2}} f(\delta, g, \Delta, D). \quad (2.23)$$

Where $f(\delta, g, \Delta, D)$ is a function that represents the attenuation due to diffusion. Thus, if the PFG measurement is performed whilst keeping τ constant, it is possible to separate the contributions. Hence, by dividing Eq. [2.23] by Eq. [2.22] we normalize out the attenuation due to relaxation, leaving only the attenuation due to diffusion,

$$E = \frac{S(\tau)}{S(\tau)_{g=0}} = f(\delta, g, \Delta, D). \quad (2.24)$$

We now need to equate the attenuation E of the echo signal to the experimental variables; that is, we need to derive $f(\delta, g, \Delta, D)$.

2.2.2. Correlating signal attenuation with diffusion

The Bloch equation [47] including the effect of diffusion [37] is given by

$$\frac{d\mathbf{M}}{dt} = \gamma \mathbf{M} \times \mathbf{B} - \begin{pmatrix} 1/T_2 & 0 & 0 \\ 0 & 1/T_2 & 0 \\ 0 & 0 & 1/T_1 \end{pmatrix} \mathbf{M} + \begin{pmatrix} 0 \\ 0 \\ 1/T_1 \end{pmatrix} \mathbf{M}_0 + \nabla(\underline{\underline{\mathbf{D}}} \nabla \mathbf{M}) \quad (2.25)$$

and describe the equation of motion of the macroscopic magnetization vector $\mathbf{M} = (M_x, M_y, M_z)$, in the rotating frame in the presence of a magnetic field vector $\mathbf{B} =$

(B_x, B_y, B_z) . The variables T_1 and T_2 are the longitudinal and transverse relaxation times, respectively. The diffusion tensor is represented by $\underline{\underline{\mathbf{D}}}$ and \mathbf{M}_0 is the thermal equilibrium magnetization in the presence of the static field B_0 . In an imaging sequence, spins are subjected to time dependent gradients (e.g. slice selection, read-out) in addition to the static main field B_0 . The total magnetic field, therefore, is given by

$$\mathbf{B}(\mathbf{r}, t) = [0, 0, \mathbf{r} \cdot \mathbf{G}(t) + B_0]^T. \quad (2.26)$$

Here, \mathbf{r} represents the position vector and $\mathbf{G}(t)$ is defined by:

$$\mathbf{G}(t) = [G_x(t), G_y(t), G_z(t)]^T. \quad (2.27)$$

Substitution of Eq. [2.26] into Eq. [2.25] and defining the complex transverse magnetization, M_+ , which is precessing about the z axis, by

$$M_+ = M_x + iM_y \quad (2.28)$$

one obtains [37]

$$\frac{\partial M_+}{\partial t} = -i\gamma B_0 M_+ - i\gamma \mathbf{r} \mathbf{G}(t) M_+ - \frac{M_+}{T_2} + \nabla \underline{\underline{\mathbf{D}}} \nabla M_+. \quad (2.29)$$

In the absence of diffusion M_+ is exponentially decaying with the characteristic time T_2 , the transverse relaxation time. Introducing ψ , such that

$$M_+(\mathbf{r}, t) = \psi(\mathbf{r}, t) \exp(-i\gamma B_0 t - t/T_2), \quad (2.30)$$

and substituting Eq. [2.30] into Eq. [2.29] eliminates the attenuation due to transverse relaxation and results in

$$\frac{\partial \psi}{\partial t} = -i\gamma \mathbf{r} \mathbf{G}(t) \psi(\mathbf{r}, t) + \nabla \underline{\underline{\mathbf{D}}} \nabla \psi(\mathbf{r}, t). \quad (2.31)$$

$\psi(\mathbf{r}, t)$ is constant if $\mathbf{G}(t) = 0$ and no diffusion occurs. However, in the presence of field gradients \mathbf{G} , the spins are subjected to an additional precession. If they also diffuse $\psi(\mathbf{r}, t)$ is attenuated due to the displacement of the spins (translational motion) with different local phases. To solve Eq. [2.31] we follow Ref. [37] and define $\psi(\mathbf{r}, t)$ by writing

$$\psi(\mathbf{r}, t) = S(t) \exp\left(-i\gamma \mathbf{r} \int_0^t \mathbf{G}(t') dt'\right). \quad (2.32)$$

2. MRI of diffusion

This leads to the following equation:

$$\frac{\partial S}{\partial t} = S(t) \nabla \underline{\underline{\mathbf{D}}} \nabla \exp \left(-i \gamma \mathbf{r} \int_0^t \mathbf{G}(t') dt' \right). \quad (2.33)$$

Performing the integration (Eq. [2.33]) yields

$$S(t) = S_0 \exp \left[-\gamma^2 \int_0^t \left(\int_0^{t'} \mathbf{G}(t'') dt'' \underline{\underline{\mathbf{D}}} \int_0^{t'} \mathbf{G}^T(t'') dt'' \right) dt' \right]. \quad (2.34)$$

Using

$$\mathbf{F}(t') = \int_0^{t'} \mathbf{G}(t'') dt'' \quad (2.35)$$

we can simplify Eq. [2.35] to obtain $S(t)$ at time τ

$$S_\tau = S_0 \exp \left(-\gamma^2 \int_0^\tau (\mathbf{F}(t') \underline{\underline{\mathbf{D}}} \mathbf{F}^T(t')) dt' \right) \quad (2.36)$$

where S_0 represents the initial transverse magnetization. Referring to Eq. [2.24] the echo attenuation E can thus be written as

$$E = \frac{S_\tau}{S_0} = \exp \left(-\gamma^2 \int_0^\tau (\mathbf{F}(t') \underline{\underline{\mathbf{D}}} \mathbf{F}^T(t')) dt' \right). \quad (2.37)$$

To separate the diffusion tensor $\underline{\underline{\mathbf{D}}}$ from the gradient terms we rewrite Eq. [2.37] by using the double dot product and obtain

$$\ln E = -\gamma^2 \int_0^\tau (\mathbf{F}^T \mathbf{F}) dt : \underline{\underline{\mathbf{D}}}. \quad (2.38)$$

The double dot product is the multiplication of two tensors and results in a scalar. In deriving Eq. [2.38] we have assumed that the diffusion tensor is not time-dependent and can be moved outside the integral. The remaining part is considered as the \mathbf{b} -matrix and is defined as a dyadic product. A dyadic is formed by the outer or direct product of two vectors, a column vector and a row vector:

$$\mathbf{b} = -\gamma^2 \int_0^\tau (\mathbf{F}^T \mathbf{F}) dt. \quad (2.39)$$

When the coefficients of the dyadic product are written as a $N \times N$ array it is called a matrix. By rewriting Eq. [2.38] as a double dot product in sum notation using Eq.

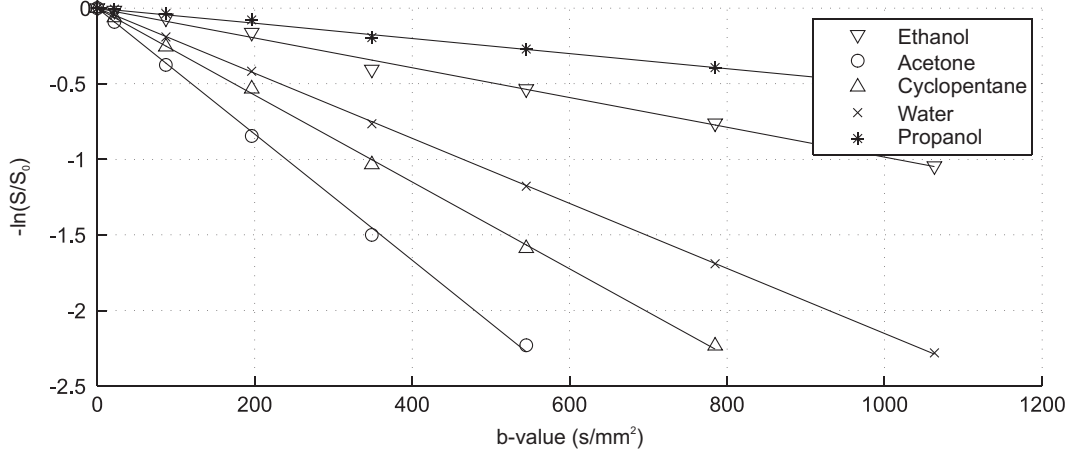


Fig. 2.7.: Signal attenuation of several liquids measured at different b -values.

[2.39] we obtain

$$\ln E = \mathbf{b} : \underline{\underline{\mathbf{D}}} = - \sum_{i=1}^3 \sum_{j=1}^3 b_{ij} D_{ji}. \quad (2.40)$$

From this expression it can be clearly seen that each b -matrix element b_{ij} weights the contribution of the corresponding diffusion tensor component D_{ij} linearly with respect to the measured logarithmic NMR signal ratio. The scalar b -value, applicable for isotropic diffusion, is obtained by performing the integration over the scalar or inner product $\mathbf{F}\mathbf{F}^T$. It can also be obtained by calculating the trace of \mathbf{b} .

$$b = \gamma^2 \int_0^\tau (\mathbf{F}^T \mathbf{F}) \, dt = \text{Tr}(\mathbf{b}). \quad (2.41)$$

To demonstrate the correlation of the echo attenuation with the diffusion effect we performed an experiment to determine the diffusion coefficient of five different liquids (Propanol, Ethanol, Water, Cyclopentane, Acetone). Therefore, a conventional spin-echo sequence was modified by inserting two gradient pulses before and after the π -pulse (cf. Fig. 2.6) in read-out direction ranging from 0 up to 21 mT/m. The model substances were filled in small bottles and the MRI signal was acquired using a small loop coil (\varnothing 8 cm). The used protocol parameters were: FOV = $200 \times 200 \text{ mm}^2$, slice thickness 2 mm, matrix size 256×256 , TR = 1000 ms, TE = 100 ms, diffusion-time Δ = 64.56 ms, diffusion gradient pulse duration δ = 24.5 ms at a 1.5 T whole-body MR scanner (Magnetom Vision, Siemens, Erlangen). In Fig. 2.7 the logarithmized signal ratio ($\ln E$) is plotted as a function of the b -value. The last two echoes were omitted for acetone and the last echo for Cyclopentane, due to low signal-to-noise ratios. From the plot we extracted the self diffusion coefficient listed in 2.1 by using linear regression.

Tab. 2.1.: Comparison of measured self-diffusion coefficients with values taken from literature ($^1T = 18.5^\circ C$, $^2T = 25^\circ C$)

substance	$D_{measured}$	$D_{literature}$	Reference
Acetone	4.17	4.06^1	[48]
Cyclopentane	2.71	3.23^2	[49]
Ethanol	0.99	1.01^2	[50]
Propanol	0.51	0.50^2	[50]
Water	2.15	2.03^1	[48]

The experimentally derived diffusion coefficients were found to be in a good agreement to the values from the literature.

2.3. The b-matrix

2.3.1. b-Matrix calculation

The link between the measured NMR signal and the self-diffusion tensor is established by the so-called b-matrix we derived in Eq. (2.40), which depends on the gradients direction, strength and timing. However, in the calculation of b-matrix elements the influence of imaging gradients on each element of the b-matrix is often neglected. This may cause errors, which in turn leads to an incorrect extraction of diffusion coefficients. We will demonstrate the error of neglecting these imaging gradients on the b-matrix calculation by investigating a pulsed gradient spin-echo (PGSE) imaging sequence. Starting from Eq. (2.41) we can calculate the b-value for the Stejskal-Tanner PFG sequence [51] and take into account only the rectangular diffusion gradient pulse pair with the strength g_D . However, we have to use the effective gradient strength in the function $F(t)$ (cf. Eq. (2.35)) which means that the gradient polarity has to be reversed after each π pulse. In case of a spin-echo sequence the gradient pulse pair is then defined as

$$G(t') = \begin{cases} g & t' < \tau/2 \\ -g & t' > \tau/2 \end{cases} \quad (2.42)$$

and the final expression for the b-value becomes very simple

$$b = \gamma^2 g_D^2 \delta^2 (\Delta - \delta/3). \quad (2.43)$$

In many instances, in particular with clinical imaging applications, only this simplified expression (Eq. (2.43)) is used for the b-value while the contributions of the imaging gradients are neglected. However, with large imaging gradients in combination with

low to moderate diffusion weighting gradient pulses, so-called "cross-terms" have to be considered. Solving Eq. (2.40) analytically it can be shown that the influence of the cross-terms on the final b -value depends strongly on the selected imaging acquisition parameters as well as on the spatial orientation of the diffusion pulses with respect to the imaging gradients [52]. Considering all imaging and diffusion gradients in Eq. (2.41) each element of the b -matrix can be decomposed into three parts

$$b_{ij} = b_{d_{ij}} + b_{ct_{ij}} + b_{img_{ij}} \quad (2.44)$$

Usually, the largest contribution to b_{ij} is the diffusion term $b_{d_{ij}}$ which is proportional to the product of the strength of two diffusion gradients and a factor containing information about the timing elements (δ , Δ) of these gradients. The second term $b_{ct_{ij}}$, also called the "cross term", depends on the product of a diffusion gradient pulse and one imaging gradient. Hence, this term occurs only in the presence of diffusion gradients. The third term $b_{img_{ij}}$ is generated by the imaging gradients alone and usually has the smallest contribution to b_{ij} . This term is present even in the absence of the diffusion gradients and causes very small diffusion weighting in common imaging sequences. However, this term still occurs in the so-called b_0 -image ($S(\tau)_{g=0}$), which is acquired without diffusion weighting gradients and utilized to calculate the correct b -matrix. If we consider this b_0 -image as a low diffusion weighted image ($S(\tau)_{g=low}$), Eq.(2.40) can be written as

$$\ln(E) = \ln\left(\frac{S(\tau)_{g=high}}{S(\tau)_{g=low}}\right) = - \sum_{i=1}^3 \sum_{j=1}^3 \left(b_{ij}^{high} - b_{ij}^{low}\right) D_{ij} \quad (2.45)$$

Using the same imaging parameters to acquire $S(\tau)_{g=high}$ and $S(\tau)_{g=low}$ the term b_{img} can be ignored in Eq. (2.44). Thus, we replace $S(\tau)_{g=0}$ by $S'(\tau)_{g=0}$ which represents a low diffusion weighted image weighted with b_{img} . This procedure eliminates the contribution of b_{img} to the b -matrix elements. Consequently, we only have to consider the cross term b_{ct} in addition to b_d (cf. Eq. (2.44)). The b_{ct} values depend directly on the following imaging sequence parameters: field of view (FOV), slice thickness (SL) and readout data size ($MATRIX$). This will be demonstrated in the experimental part with two different imaging protocol settings. To compare simulated with experimental data we used an isotropic phantom. In this case only the diagonal elements of the b -matrix have to be considered. Assuming an isotropic diffusion tensor

$$\underline{\underline{\mathbf{D}}} = \begin{bmatrix} D_{iso} & 0 & 0 \\ 0 & D_{iso} & 0 \\ 0 & 0 & D_{iso} \end{bmatrix}, \quad (2.46)$$

2. MRI of diffusion

the signal attenuation is (cf. Eq. (2.40))

$$\begin{aligned} \ln E' &= \ln \left(\frac{S(\tau)_g}{S(\tau)_{g=0}} \right) = -(b_{11} + b_{22} + b_{33}) D_{iso} \\ &= -[(b_{d_{11}} + b_{d_{22}} + b_{d_{33}}) + (b_{ct_{11}} + b_{ct_{22}} + b_{ct_{33}})] D_{iso}, \end{aligned} \quad (2.47)$$

To compare the measured data (the left hand side of Eq. (2.47)) directly with the "error-term", given by the sum of the "cross-term" elements ($b_{ct_{11}} + b_{ct_{22}} + b_{ct_{33}}$), but independently of the numerical value of the diffusion coefficient, D_{iso} , we make the additional assumption that the influence of the phase encoding gradient on the b -matrix elements can be neglected. This is a reasonable approximation because the main signal intensity is related to the center of k -space where the amplitude of this gradient is zero or close to zero. Thus, by applying a diffusion gradient pulse in the phase encoding direction (g_{D_p}) only, one obtains a diffusion weighted reference signal without any influence from "cross-terms"

$$\ln E'_{ref} = \ln \left(\frac{S(\tau)_{g=ref}}{S'(\tau)_{g=0}} \right) = -b_{d_{22}} D_{iso} = -b_{ref} D_{iso}, \quad (2.48)$$

If we further require that $b_{ref} = b_{d_{11}} + b_{d_{22}} + b_{d_{33}}$ in all experiments where the diffusion gradient pulse pairs are applied – not only in the phase encoding direction but in arbitrary directions – we can combine Eqns. (2.47) and (2.48) to obtain the following relation:

$$\frac{\ln E'}{\ln E'_{ref}} = 1 + \frac{b_{ct_{11}} + b_{ct_{22}} + b_{ct_{33}}}{b_{d_{11}} + b_{d_{22}} + b_{d_{33}}} = 1 + \frac{b_{ct_{11}} + b_{ct_{22}} + b_{ct_{33}}}{b_{ref}}. \quad (2.49)$$

Equation (2.49) can then be used to verify the analytically calculated b -values (right-hand side of Eq. (2.49)) by measuring $S(\tau)_g$, $S(\tau)_{g=ref}$ and $S'(\tau)_{g=0}$ inserting the values on the left hand side.

Another approach to investigate the influence of the imaging gradients on the b -matrix has been proposed by Neeman et al. [53]. By determining the geometric average of two diffusion weighted images ($S(\tau)_{g=pos}$, $S(\tau)_{g=neg}$) with opposite diffusion weighting directions (e.g., positive and negative diffusion gradient pulse pairs in the read-out direction) it is possible to obtain an image that is free of cross-term contamination (b_{ct}). Ideally, the directionally opposed diffusion weighting generates cross-terms with equal contributions but opposite signs. Hence, the b_{ct} term is eliminated by taking the product of the two signals:

$$\sqrt{S(\tau)_{g=pos} S(\tau)_{g=neg}} = S(\tau)_{g=0} e^{-D(b_{img} + b_d)}. \quad (2.50)$$

Furthermore, the square root of the ratio between the two images contains only the "cross-term" contribution

$$\sqrt{\frac{S(\tau)_{g=pos}}{S(\tau)_{g=neg}}} = e^{Db_{ct}}. \quad (2.51)$$

This approach, however, requires two scans in each direction and doubles the acquisition time. The term b_{img} in Eq. (2.50) can be eliminated in the same way that led to Eq. (2.47). If we set

$$S'(\tau)_{g=0} = S(\tau)_{g=0} \cdot e^{-Db_{img}}. \quad (2.52)$$

for the low diffusion-weighted image, $S'(\tau)_{g=0}$, and calculate the signal ratio between the geometric average (cf. Eq. (2.50)) and $S'(\tau)_{g=0}$ (cf. Eq. (2.52)) we finally obtain an expression which contains only a contribution of b_d

$$\sqrt{\frac{S(\tau)_{g=pos} S(\tau)_{g=neg}}{S'(\tau)_{g=0}}} = \frac{S(\tau)_{g=0} \cdot e^{-D(b_{img}+b_d)}}{S(\tau)_{g=0} \cdot e^{-Db_{img}}} = e^{-D \cdot b_d}. \quad (2.53)$$

The diffusion term b_d is then calculated using the simple expression in Eq. (2.43). Applying different diffusion weighting directions that sample full circles in the three principal planes $(x-y)$, $(x-z)$ and $(y-z)$, as described in the experimental part below, we are able to generate image pairs $(S(\tau)_{g=pos}, S(\tau)_{g=neg})$ with opposite diffusion weighting directions. With these image pairs it is then possible to extract a cross-term free diffusion coefficient using by Eq. 2.53.

The *analytical* computation of Eq. (2.41) was performed using an in-house developed script for the software package MAPLE 8 (Waterloo Maple Inc., Ontario, Canada). This script handles different gradient pulse shapes and gradient strengths by variables. Only the timing elements are fixed by the particular pulse sequence. The actual gradient strength of the imaging gradients was calculated and substituted by the corresponding sequence parameters (field of view - FOV , readout resolution - $MATRIX$, and slice thickness - SL). The output of the script is a parameterized b -matrix, which depends on these three parameters and the diffusion sensitizing gradients in the three spatial directions $(x, y$ and $z)$. For the numerical calculation we solved Eq. (2.41) for a PGSE sequence with the following parameters: $TE = 100$ ms, length of the diffusion sensitizing gradients $\delta = 20$ ms, time separation of these gradients $\Delta = 69$ ms. Furthermore, the ramp-up and ramp-down times were equal and were chosen $500 \mu s$ and $600 \mu s$ for all imaging and diffusion sensitizing gradients, respectively. The time points t_1, \dots, t_6 (Fig. 2.6), which define the pulse positions, were 1.78 ms, 4.22 ms, 5.22 ms, 48.22 ms, 51.78 ms, and 95.28 ms, respectively. The amplitudes of the imaging gradients g_{sl} (slice-selection gradient), g_{slreph} (slice-refocusing gradient), g_{rdp} (read-dephasing

2. MRI of diffusion

gradient), and g_{ro} (read-out gradient) were calculated according to the technical specifications of the manufacturer (Siemens Medical Systems, Erlangen, Germany) and are given in mT/m .

$$g_{sl} = 1 \times \frac{10}{SL(mm)}, \quad (2.54)$$

$$g_{slreph} = 1 \times \frac{10}{SL(mm)}, \quad (2.55)$$

$$g_{rdp} = 3.61 \times \frac{500}{FOV(mm)} \times \frac{MATRIX}{256} \quad (2.56)$$

and

$$g_{ro} = 1.566 \times \frac{500}{FOV(mm)} \times \frac{MATRIX}{256}. \quad (2.57)$$

From Eqs. (2.54 - 2.57) it is clearly seen, that the amplitudes of the imaging gradients depends on the used protocol parameters (slice thickness, field of view and matrix size). High spatial resolution is achieved by a small slice thickness SL , high readout sampling resolution ($MATRIX$) and a small field of view (FOV). Thus, high spatial resolution always requires large imaging gradient amplitudes. As already mentioned the contribution of the phase encoding gradient to the b -value can be neglected. The sequence design was chosen to achieve large *cross-terms* to ensure a significant mismatch between b -matrices calculated with and without taking into account all imaging gradients. For instance, removing the readout dephasing gradient g_{rdp} from its position in (insert figure number of PGSE imaging sequence) and moving it as close as possible to the readout gradient g_{ro} dramatically reduces the *cross-terms*. Using the analytical expressions of the b -matrix elements and the timing parameters of the PGSE sequence the diagonal elements b_{11} , b_{22} and b_{33} were calculated and decomposed into the b_d , b_{ct} and b_{img} contributions (2.2). From Eq. (2.49) and the parameterized b -values in Table

Tab. 2.2.: Calculated diagonal b -matrix elements decomposed in b_d , b_{ct} and b_i for the applied PGSE sequence - g_{Dr} , D_s , g_{Dp} are the amplitudes of the diffusion gradients in mT/m and $MATRIX$ in pixel, FOV in mm and SL in mm are the protocol parameters.

$[s/mm^2]$	b_d	b_{ct}	b_i
$b_{11} = b_{xx}$	$1.7860 \cdot g_{Dr}^2$	$+ 2.7028 \cdot \frac{MATRIX}{FOV} g_{Dr}$	$+ 1.2532 \cdot \frac{MATRIX^2}{FOV^2}$
$b_{22} = b_{yy}$	$1.7860 \cdot g_{Dr}^2$		
$b_{33} = b_{zz}$	$1.7860 \cdot g_{Dr}^2$	$- 0.0807 \cdot \frac{1}{SL} g_{Ds}$	$+ 0.2544 \cdot \frac{1}{SL^2}$

2.2 we obtain the following expression for isotropic diffusion:

$$\frac{\ln S(\tau)_g - \ln S'(\tau)_{g=0}}{\ln S(\tau)_{g=ref} - \ln S'(\tau)_{g=0}} = 1 + \frac{b_{ct}}{b_d} = 1 + \frac{2.7028 \cdot g_{D_r} \cdot \frac{MATRIX}{FOV} - 0.0807 \cdot g_{D_s}}{1.7860 \cdot g_{D_{pref}}^2}. \quad (2.58)$$

As can be seen from this equation the measured signal intensity ratio is directly related to easily adjustable sequence parameters and the relative influence of the *cross-terms* can be estimated.

To demonstrate experimentally the influence of the imaging gradients on the diffusion weighting we used the PGSE sequence shown in 2.6. All experiments were performed on a whole-body MR scanner (Magnetom Vision 1.5 T, Siemens, Erlangen, Germany) with a maximum diffusion gradient strength of $g_{max} = 18 \text{ mT/m}$. To investigate the influence of the direction of the diffusion weighting we sampled the spatial direction along circular paths in steps of 15 degrees. The circular paths were placed in the three principal planes ($x-y$, $x-z$, $y-z$), respectively. Fig. 2.8 demonstrates the sampling scheme graphically by the solid lines.

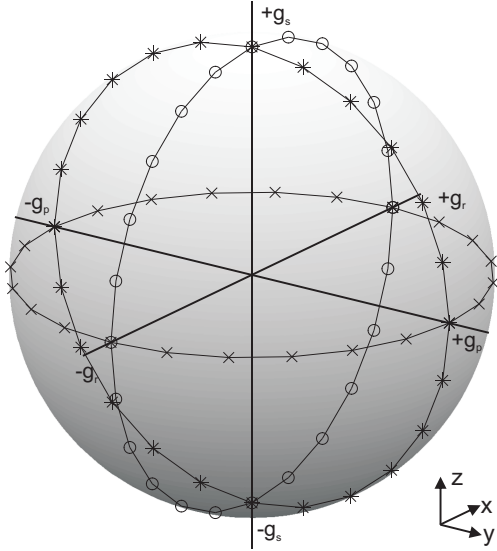


Fig. 2.8: Sampling scheme used in the experimental part to estimate the contribution of the imaging gradients to the *b*-matrix elements. Using diffusion gradients with different amplitudes simultaneously in two directions, diffusion weighting was realized along the solid lines. Position of sampling directions - $g_{D_p}g_{D_r}$, $-g_{D_p}g_{D_s}$ and $-g_{D_r}g_{D_s}$.

For each sampled direction we calculated the *b*-matrix using Eq. (2.39) with and without taking the imaging gradients into account. Neglecting the imaging gradients, the diffusion weighting is the same for all sampling directions ($b = b_{ref} = 578.7 \text{ smm}$). The circular pathways are listed as diffusion gradient tables in Table 2.3. g_{D_p} , g_{D_r} and g_{D_s} are the diffusion gradient amplitudes in phase encoding, readout and slice selection direction, respectively. To investigate the influence of the three imaging sequence parameters, *FOV*, *MATRIX*, and *SL*, we sampled the sphere twice with different parameter settings (set 1: $FOV = 128 \text{ mm}$, $MATRIX = 256$, $SL = 3 \text{ mm}$; set 2: FOV

Tab. 2.3.: Definition of diffusion gradient amplitudes for sampling along circular paths with $\alpha = 0^\circ \dots 360^\circ$

	g_{D_p}	g_{D_r}	g_{D_s}	abbreviation
phase enc. - read-out	$g_{max} \cos(\alpha)$	$g_{max} \sin(\alpha)$	0	$g_{D_p} g_{D_r}$
phase enc. - slice dir.	$g_{max} \cos(\alpha)$	0	$g_{max} \sin(\alpha)$	$g_{D_p} g_{D_s}$
read-out - slice dir.	0	$g_{max} \cos(\alpha)$	$g_{max} \sin(\alpha)$	$g_{D_r} g_{D_s}$

= 196 mm, MATRIX = 128, SL = 5 mm). Thus, the imaging gradients were applied with different amplitudes as given in Eq. (2.54-2.57).

A small glass bottle ($\varnothing = 7$ cm) filled with distilled water was used as a phantom and a small surface coil ($\varnothing = 8$ cm) was used for imaging. The temperature was held constant at 21°C during the experiments. All measurements were performed with two averages. The signal analysis was based on a rectangular region of interest (ROI) (for set 1: $\Delta x = 60$ pixel (30 mm), $\Delta y = 60$ pixel (30 mm) and for set 2: $\Delta x = 24$ pixel (36.8 mm), $\Delta y = 29$ pixel (44.4 mm)).

Error mapping

Fig. 2.9 show the simulated error $1 + b_{ct} b_d^{-1}$ maps (see Eq. (2.58)) for isotropic diffusion and both protocol sets. Here, $1 + b_{ct} b_d^{-1}$ was mapped on a spherical surface and remapped to 2D coordinates (longitude, latitude). Diffusion weighting in the positive slice selection direction ($+g_{D_s} = z$) corresponds to latitude angle = 0° (in this case the longitude angle is undefined), weighting in the positive readout direction ($+g_{D_r} = x$) to longitude angle = π and latitude angle = $\pi/2$ and weighting in the positive phase encoding direction to longitude angle = $\pi/2$ and latitude angle = $\pi/2$. A value of 1.0 means no contribution from the *cross-terms* to the scalar b -value. Fig. 2.9 illustrates the different sampling courses through the maps which correspond to the three different sampling measurements across the spherical surface as illustrated in Fig. 2.8 and described in Tab. 2.3. Figure 2.11 demonstrate the deviations along the sampling paths for the two different protocol settings. For set 1 we obtained a maximum value of $1 + b_{ct} b_d^{-1}$ of 1.168 and a minimum value of 0.832 and for set 2 a maximum of 1.055 and a minimum of 0.945. For both sets maxima were found when applying diffusion weighting in the readout direction and the minima were found when using diffusion weighting in readout direction with opposite polarity. Thus, the scalar b -value (sum of diagonal elements of the b -matrix: $b_{11} + b_{22} + b_{33}$) is miscalculated by up to ± 16.84 percent with the chosen parameters if the imaging gradients of the pulse

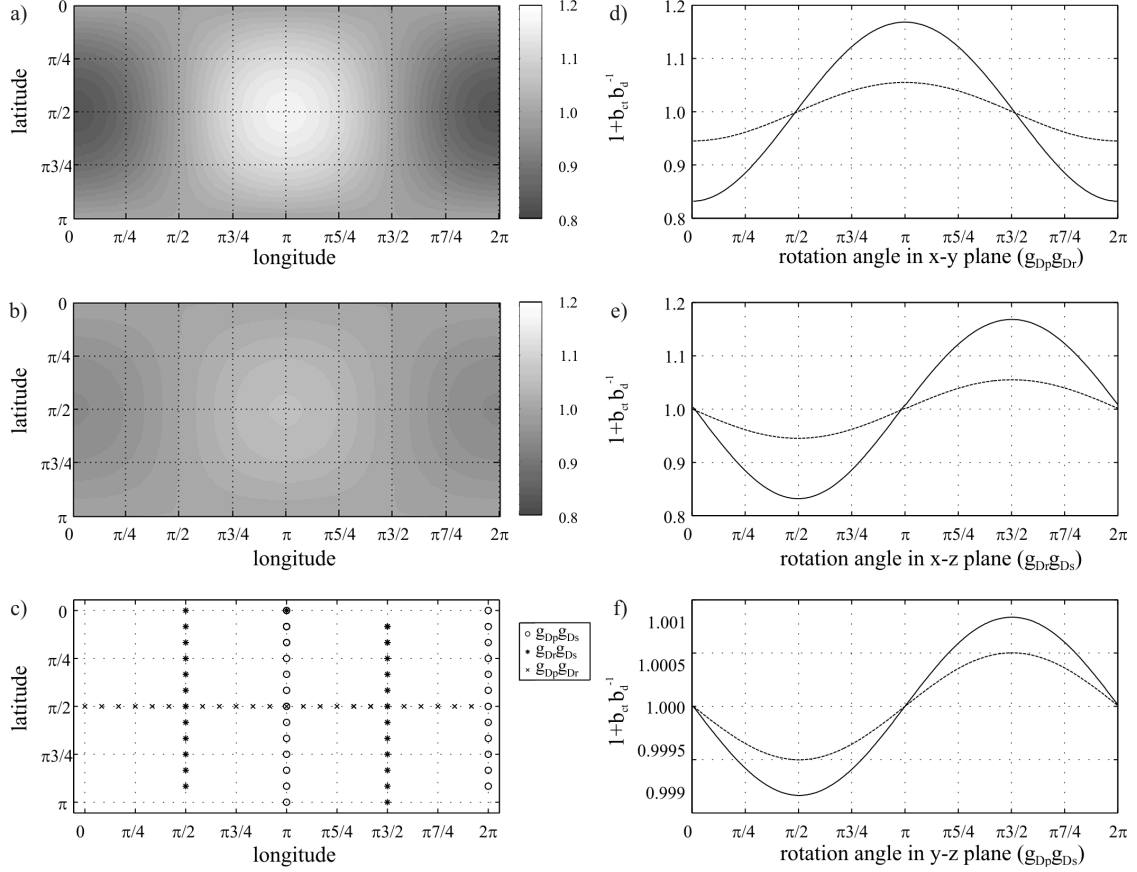


Fig. 2.9.: (a, b) Simulated error maps over a spherical surface for protocol set 1 (FOV = 128 mm, MATRIX = 256, SL = 3 mm) and set 2 (FOV = 196 mm, MATRIX = 128, SL = 5 mm), respectively. The spatial directions are represented by longitude and latitude. (0,0) corresponds to $+g_{D_s}$; (0, $\pi/2$) to $-g_{D_s}$; (0, $-\pi$) to $-g_{D_s}$. (c) Sampled directions used for the experiments. (d)-(f) Simulated data for the three measured circles ($g_{D_p}g_{D_r}$, $g_{D_r}g_{D_s}$, $g_{D_p}g_{D_s}$) and the two protocol settings (solid line = set 1, dashed line = set 2). Note the different scale in (f).

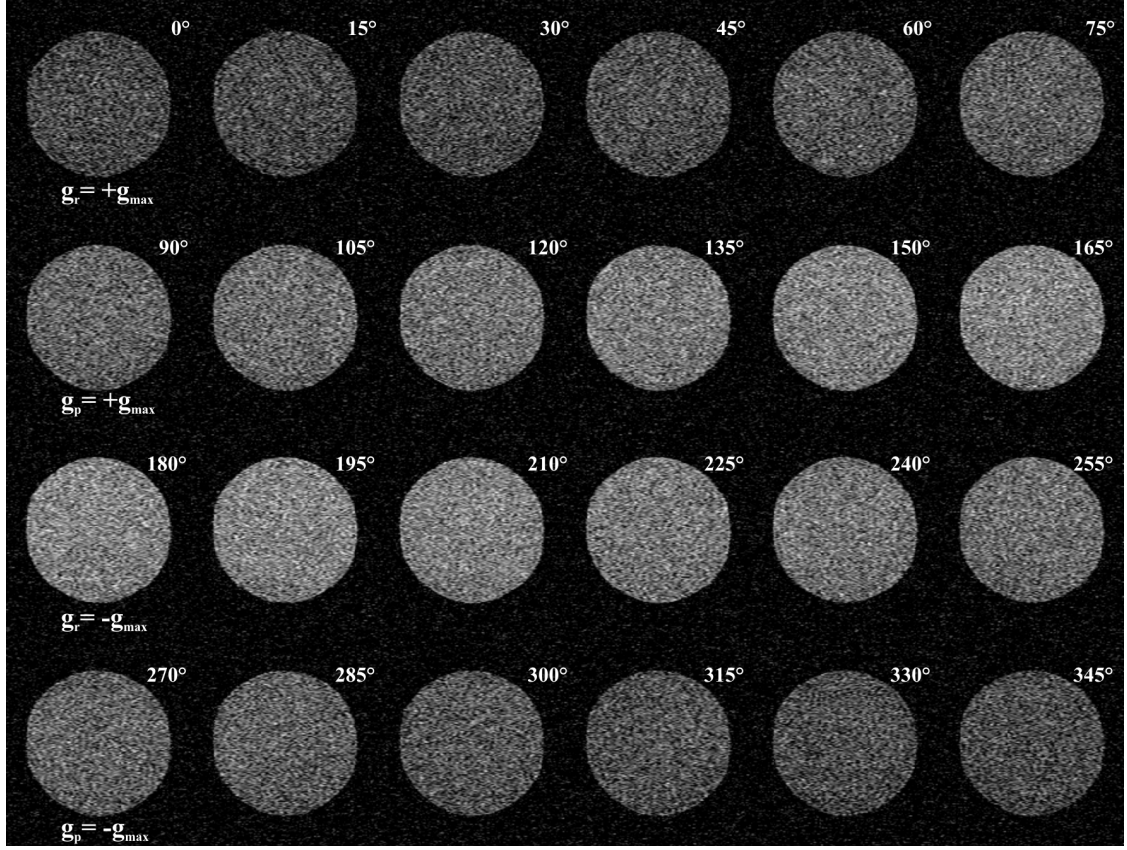


Fig. 2.10.: Diffusion weighted images for 24 sampling directions in steps of 15° in the $x - y$ -plane ($g_{D_p}g_{D_r}$) with equal diffusion weighting. The influence of the cross-term on the b -value is clearly seen by the changing image intensity. Parameter set 1 was used in for images in this figure.

sequence are neglected. Fig. 2.10 presents a series of diffusion weighted images for parameter set 1 which were acquired with different diffusion directions in the $x - y$ plane. All images have nominally the same b -value if the imaging gradients are neglected. Since the contribution of the *cross-terms* to the true b -value depends on the direction of the diffusion weighting the signal attenuation changes significantly between the images. Based on the assumption that Eq. (2.48) is not contaminated by cross-terms we used four data sets acquired with diffusion weightings only in the positive ($2\times$) or negative ($2\times$) phase encoding direction to compute an averaged $S(\tau)_{g=ref}$. These data sets were taken from the measurement series $g_{D_p}g_{D_r}$ and $g_{D_p}g_{D_s}$ (see Table 2.3). With this signal one can calculate the left-hand side of Eq. (2.58) by inserting the measured diffusion weighted images ($S(\tau)_g$) and the unweighted image ($S'(\tau)_{g=0}$). The experimental results - together with the simulated data of Fig. 2.9 - are plotted in Fig. 2.11 for parameter set 1 and set 2. In general, we observed a very good correlation between the simulation and the measurement data. However, the maximum b -value error of 0.083 percent obtained with the simulated diffusion weighting in the $y - z$

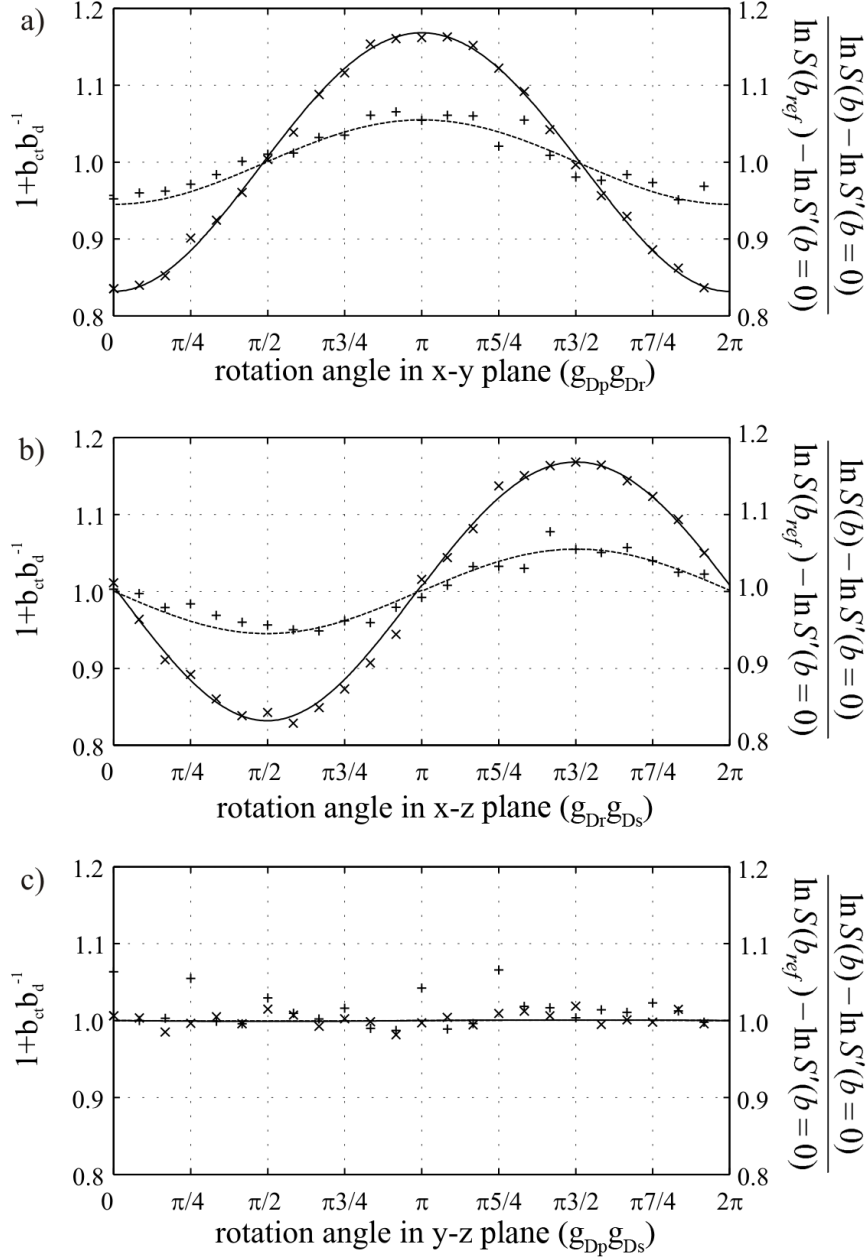


Fig. 2.11.: Comparison of simulated data (solid lines) with measured data (measuring points). The representation of the simulated data is identical with the diagrams in Fig. 2.9d-f. Note again the different scale in Fig. 2.9f (\times - data acquired with protocol set 1; $+$ - data acquired with protocol set 2).

2. MRI of diffusion

plane ($g_{D_p}g_{D_s}$) could not be experimentally verified (cf. Fig. 2.11). Fig. 2.12 shows the decomposition of the signal ratio between the weighted and unweighted images following the approach of Neeman et al. [54]. Pairs of diffusion weighted images with opposite diffusion weighting direction were used from the data presented in Fig. 2.12. This reduces the data points to the half circle ($0 - \pi$). As expected, the logarithm of the *cross-term* free signal ratio $\ln \left(\sqrt{S(\tau)_{g=pos} S(\tau)_{g=neg}} (S'(\tau)_{g=0}^{-1}) \right)$ (cf. Eq. (2.53)) was found at the same level of -1.199 ± 0.016 for all measurements. With a b-value of 578.7 s/mm^2 , which was calculated using Eq. (2.49) without taking the imaging gradients into account, a diffusion coefficient of $2.07 \pm 0.028 \times 10^{-3} \text{ mm}^2/\text{s}$ was obtained which is in excellent agreement with data from the literature [48, 49, 50] at room temperature (21°C). In addition, we plotted the logarithm of the signal ratio $\ln \left(\sqrt{S(b^+) (S(b^-))^{-1}} \right)$ as a function of the angle (cf. Eq. (2.51)). These curves closely follow the curves in Fig. 2.11. However, the actual values depend on the diffusion coefficient of the medium under investigation.

2.3.2. Experimental estimation of cross-term errors

Since, the imaging as well as the exact diffusion gradients are unknown without access to the sequence code, we can consider that the diffusion gradients are proportional to the square root of b_d , whereas b_d is the sum of $b_{d_{xx}}$, $b_{d_{yy}}$ and $b_{d_{zz}}$ known as scalar b-value [55]. Additionally, the cross-terms are proportional to the normalized gradient amplitudes taken from the gradient scheme in the form $[x, y, z]$. All the previous considerations lead to

$$\ln \left(\frac{S(b)}{S'(b_0)} \right) = -D_{iso} \cdot b_d [(x^2 + y^2 + z^2) + k_x x + k_y y + k_z z] \quad (2.59)$$

We regard k_x , k_y and k_z as unknowns. If these parameters are once determined, the full b -matrix can be reconstructed by applying

$$b_d \begin{bmatrix} x^2 + (k_x x) & x \cdot y + \left(\frac{k_x}{2} y + \frac{k_y}{2} x \right) & x \cdot z + \left(\frac{k_x}{2} z + \frac{k_z}{2} x \right) \\ x \cdot y + \left(\frac{k_x}{2} y + \frac{k_y}{2} x \right) & y^2 + (k_y y) & y \cdot z + \left(\frac{k_y}{2} z + \frac{k_z}{2} y \right) \\ x \cdot z + \left(\frac{k_x}{2} z + \frac{k_z}{2} x \right) & y \cdot z + \left(\frac{k_y}{2} z + \frac{k_z}{2} y \right) & z^2 + (k_z z) \end{bmatrix} \quad (2.60)$$

Attention should be paid on the fact, that in the off-diagonal elements the error terms contribute on half for each involved gradient direction and were multiplied with the contrarian normalized gradient.

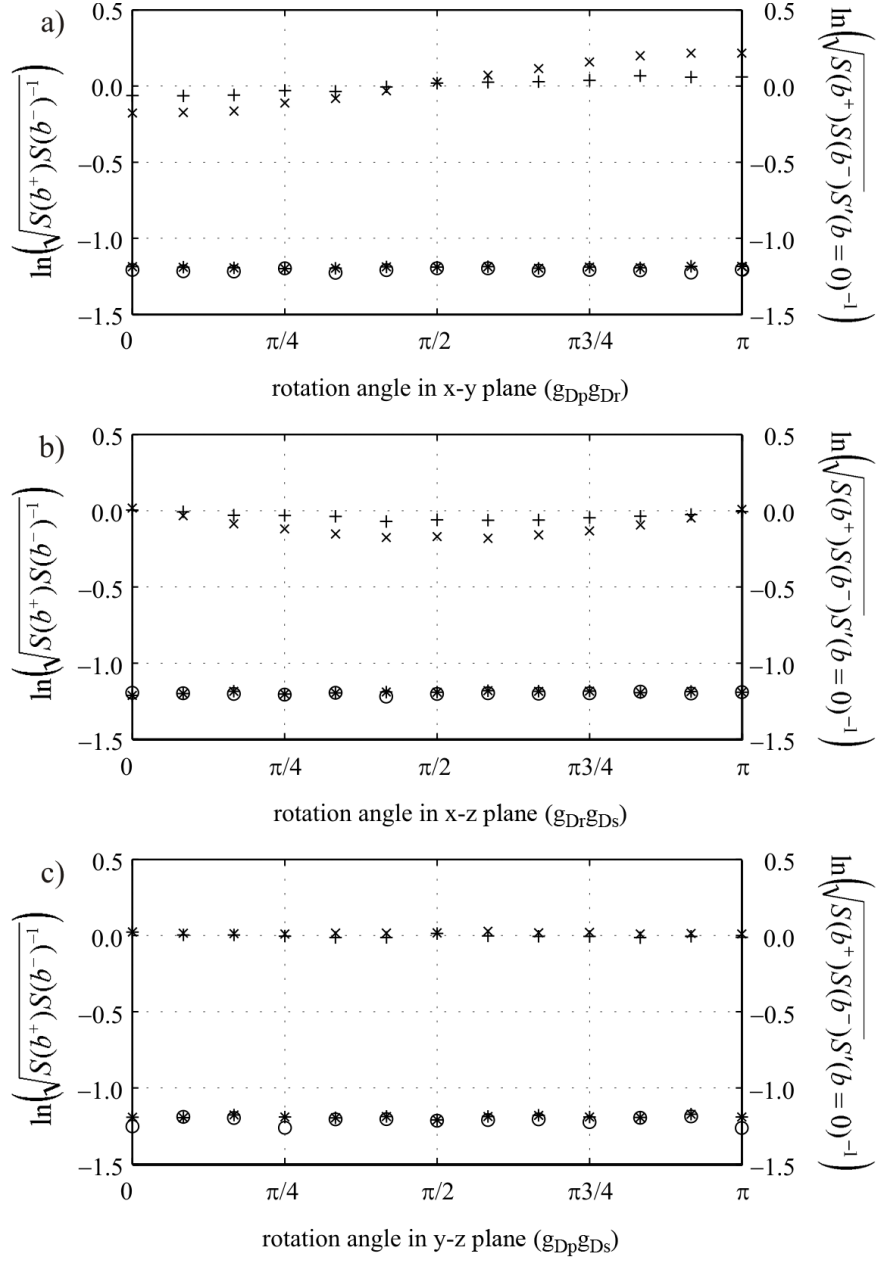


Fig. 2.12.: Decomposition of the signal according to Neeman et al. [54] into a cross-term free signal ratio (\circ for set 1, $*$ for set 2) (cf. Eq. (2.53)) and a signal ratio containing only the cross-term effect (\times for set 1, $+$ for set 2) (cf. Eq. (2.51)).

Data Fitting

The fitting of the data was performed using a *robust fit* function provided by the Statistics Toolbox of Matlab 7.0 (The Mathworks, Inc., USA). The *robust fit* function uses an iteratively reweighed least squares algorithm, with the weights at each iteration calculated by applying the bi-square function to the residuals from the previous iteration [56]. This algorithm gives lower weight to points that do not fit well. The results are less sensitive to outliers in the data as compared with ordinary least squares regression.

For a single data set the fit of Eq. (2.59) gives four parameters $p_{1...4}$ which are represented as follows

$$p_1 = -D_{iso}b_d, \quad (2.61)$$

$$p_2 = -D_{iso}b_dk_x, \quad (2.62)$$

$$p_3 = -D_{iso}b_dk_y \quad (2.63)$$

and

$$p_4 = -D_{iso}b_dk_z \quad (2.64)$$

Hence, the parameters k_x , k_y and k_z result from the division of $p_{2...4}$ by the constant term p_1 . For this reason the k -parameters seem to be independent from the diffusion coefficient D_{iso} as well as from the diffusion weighting represented by b_d . This holds true for the diffusion coefficient, however not for b_d . The k -parameters comprise the strength of the diffusion gradient g_D , which correlates with b_d as shown in Eq. (2.43), and thus they are only valid for a given b_d . This fact should be kept in mind while reading the further explanations.

By using multiple data sets with different protocol settings for the fit, these settings (matrix, field of view and slice thickness) have to be taken into account while fitting the data. If we assume that gradients in read-out and phase encoding direction are scaled by the ratio between matrix and field of view and gradients in slice direction are scaled by the reciprocal of the slice thickness, we can include this information into the fit procedure. Consequently, Eq. (2.59) can be rewritten

$$\ln \left(\frac{S(b)}{S'(b_0)} \right) = -D_{iso} \cdot b_d \left[(x^2 + y^2 + z^2) + k'_x \frac{MATRIX}{FOV} x + k'_y \frac{MATRIX}{FOV} y + k'_z \frac{1}{SL} z \right] \quad (2.65)$$

The k -parameters are different from the parameters which can be determined from a single data set and thus they will be treated as k' -parameters.

Measurements

The fitting procedure was investigated using three different data sets. The first data set (*data set 1*) was acquired using a pulsed-gradient spin-echo sequence (PGSE) as shown in Fig. 2.6. These sequence was intentionally designed to produce large cross-terms by placing the read-out dephasing gradient right after the excitation RF pulse. Knowing the full sequence design it was possible to estimate all terms of the b -matrix analytically. This makes it possible to compare the fitted parameter directly with the analytically derived parameters. The spin-echo sequence was implemented on a 1.5 T Magnetom Vision (Siemens, Erlangen, Germany) and applied by using a standard head coil and a spherical isotropic phantom filled with distilled water. Measurements were performed with diffusion gradient pairs applied in the x-y, x-z and y-z plane in steps of 15 degree (overall 72 measurement points, where 6 points are measured twice).

The sequence design and analytical analysis has been described in detail in [55]. The maximum diffusion gradient strength was 18 mT/m , applied over a duration of 20 ms with a time constant Δ (temporal distance between begins of the two gradients) of 69 ms. The settings for the diffusion gradients result in a diffusion weighting factor b of 578.7 s/mm^2 without taking into account the imaging gradients. The echo time of the sequence was 100 ms. To take into account different protocol settings we acquired images with a resolution of 256×256 pixel at a FOV of $128 \times 128 \text{ mm}^2$ and a slice thickness of 3 mm (entitled as high resolution in the following) as well as with a resolution of 128×128 pixel at a FOV of $196 \times 196 \text{ mm}^2$ and a slice thickness of 5 mm (entitled as low resolution in the following).

The second data set (*data set 2*) was also acquired on a 1.5 T Magnetom Vision (Siemens, Erlangen, Germany) employing a twice refocusing echo planar imaging (TRSE-EPI) [57] sequence with six different diffusion directions and a diffusion weighting of $b_d = 900 \text{ s/mm}^2$. The standard head coil and a spherical isotropic phantom filled with distilled water were used. To asses the dependence of the fit parameters on the protocol settings we applied three different field of views (210, 223 and 256 mm) and three different values for the slice thickness (3, 5 and 7 mm) resulting in 9 series by combining the protocol settings. The read-out resolution (matrix) was always set to 128.

A third data set (*data set 3*) was acquired on a 1.5 T Magnetom Sonata (Siemens, Erlangen, Germany) using also a standard head coil and a spherical isotropic phantom. Diffusion images were measured by employing a twice refocusing echo planar imaging (TRSE-EPI) [57] sequence provided by the manufacturer, which is also used in clinical routine. We applied this sequence with a diffusion gradient scheme comprising 12 directions. The measurements were performed with three different field of views (196, 226 and 256 mm) and four different values for the slice thickness (2, 4, 7 and 10 mm)

resulting in 12 series. The read-out resolution was always set to 128. A diffusion weighting factor of 600 s/mm^2 was applied.

Analysis

Error mapping To demonstrate the directional dependence of the error, the data sets were first mapped by means of longitude and latitude. Thus, the diffusion coefficients for different measurement points were calculated using the acquired signal ratio and the b -value, which was calculated once without considering the imaging gradients (*data set 1*) and once taking them into account (*data set 2* and *3*). To map the data two-dimensionally, the direction vectors were transformed to angle pairs (longitude and latitude). The maps are shown as contour maps with a contour step size of $0.05 \mu\text{m}^2/\text{ms}$ (for the diagrams in the upper row) which is around 2.5% of the mean diffusion coefficient, assuming a diffusion coefficient of $2.00 \mu\text{m}^2/\text{ms}$. The contour steps for the lower row with the EPI data was set to $0.01 \mu\text{m}^2/\text{ms}$. Data gridding was performed using a cubic spline algorithm, which does not take into account the spherical nature of the map. The upper row of Fig. 2.13 compares the error maps from simulation and measurement

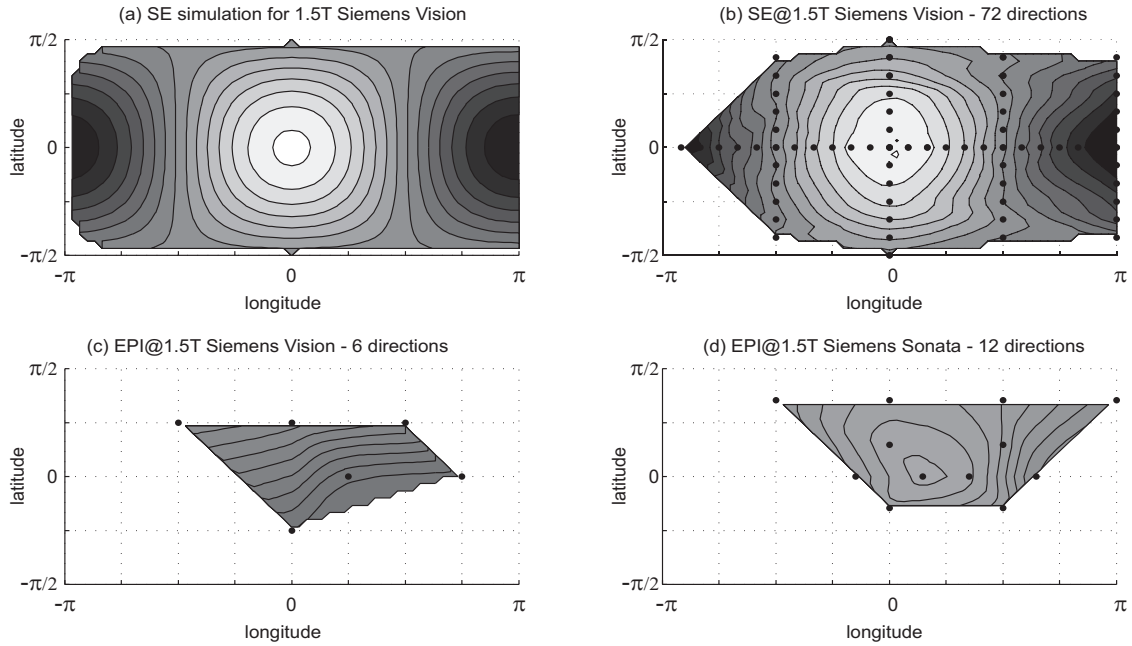


Fig. 2.13.: Contour maps of estimated diffusion coefficients using b -values which do not take into account cross-terms for simulation (a) and measurement (b) employing a Spin-Echo sequence (b -value = 578.7 s/mm^2 on a Siemens Vision MR-Scanner. The lower row shows the mapping for an EPI sequence with 6 directions (c) performed on a Siemens Vision Scanner and the on a Siemens Sonata Scanner using a 12 direction scheme.

for the spin-echo sequence. To calculate the simulated values a diffusion coefficient of $2.0848 \mu\text{m}^2/\text{ms}$ was used, which corresponds to the value determined during the fitting process for *data set 1*. The maximum was found at $(0, 0)$ (longitude, latitude) at a value of $2.454 \mu\text{m}^2/\text{ms}$ for the simulation and $2.428 \mu\text{m}^2/\text{ms}$ for the measurement. The position corresponds to diffusion weighting in x direction. A minimum value of $1.752 \mu\text{m}^2/\text{ms}$ for the simulation was found at $(-\pi, 0)$ corresponding to diffusion weighting in -x direction. For the SE measurement a minimum of $1.723 \mu\text{m}^2/\text{ms}$ was found at $(\pi, 0.261788)$ (longitude, latitude) corresponding to a diffusion weighting vector of $(0.9659, 0, 0.2588)$ (x, y, z).

Data set 1 The k -parameters derived for the spin-echo experiment with high resolution imaging parameters were 0.1689, 0.0018 and -0.0019 with a standard deviation of 0.0016 for all three values. For the low resolution series the parameters were 0.0517, -0.0009 and -0.0064, all with a standard deviation of 0.0034. In comparison to these values we calculated the k -parameters from the analytically derived b -matrices. For the high resolution series we obtained 0.1681, 0 and -0.0008 and for the low resolution series 0.0549, 0 and -0.0005 as k -parameters. The results for the k_x parameter are in very good agreement with the simulations. Also the k_y parameters are within the expected limits.

The k' -parameter, which are independent from the used acquisition settings were 0.0838, 0.0009 and -0.0126. The associated standard deviations are 0.0013, 0.0013 and 0.0069, respectively. The k'_z parameter could not be fitted as good as k'_x and k'_y . With the derived k and k' parameters corrected b -matrices were calculated to extract corrected diffusion tensors, which are compared to the diffusion tensors extracted with uncorrected b -matrices, as shown in Tab. 2.4.

Tab. 2.4.: Diffusion tensors derived for *data set 1* (high and low resolution data) by using different b -matrices. All values are given in $\mu\text{m}^2/\text{ms}$.

	D_{uc}, D_{sc}	D'_{uc}	D_{pc}
hr	$\begin{bmatrix} 2.085 & 0.002 & 0.005 \\ 0.002 & 2.085 & 0.002 \\ 0.005 & 0.002 & 2.079 \end{bmatrix}$	$\begin{bmatrix} 2.346 & 0.123 & 0.007 \\ 0.123 & 1.829 & 0.004 \\ 0.007 & 0.004 & 2.354 \end{bmatrix}$	$\begin{bmatrix} 2.082 & 0.001 & 0.005 \\ 0.001 & 2.088 & 0.001 \\ 0.005 & 0.001 & 2.082 \end{bmatrix}$
lr	$\begin{bmatrix} 2.088 & 0.002 & 0.004 \\ 0.002 & 2.093 & 0.007 \\ 0.004 & 0.007 & 2.084 \end{bmatrix}$	$\begin{bmatrix} 2.063 & 0.025 & 0.004 \\ 0.025 & 2.083 & 0.026 \\ 0.004 & 0.026 & 2.225 \end{bmatrix}$	$\begin{bmatrix} 2.087 & 0.002 & 0.003 \\ 0.002 & 2.094 & 0.005 \\ 0.003 & 0.005 & 2.081 \end{bmatrix}$

That the results for the D_{uc} and D_{sc} tensors are equal may be surprising, but is correct. This reduction of the errors using uncorrected b -matrices results from averaging of opposed diffusion weighting direction, since we applied diffusion weighting in 66

2. MRI of diffusion

different spatial directions whereas 33 directions have a collinear representation. This leads to a complete cancellation of the cross-terms as proposed by Neeman et al. [53] and one obtains the same results as by applying a corrected b -matrix. If we use signal values from only 6 diffusion weighting directions (instead of 66), we obtain the uncorrected diffusion tensors D'_{uc} also shown in Tab. 2.4. For this diffusion tensor estimation the influence of cross-terms is clearly visible. Also the reduction of cross-term influence by applying low resolution acquisition settings is clearly recognizable.

Data set 2 For the DTI-EPI series the diffusion tensors reconstructed using the uncorrected D_{uc} , the single corrected D_{sc} and the protocol corrected D_{pc} are not shown in detail. To provide the results of the correcting approach the standard deviation of the diagonal tensor elements (D_{xx}, D_{yy}, D_{zz}) were plotted on a grid with the field of view and the slice thickness as axis labels (cf. Fig. 2.14). In Fig. 2.14a it is clearly

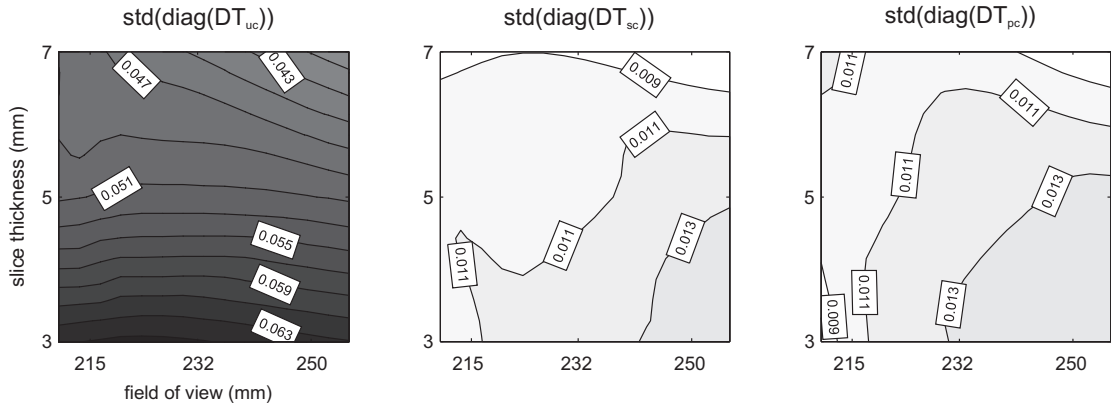


Fig. 2.14.: Standard deviation of diagonal tensor elements plotted by means of field of view and slice thickness for a) uncorrected Diffusion Tensors, b) single correct Diffusion Tensors and c) protocol corrected Diffusion Tensors for DTI-EPI series acquired on a Siemens Magnetom Vision.

shown, that the diagonal elements of the diffusion tensors have a larger deviation if a smaller slice thickness is used. With thicker slices a gradient in the standard deviation from large field of views to small field of views is also noticeable (Fig. 2.14(a)). The map in Fig. 2.14b shows that the standard deviation is reduced by a factor of 4 to 6 by applying corrected b -matrices for every protocol setting separately. If we apply a fit of the k' -parameters including the protocol (cf. Eq. 16) and use them to calculate corrected b -matrices, the standard deviation in the diagonal diffusion tensor elements Fig. 2.14c is similar to the results shown in Fig. 2.14b. That means that the assumption of scaling imaging gradients by changing the slice thickness and field of view holds true. To demonstrate that the k -parameters are a function of the field of view (FOV) and of

the slice thickness (SL), the parameters were plotted over these two protocol settings (Fig. 2.15). The k -parameters can be directly interpreted as relative deviation of the

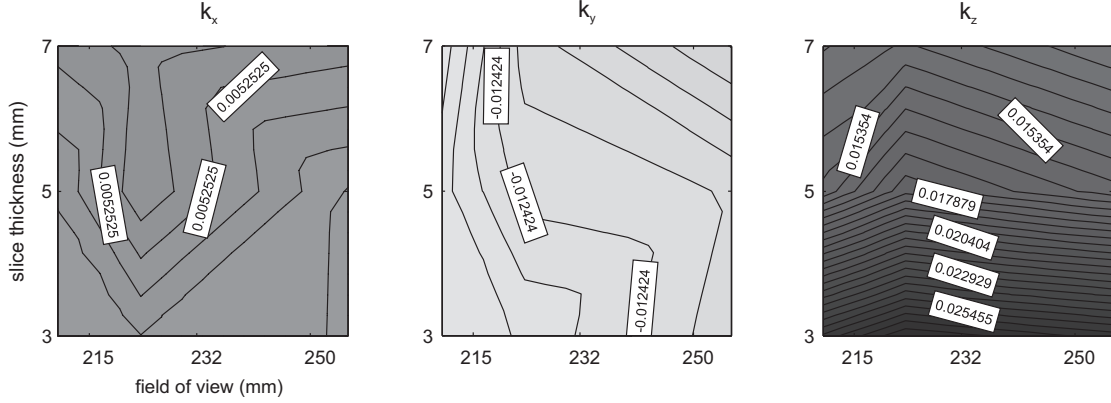


Fig. 2.15.: Plot of fitted k -parameter for every series over field of view and slice thickness for the series acquired on a Siemens Magnetom Vision

b -value on x , y or z . Thus, Fig. 2.15 shows the largest deviations in k_z with values over 0.025. A gradient from thicker slices to thinner slices is clearly noticeable for the parameter k_z (Fig. 2.15c), since the z -direction represent the slice encoding direction and imaging gradients aligned along this axis are scaled by $1/SL$. The second largest deviations were found for parameter k_y (Fig. 2.15b) with a negative sign, meaning that diffusion weighting in y direction is less than expected by the diffusion gradients. A gradient from larger field of view to smaller field of view is recognizable, which demonstrates the scaling of the imaging gradients in y -direction by $MATRIX/FOV$. The smallest deviations were found for the parameter k_x (Fig. 2.15a). For this map we had expected a similar gradient as shown in (Fig. 2.15b), since the imaging gradients in x -direction are also scaled by the factor $MATRIX/FOV$, but the deviations within the map are so small that a dependence on that factor is not emphasized.

Data set 3 The results for the DTI-EPI series acquired on the Siemens Magnetom Sonata are presented in the same manner done for *data set 2*. Fig. 2.16a shows that the diagonal diffusion tensor elements derived using the uncorrected b -matrices deviate the more the slice thickness as well as field of view is reduced. The correction by estimating the k -parameter and applying them to calculate corrected b -matrices for every series separately reduces the standard deviation shown in Fig. 2.16b by a factor of 4 to 6. The correction of b -matrices using the k' -parameter, which should be independent of the protocol settings, fails as shown by the calculated standard deviation of diagonal diffusion tensor elements after correction (Fig. 2.16c). An explanation for the failure is given by plotting the fitted k -parameter over field of view and slice thickness. As shown

2. MRI of diffusion

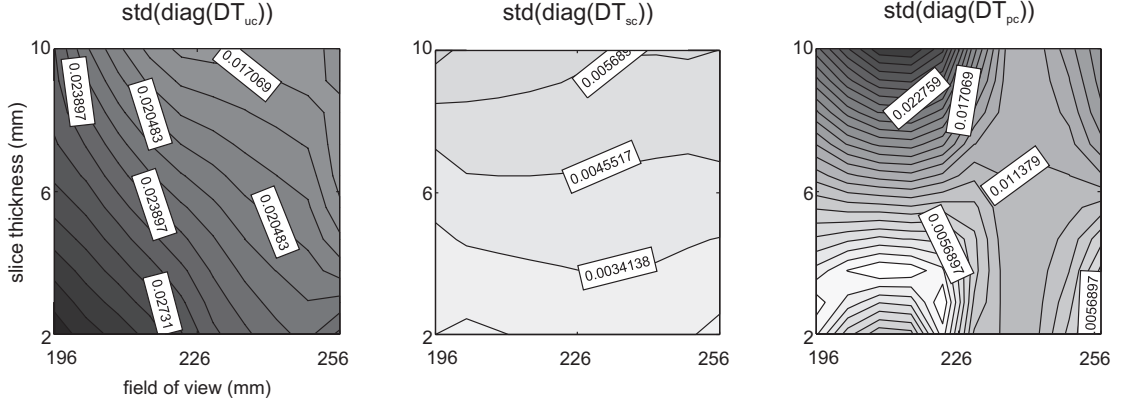


Fig. 2.16.: Standard deviation of diagonal tensor elements plotted by means of field of view and slice thickness for a) uncorrected Diffusion Tensors, b) single correct Diffusion Tensors and c) protocol corrected Diffusion Tensors for DTI-EPI series acquired on a Siemens Magnetom Sonata.

in Fig. 2.17 we found a gradient for the k_x -parameter (Fig. 2.17a), which tends mostly in the direction of a reduced field of view. However, the first mismatch was found for the k_y -parameter map, which shows a gradient but forcing in the direction of reduced slice thickness, whereas we had expected a gradient in the direction of reducing the field of view. For the k_z -parameter we found also a dependence on the slice thickness, which is alright, however, the gradient points in the direction of thicker slices, which does not correspond to the assumption of larger imaging gradients in slice direction with reduced slice thickness.

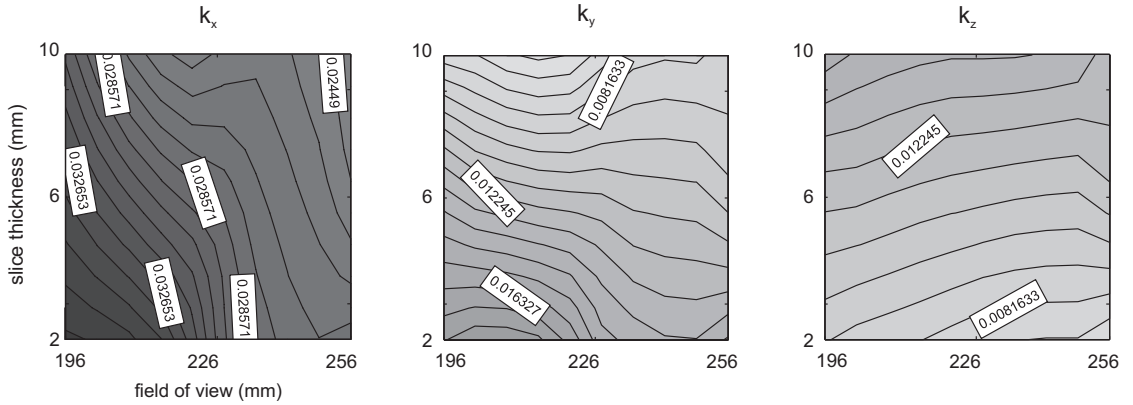


Fig. 2.17.: Plot of fitted k -parameter for every series over FOV and SL for the data set acquired on a Siemens Magnetom Sonata.

Implication and application of cross term correction

In this section the possibility to experimentally estimate the contribution of the imaging gradients to the diffusion weighting factor (b -value) in diffusion weighted MR acquisitions with the help of an isotropic phantom. Thereby, three different sequence techniques were employed. A conventional spin-echo sequence with additional diffusion gradients (PFG sequence, cf. Fig. 2.6) and full access to all gradient parameters was used to analyze the proposed approach and to compare the results with the analytical solution. Two different DTI-EPI sequences were employed on two different MR scanners (Siemens Magnetom Vision and Sonata). The deviation of the diffusion weighting represented by the b -value was estimated by assuming an isotropic diffusion tensor realized by using an isotropic water phantom. These deviations were investigated for different protocol settings to prove their dependence on the strength of the imaging parameters and to obtain the modified correction parameters, which are independent of the protocol settings. We found that the correction procedure applies well for single measurements for a given protocol setting in every case. The dependence of the protocol parameters (field of view, slice thickness) was confirmed for the spin-echo sequence and the DTI-EPI sequence at the Siemens Vision MR Scanner. The DTI-EPI sequence at the Siemens Sonata Scanner did not follow the assumption, that the imaging gradients in read-out and phase encoding direction are scaled by the factor of Matrix/FoV and the gradients in slice direction are scaled by $1/SL$. In this case the sequence is designed to adjust the imaging and diffusion weighting gradients in their scale and timing, if the protocol setting were changed. Hence, a protocol independent correction of the b -matrices is not possible. Nevertheless, a correction for specified acquisition settings is possible and reduces the error in the b -matrices.

The results for *data set 1* showed, that a complete cancellation of cross-terms influence could be achieved by applying a direction scheme, which acquires for every spatial direction also the corresponding opposed direction. For this reason, the cross-term is applied once with positive and once with negative sign for a direction pair. Thus, during the calculation of the diffusion tensor the error is canceled. The effect applies partially if more than 6 diffusion weighting directions are used to obtain the six unknown of the symmetric diffusion tensor. The complete procedure could be extended to include the amount of diffusion weighting given by the b -value, since the k -parameters are proportional to the square root of the b -value. The consideration of the b -value in the correction procedure would then change from a relative to an absolute correction. In this case exact b -values, which represent only the amount of diffusion weighting due to diffusion sensitized gradients, have to be warranted.

The presented method allows a simple detection and correction of cross-term contribution to b -matrices in diffusion tensor imaging. There is no need to have access

to the sequence code get an parameterized expression for the b-matrices for a given sequence. The correction method can also be performed independently of the chosen protocol settings, but only if the timings of all gradients is not changed.

2.4. Diffusion tensor imaging

2.4.1. MR diffusion weighted sequences

As we have learned from the theory section (cf. 2.2.2), the signal attenuation in diffusion weighted imaging correlates with the strength of weighting represented by the b-value and the diffusion constant. To image the diffusion constant voxel by voxel, one has to acquire an image with and without diffusion weighting. In general, all MR imaging sequences can be modified to generate a diffusion weighted MR signal, however not all sequences are suited for in vivo DWI. Although a variety of imaging sequences has been proposed for diffusion imaging [58, 59, 60], the most popular sequence type is echo-planar imaging [61, 62, 63]. With echo-planar imaging (EPI), the entire set of echoes needed to form an image is collected within a single acquisition period (single shot) of 25-100 ms [34]. The echo is typically a spin-echo, so that the diffusion sensitization gradient are placed right before and after the 180° -Pulse. However, the applied gradient pulses have higher intensity and longer duration than in any other well known MRI sequence, resulting in comparatively large and persistent eddy currents. When the eddy current decays slowly, so that a residual field remains during the image readout, the field behaves like an additional spatial encoding gradient field and causes distortion of the image. Since diffusion tensor imaging relies on the repeated measurement of diffusion weighted images with different weighting directions, the diffusion sensitized gradients are applied in different combination on the three axis (x,y and z). This leads to different distorted images, which can not be superimposed without correction. The most elegant way to reduce the effect of eddy current distortion was introduced by Reese et al. [57]. They proposed an improved spin-echo (SE) diffusion sequence that displays less distortion and consequently improves image quality by adding a second refocusing pulse which provides better image quality with less distortion at no cost in scanning efficiency or effectiveness, and allows more flexible diffusion gradient timing. By adjusting the timing of the diffusion gradients, eddy currents with a single exponential decay constant can be nulled, and eddy currents with similar decay constants can be greatly reduced. This sequence is referred as diffusion weighted Twice-Refocused Spin Echo EPI (dwTRSE-EPI) and serves as basis for almost every standard diffusion weighted sequence for in-vivo measurements. Fig. 2.18 shows the timing diagram of the TSRE sequence and buildup and decay of eddy currents due to the gradient switching.

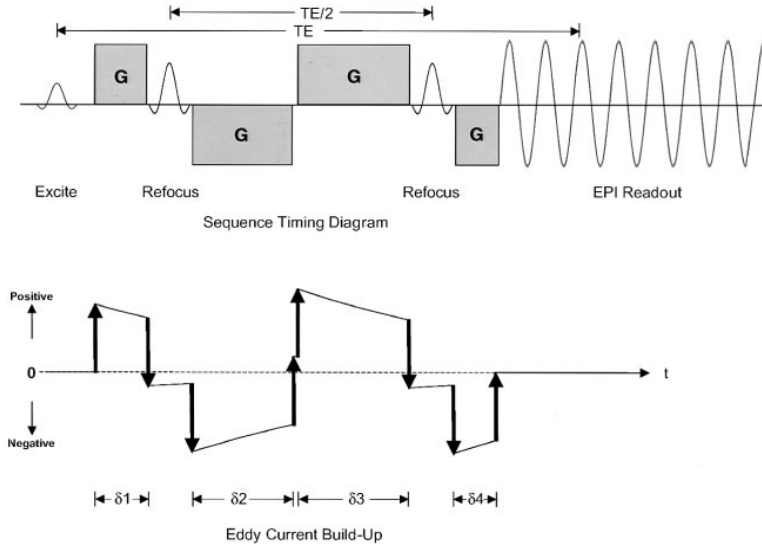


Fig. 2.18: Timing diagram of the diffusion weighted TSRE sequence. Note that the inserted diffusion gradients \mathbf{G} of length δ_1 , δ_2 , δ_3 and δ_4 do not have the same appearance as shown in the simple PGSS sequence (cf. 2.6). Below the graph the timing diagram of the buildup and decay of eddy currents due to the gradient switching is shown (adapted from Reese et al. [57]).

The on and off diffusion gradient transitions that generate the eddy currents are shown with bold black arrows. Knowing the principle eddy current decay time constant, diffusion gradient lengths can be calculated so that eddy current buildup is nulled prior to readout. Additionally it can be shown, that the flexible sequence timing in TRSE allows shorter echo times for the same b-value compared to Stejskal-Tanner PGSE sequence (cf. Fig. 2.6). However, the echo times (TE) are still very long (80-100 ms). Since the gradient amplitude is limited due to technical issues, one has to apply these gradients long enough to gain sufficient diffusion weighting which leads to longer echo times. Thus, local field distortions, especially in the frontal sinus or in regions near the temporal bone, caused by magnetic susceptibility variations are a severe problem. These susceptibility variations are difficult to correct, even with high-order shimming coils, and they increase with the field strength B_0 . The recent advent of parallel imaging helps to reduce susceptibility-induced artifacts by reducing the echo train length and thereby the amount of time that the off-resonant spins accumulate phase errors. Fig. 2.19 shows two axial slice positions (top row, bottom row) acquired with and without readout acceleration. It is clearly seen, that the susceptibility artifacts are reduced with increased readout acceleration which in turn reduces the required echo time. Thus, all diffusion studies which rely on well defined anatomic replication of the scanned object, should employ a parallel acquisition technique if available. The disadvantage with parallel imaging is that the signal to noise ratio (SNR) increases with increasing acceleration factor and is spatial depended. The reduced SNR can be overcome by repeated scans and subsequent averaging at the expense of scan time.

In addition to the widely used dwTRSE-EPI sequence, many other sequences have been developed for diffusion weighted imaging. One promising technique is based on

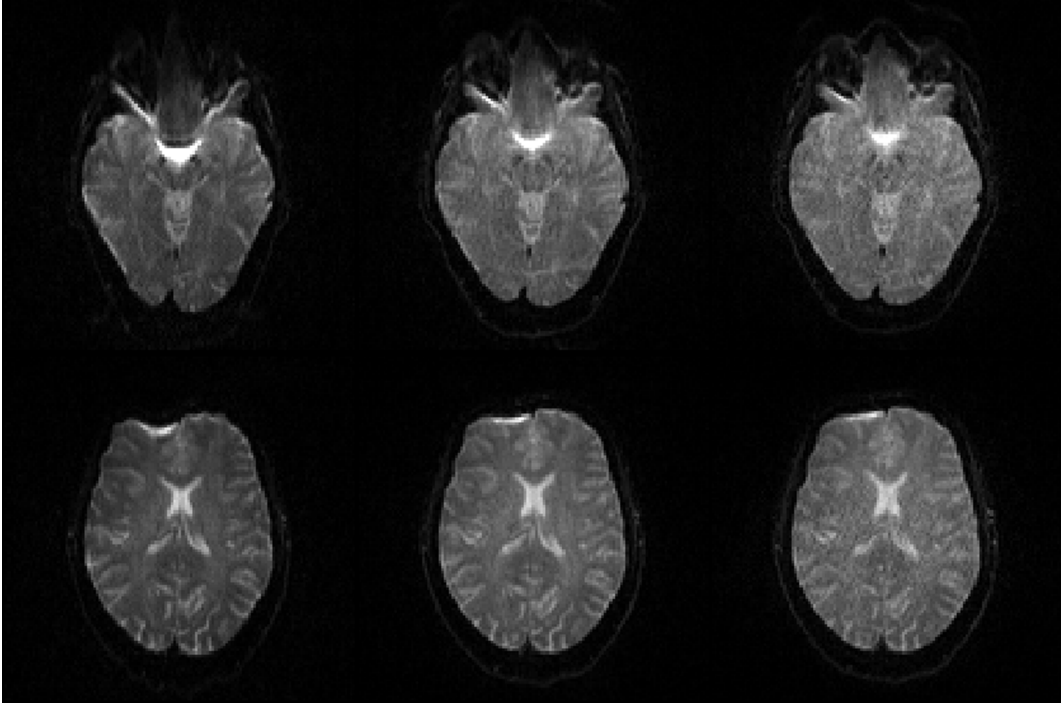


Fig. 2.19.: Two axial slices (upper and lower row) acquired using echo planar imaging with different acceleration factors (from left to right: without acceleration, 2x, 3x). The parallel imaging technique allows reduced echo times (from left to right: 94, 83 and 77 ms).

RARE (rapid acquisition with relaxation enhancement) pulse sequence [60], however implementing diffusion weighting into such a sequence is not straightforward. Additionally, this type of sequence is more sensitive to motion artifacts and has a lower signal to noise ratio, compared to EPI. Similar limitations apply using stimulated echo pulse sequences (STEAM) [58, 64] and spin echo (SE) or fast spin echo sequences [65, 66].

2.4.2. Determination of the diffusion tensor

If tissue structures have a non-spherical geometry with water diffusion boundaries, a scalar diffusion coefficient D is no longer sufficient to describe the diffusion process. As shown in section 2.2.2 the signal attenuation due to diffusion gradients can be related to the diffusion tensor (cf. Eq. 2.38), which can not be reduced to a scalar measure in the presence of anisotropy. To determine the six unknown parameters of the symmetric diffusion tensors, one has to acquire at least seven images: one with a zero b -value to obtain S_0 , and six with nonzero b -values and diffusion gradients with different orientations which are not collinear and not coplanar. From these images six different signal attenuations E_1, \dots, E_6 are calculated. Due to the change of the diffusion gradient directions changes different b -matrices are obtained for each E_i . These b -matrices

have to be calculated according to Eq. 2.39 to take into account diffusion and imaging gradients as well as cross-terms. If we use the sum notation of Eq. 2.38, as shown in Eq. 2.40, we can setup a system of linear equations (Eq. 2.66), which has to be solved for each image voxel to determine the coefficients of the diffusion tensor.

$$\ln \begin{bmatrix} E_1 \\ E_2 \\ E_3 \\ E_4 \\ E_5 \\ E_6 \end{bmatrix} = \begin{bmatrix} b_{xx_1} & 2b_{xy_1} & 2b_{xz_1} & b_{yy_1} & 2b_{yz_1} & b_{zz_1} \\ b_{xx_2} & 2b_{xy_2} & 2b_{xz_2} & b_{yy_2} & 2b_{yz_2} & b_{zz_2} \\ b_{xx_3} & 2b_{xy_3} & 2b_{xz_3} & b_{yy_3} & 2b_{yz_3} & b_{zz_3} \\ b_{xx_4} & 2b_{xy_4} & 2b_{xz_4} & b_{yy_4} & 2b_{yz_4} & b_{zz_4} \\ b_{xx_5} & 2b_{xy_5} & 2b_{xz_5} & b_{yy_5} & 2b_{yz_5} & b_{zz_5} \\ b_{xx_6} & 2b_{xy_6} & 2b_{xz_6} & b_{yy_6} & 2b_{yz_6} & b_{zz_6} \end{bmatrix} \begin{bmatrix} D_{xx} \\ D_{xy} \\ D_{xz} \\ D_{yy} \\ D_{yz} \\ D_{zz} \end{bmatrix} \quad (2.66)$$

As seen in Eq. (2.66), the diffusion tensor elements D_{yx} , D_{zx} and D_{zy} do not appear. Due to the symmetry of the diffusion tensor these elements equal D_{xy} , D_{xz} and D_{yz} and their contribution is considered with a factor of 2 in the corresponding b -matrix elements b_{xy} , b_{xz} and b_{yz} . When the number of gradient directions exceeds six, the tensor elements can be obtained using least-square fitting algorithm, such as singular value decomposition (SVD). The number of diffusion gradient directions used in DTI data acquisition along with the number of spatial distribution of the directions at a given number are usually referred to as *diffusion gradient scheme*. In the literature there are conflicting opinions as to whether it is more beneficial to use a large number of gradient sampling orientations than to use a smaller number of carefully chosen orientations. Increasing the number of directions typically improves the precision of DTI tensor element calculation, however the gain in image quality of the diffusion tensor maps becomes progressively less when the number of directions exceeds 25. Jones et al. [67] showed that at least 20 unique sampling orientations are necessary for a robust estimation of anisotropy, whereas at least 30 unique sampling orientations are required for a robust estimation of tensor-orientation and mean diffusivity. However, for a given specific number of directions, there are infinite ways to distribute the non-collinear gradient directions in 3D space. Actually, it is common consensus to distribute the diffusion gradients as uniformly as possible across the three dimensions [68, 69, 70, 71]. For the selection of a proper gradient scheme the so-called condition number has to be minimized [69]. If we introduce α_i as a six-dimensional vector with the b -matrix elements written in one line

$$\alpha_i = (b_{xx_i} 2b_{xy_i} 2b_{xz_i} b_{yy_i} 2b_{yz_i} b_{zz_i}) \quad (2.67)$$

2. MRI of diffusion

and build up a matrix \mathbf{A} of the different b -matrices, which corresponds to the matrix shown in Eq. 2.66,

$$\mathbf{A} = (\alpha_1, \alpha_2, \dots, \alpha_N)^T \quad (2.68)$$

we can calculate the condition number by

$$\text{cond}(\mathbf{A}) = \|\mathbf{A}\| \|\mathbf{A}^{-1}\|. \quad (2.69)$$

with $\|\cdot\|$ representing the norm of a matrix. A condition number close to 1 leads to low variances in the apparent diffusion coefficient (ADC) and fractional anisotropy (FA).

2.4.3. Scalar measures

The diffusion tensor is defined in the laboratory frame, which means that the diffusion coefficient in z-direction represents the amount of diffusion parallel to the B_0 static magnetic field of the MR scanner. The directional representation of a diffusion tensor in an acquired voxel depends on the orientation of the scanned object in the scanner system. To overcome this limitation one has to diagonalize the diffusion tensor using eigenvalue analysis.

$$\begin{bmatrix} D_{xx} & D_{xy} & D_{xz} \\ D_{yx} & D_{yy} & D_{yz} \\ D_{zx} & D_{zy} & D_{zz} \end{bmatrix} = \begin{bmatrix} \nu_{x1} & \nu_{x2} & \nu_{x3} \\ \nu_{y1} & \nu_{y2} & \nu_{y3} \\ \nu_{z1} & \nu_{z2} & \nu_{z3} \end{bmatrix} \begin{bmatrix} \lambda_1 & 0 & 0 \\ 0 & \lambda_2 & 0 \\ 0 & 0 & \lambda_3 \end{bmatrix} \begin{bmatrix} \nu_{x1} & \nu_{x2} & \nu_{x3} \\ \nu_{y1} & \nu_{y2} & \nu_{y3} \\ \nu_{z1} & \nu_{z2} & \nu_{z3} \end{bmatrix}^T \quad (2.70)$$

or in reduced matrix notation

$$\mathbf{D} = \mathbf{V} \cdot \mathbf{\Lambda} \cdot \mathbf{V}^T. \quad (2.71)$$

The elements, λ_1 , λ_2 and λ_3 , are known as the eigenvalues of the matrix. Their sum represent the trace of the matrix. The trace of a matrix is rotationally invariant, which means that it has the same numerical value as the sum of the diagonal elements of the diffusion tensor (D_{xx} , D_{yy} , D_{zz}). If one eigenvalue is considerably larger than the other two, the corresponding eigenvector is referred to as principal diffusion direction. The eigenvalues and eigenvectors can be used to create a graphical representation of the diffusion tensor as an ellipsoid (Fig. 2.20). Once the principal eigenvalues are known, a number of scalar diffusion parameter can be derived. The apparent diffusion coefficient (ADC), for example, which is the average of the eigenvalues (cf. Eq. 2.75), can be mapped voxel by voxel as shown in Fig. 2.21. To visualize the location of anisotropic voxel, fractional and relative anisotropy can be calculated using Eq. 2.73 and 2.74 [72]. Both are based on the standard deviation of the eigenvalues, but normalized by different

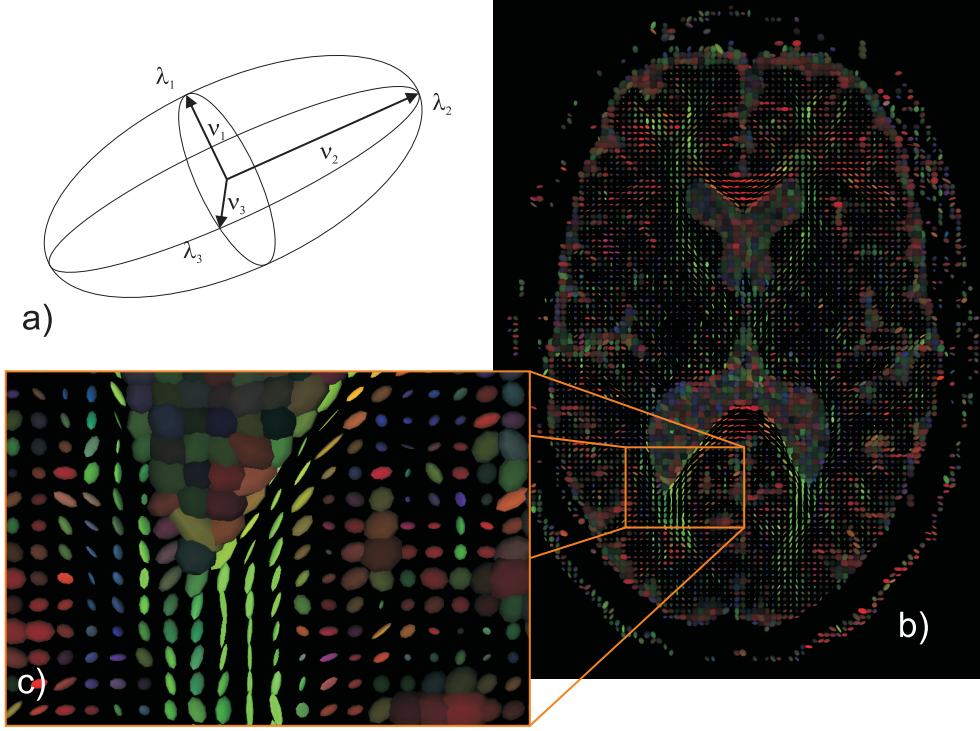


Fig. 2.20.: a) Representation of anisotropic diffusion tensor described by diffusion ellipsoid with the semi-axes equal to the amplitude of the diffusion tensor eigenvalues λ_1 , λ_2 and λ_3 . The axis of the ellipsoid coincide with the eigenvectors ν_1 , ν_2 and ν_3 . The right image shows the reconstruction of diffusion ellipsoids for each voxel of an axial slice of a human head.

denominators and coefficients. Fractional anisotropy ranges from 0 to 1 and has been found to be more sensitive at low anisotropies compared to relative anisotropy (RA) [73]. RA ranges from 0 to $\sqrt{2}$ and is linear over a wide range of diffusion anisotropy found in the human brain.

$$FA = \sqrt{\frac{3}{2}} \sqrt{\frac{\sum_{i=1}^3 (\lambda_i - ADC)^2}{\sum_{i=1}^3 \lambda_i^2}}, \quad (2.72)$$

$$RA = \frac{1}{\sqrt{3}ADC} \sqrt{\sum_{i=1}^3 (\lambda_i - ADC)^2}, \quad (2.73)$$

and

$$VR = \frac{\lambda_1 \lambda_2 \lambda_3}{ADC^3}, \quad (2.74)$$

where

$$ADC = \frac{\lambda_1 + \lambda_2 + \lambda_3}{3}. \quad (2.75)$$

2. MRI of diffusion

A special case of anisotropic maps is the color-coded fractional anisotropy map (see Fig. 2.21 - cFA). The color components are derived from the eigenvector components of the corresponding principal diffusion direction; in other words, the components of the vector with the largest eigenvalue [74]. In most cases the following convention applies: *red* represents diffusion along the x-axis, *green* along the y-axis and *blue* along the z-axis. In case of a human subject, imaged supine (lying on the back in the scanner), the colors correspond to left-right (red), anterior-superior (green) and superior-inferior (blue) orientation (see also Fig.2.21).

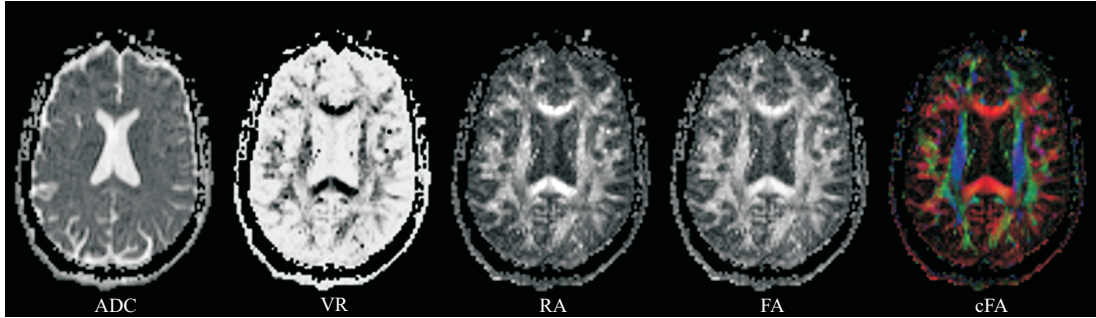


Fig. 2.21.: Different scalar measures derived from the diffusion tensor. From left to right: apparent diffusion coefficient (ADC), volume ratio (VR), relative anisotropy (RA), fractional anisotropy (FA) and color coded fractional anisotropy (cFA).

3. Volume conductor modeling

3.1. Introduction

Synchronized neuronal currents or electrical activities are capable of generating electromagnetic fields sufficiently large to be measured outside the body by using, for example, electro/magnetoencephalography (EEG/MEG) in the case of the brain or electro/magnetocardiography (ECG/MCG) in case of the heart. The spatial distribution of the underlying currents can then be estimated from the measured electromagnetic fields through a model-based inversion procedure that is also known as electromagnetic source imaging (ESI) or source localization depending on the type of the applied method. Within this inverse procedure the so-called forward problem has to be solved, in which the electromagnetic field is calculated at the sensor positions for given source positions employing a volume conductor and the quasi-static Maxwell Equations. The latter describes the interrelationship between electric field \vec{E} , magnetic field \vec{B} , electric displacement \vec{D} , and electric current density \vec{J} , and can be written in vector notation as follows [75]

$$\nabla \times \vec{E} = 0 \quad (3.1)$$

$$\nabla \times \vec{B} = \underline{\underline{\mu}} \vec{J} \quad (3.2)$$

$$\nabla \cdot \vec{D} = 0 \quad (3.3)$$

$$\nabla \cdot \vec{B} = 0. \quad (3.4)$$

The corresponding material equations are:

$$\vec{D} = \underline{\underline{\epsilon}} \vec{E} \quad (3.5)$$

$$\vec{J} = \underline{\underline{\sigma}} \vec{E} \quad (3.6)$$

The material properties are represented by $\underline{\underline{\epsilon}}$ the electrical permittivity, $\underline{\underline{\mu}}$ the magnetic permeability and $\underline{\underline{\sigma}}$ the specific electric conductivity tensors. Permittivity as well as conductivity are assumed to be constant considering biological tissue in the low fre-

3. Volume conductor modeling

quency domain. These material properties are used in the volume conductor models (e.g. boundary element models, finite element models) in order to solve the forward problem. The most important parameter is the specific electric conductivity or its reciprocal - resistivity. The influence of the conductivity on EEG and MEG forward problems as well as on the inverse solution has been shown in several publications. Haueisen et al. [76] investigated the variation of the conductivity values in the vicinity of the source and of the electrode positions and reported that a 50 % change of the conductivity influences the estimated dipole strength significantly. Pohlmeier et al. [77] demonstrated that source localization errors due to incorrect values of the conductivity of the skull can be neglected; however, these authors found that misclassification of the different compartments of the skull (spongiosa and compacta) may lead to serious localization errors.

In the following sections the different methods to measure conductivity in biological tissues are briefly introduced. In particular, it is dealt with the non-invasive determination of the conductivity tensor based on the effective medium approach. The last part of this chapter describes the necessary steps to generate high resolution finite element models with anisotropic conductivity using MRI data acquisition and various image post processing methods.

3.2. Measurement of tissue conductivity

3.2.1. Invasive methods

The most invasive measurements of conductivity at low frequencies are based upon in vitro animal experiments and were performed 40 years ago [25, 26, 27, 78]. However, such invasive measurements are very difficult to perform. Technical difficulties, like polarization or transition resistance, can lead to largely varying results and additional factors, like age, pathology, environmental factors or physical constitution, also affect the measurements [28, 79, 80]. An invasive measurement is typically performed by directing an electrical current through the tissue of interest and simultaneously acquiring the occurring potential difference. In the case of brain tissue, the current is directed through extra cellular space (approx. 20 % [81, 82]), neurons and glia cells. If one measures MEG and EEG the volume current runs only through extra cellular space and glia cells, since the neurons are the active generator. The discrepancy in the conditions for the measurement of MEG/EEG is expressed by the apparent conductivity and it has been shown that the apparent conductivity can be 1.5 times larger compared to the conductivity of the extra cellular space [80]. It can be assumed that the conductivity, which is decisive for MEG/EEG volume conductor models, ranges between the

apparent conductivity and the conductivity of the extra cellular space.

Table 3.1 lists specific electrical conductivities which are derived from in vivo measurements for the most important tissue types of the head. The values which are used in this work are given in a separate column. The table reflects the already mentioned

Tab. 3.1.: Conductivities for different tissues of the head derived from in-vivo measured. All values are given in S/m.

tissue type	conductivities from literature	used conductivity
csf	1.54 [25], 1.79 (rabbit) [25], 1.79 (human) [83]	1.79 [29]
skin/connective tissue	0.43 (skin) [25], 0.2 (con. tis.) [29]	0.33 [84]
bone/skull	0.0015 [85], 0.0062 [25]	0.0042 [84]
gray matter	0.45 [26], 0.48 [27], 0.31 [86], 0.23 [28]	0.337 [29]
white matter	0.134 [28], 0.104 [27], 0.118/1.12 (perpendicular/parallel) [78], 0.3 [26], 0.083/0.57(perpendicular/parallel) [86]	0.14 [29]

variations of invasively measured conductivities found in the literature and underlines the still existing need to explore new approaches for reliable determination of the important physical parameter. A solution may be found by using non-invasive methods which are mostly based on magnetic resonance imaging.

3.2.2. Non-invasive methods

The most common non-invasive conductivity mapping method is Magnetic Resonance Electric Impedance Tomography (MR-EIT) [87, 88]. MR-EIT is currently performed in two different variants. One is to apply low frequency sinusoidal currents via electrodes which are attached to the body surface and is therefore called applied-current electrical impedance tomography (ACEIT) [89, 87, 88, 90]. The second approach induces currents by time-varying magnetic fields (e.g., 50 kHz) and is known as induced-current electrical impedance tomography (ICEIT) [91]. Both variants can be performed without magnetic resonance [91], but then certain assumptions have to be made in order to reconstruct a cross-sectional map of the investigated object. With MRI this information is derived during data acquisition, since the current density map which is necessary to calculate the conductivity distribution is computed from the phase images acquired with special pulse sequences. This technique is also known as MR current density imaging (MRCDI). Despite the limitation that only the z-component of the induced current can be imaged by MRCDI, Pyo et al. described a theoretical solution for the x- and y-component by utilizing an auxiliary injection current [92]. This approach would be

3. Volume conductor modeling

applicable to objects with anisotropic conductivity and is more robust against measurement noise in comparison to the approach published by Seo et al. [93]. However, the approach to derive conductivity values from CDI is based on an ill-posed inverse problem and requires the application of external currents sufficiently large to produce magnetic field contrast visible by MRI.

Another possibility is Hall Effect Imaging [94, 95], which is based on the detectable voltage from a conductive object moving in a magnetic field. Imaging is performed in this case with ultra sound technique. Besides the dependence of a propagating ultra sound wave, Hall effect imaging is not quantitative and thus only suitable for imaging conductivity contrasts.

A very promising new technique is called *Electric Properties Tomography* (MR-EPT) [96, 97, 98], which extracts the patients electric properties using a standard MR system. With the EPT approach, the spatial transmit and receive sensitivity distributions of the applied RF coil have to be measured and the electric field of the RF coil has to be calculated. According to the Maxwell equations, dividing the spatial derivatives of these sensitivities by the electric field leads to the desired spatial distribution of conductivity and permittivity. Thus, MR-EPT does not apply externally mounted electrodes, currents, or RF probes and EPT is not based on an inverse problem. The spatial resolution of the reconstructed property maps is of the order of the spatial resolution of the measured MR-images. However, the disadvantages of this method is that the derived properties (conductivity and permittivity) are measured for high frequencies (~ 63 or ~ 124 MHz depending on the used magnetic field strength (1.5 or 3 T)) and actually it is limited to measure these properties parallel to the magnetic field.

A completely different non-invasive approach was proposed by Tuch et al. [42], which is based on Diffusion Tensor Magnetic Resonance Imaging and follows the assumption, that the properties diffusion and conductivity share the same eigenvectors in a two-phase anisotropic medium. This approach will be explained in more detail in the following section.

3.3. Effective medium approach

The following approach of the conductivity tensor mapping from diffusion tensor data was introduced by Tuch et al. [42] and is often cited as *Effective Medium Approach* (EMA). Since the derivation of the conductivity tensor from the diffusion tensor is an essential part of further methods presented, the derivation is expressed in this section. Additionally, the linear factor to convert diffusion tensor eigenvalues to conductivity tensor eigenvalues, which was found by Tuch et al. [42], was determined using own

measurements.

The model starts with the estimation of the statistical moments of the microstructure from the observed diffusion tensor. It is further assumed that the cell membrane is freely permeable to water and impermeable to charge-carriers on the experimental time scale (≈ 50 ms). According to Sen and Torquato [99], the effective transport tensor $\mathbf{\Lambda}$, denoting either the effective electrical conductivity tensor σ or the diffusion tensor \mathbf{D} , for a two-phase anisotropic medium of arbitrary topology which is macroscopically homogeneous but anisotropic is given by

$$(\phi_i \beta(\lambda_i, \lambda_e))^2 \mathbf{B}^{-1}(\mathbf{\Lambda}, \lambda_e \mathbf{U}) = \phi_i \beta(\lambda_i, \lambda_e) - \sum_{n=2}^{\infty} \mathbf{A}_n^{(i)} \beta(\lambda_i, \lambda_e)^n \quad (3.7)$$

where the variable ϕ_i denotes the inclusion (intracellular) volume fraction, \mathbf{U} is the identity tensor, and λ_i and λ_e are, the inclusion (intracellular) and host medium (extracellular) transport coefficients, respectively. In case of diffusion these coefficients represent intracellular (d_i) and extracellular (d_e) diffusion coefficients. Similarly for the conductivity, σ_i is the intracellular conductivity value and σ_e denotes the extracellular conductivity. The dimensionless contrast factors β and \mathbf{B} in Eq. 3.7 are defined as

$$\beta(x, y) = \frac{x - y}{x + 2y} \quad (3.8)$$

and

$$\mathbf{B}(\mathbf{X}, \mathbf{Y}) = (\mathbf{X} + 2\mathbf{Y})^{-1} (\mathbf{X} - \mathbf{Y}) \quad (3.9)$$

The tensors $\mathbf{A}_n^{(i)}$ contain microstructure information and they are defined as integrals over the n -point probability functions S_n^i , which give the probability of finding n -points within the inclusion (intracellular) phase. By setting $\mathbf{A}_1^{(i)} = -\phi_i \mathbf{U}$, the first term on the right-hand side of Eq. 3.7 can be embedded in the sum to give

$$(\phi_i \beta(\lambda_i, \lambda_e))^2 \mathbf{B}^{-1}(\mathbf{\Lambda}, \lambda_e \mathbf{U}) = - \sum_{n=1}^{\infty} \mathbf{A}_n^{(i)} \beta(\lambda_i, \lambda_e)^n \quad (3.10)$$

The sum on the right-hand side of the above equation can be made implicit by defining the concatenation $\mathbf{C}^{(i)} = (\mathbf{A}_1^{(i)} \mid \mathbf{A}_2^{(i)} \mid \dots)$, and, similarly, $\mathbf{G}_\lambda = (\beta_\lambda \mathbf{U} \mid \beta_\lambda^2 \mathbf{U} \mid \dots)^T$. Eq. 3.10 then becomes

$$(\phi_i \beta(\lambda_i, \lambda_e))^2 \mathbf{B}^{-1}(\mathbf{\Lambda}, \lambda_e \mathbf{U}) = -\mathbf{C}^{(i)} \mathbf{G}_\lambda \quad (3.11)$$

From Eq. 3.11 one can obtain a least-squares estimate $\hat{\mathbf{C}}^{(i)}$ from $\mathbf{C}^{(i)}$ based on the observed diffusion tensor \mathbf{D} by identifying $\mathbf{\Lambda}$ with \mathbf{D} and then multiplying from the

3. Volume conductor modeling

right by the right-handed Moore-Penrose pseudo-inverse, which takes into account that different geometries can give rise to the same effective transport, $\mathbf{G}_d^+ = \mathbf{G}_d^T(\mathbf{G}_d\mathbf{G}_d^T)^{-1}$ yielding

$$\hat{\mathbf{C}}^{(i)} = -(\phi_i\beta(d_i, d_e))^2 \mathbf{B}^{-1}(\mathbf{D}, d_e \mathbf{U}) \mathbf{G}_d^+ \quad (3.12)$$

Identifying \mathbf{A} in Eq. 3.11 with σ and equating $\hat{\mathbf{C}}^{(i)}$ and $\mathbf{C}^{(i)}$ gives

$$\beta(\sigma_i, \sigma_e)^2 \mathbf{B}^{-1}(\sigma, \sigma_e \mathbf{U}) = \beta(\sigma_i, \sigma_e)^2 \mathbf{B}^{-1}(\mathbf{D}, d_e \mathbf{U}) \mathbf{G}_d^+ \mathbf{G}_\sigma \quad (3.13)$$

Solving algebraically for $\mathbf{G}_d^+ \mathbf{G}_\sigma$ we obtain

$$\mathbf{G}_d^+ \mathbf{G}_\sigma = \frac{\beta_\sigma}{\beta_d} \left(\frac{\beta_d^2 - 1}{\beta_d \beta_\sigma - 1} \right) \mathbf{U} \quad (3.14)$$

The solution for σ yields

$$\sigma = \sigma_e \mathbf{B}^{-1}(\mathbf{F}, \mathbf{U}) \quad (3.15)$$

with

$$\mathbf{F} = \frac{\beta_d}{\beta_\sigma} \left(\frac{\beta_d^2 - 1}{\beta_d \beta_\sigma - 1} \right) \mathbf{B}^{-1}(\mathbf{D}, d_e \mathbf{U}) \quad (3.16)$$

An explicit linear approximation can be obtained from Eq. 3.16 by taking a series expansion in the intracellular diffusion

$$\sigma_\nu = \frac{\sigma_e}{d_e} \left[d_\nu \left(\frac{d_i}{3d_e} + 1 \right) + \frac{d_\nu^2 d_i}{3d_e^2} - \frac{2}{3} d_i \right] + O(d_i^2). \quad (3.17)$$

In order to test the cross-property relation experimentally, particularly the prediction of strong linearity made by Eq. 3.17, Tuch et al. performed diffusion tensor measurements and compared the diffusion eigenvalue data (d_ν) to reported invasive conductivity measurements (σ_ν) for corresponding anatomical regions. The plot of these data pairs is shown in Fig. 3.1 (left). The data and using Eq. 3.16 permit the determination of (σ_ν, d_ν) . Tuch et al. determined values for $\sigma_e = 1.52 \pm 0.251 \text{ S/m}$, $d_e = 2.04 \pm 0.506 \mu\text{m}^2/\text{ms}$ and $d_i = 0.117 \pm 0.0972 \mu\text{m}^2/\text{ms}$ Tuch et al. [42]. Assuming a simple linear relationship in the form of

$$\sigma_\nu = k(d_\nu + d_e). \quad (3.18)$$

they obtained numerical values for $k = 0.844 \pm 0.0545 \text{ S}\cdot\text{s}/\text{mm}^3$ and $d_e = 0.124 \pm 0.0540 \mu\text{m}^2/\text{ms}$ with a correlation coefficient of $r^2 = 0.945$. The data which were used by Tuch et al. for the correlation between diffusion tensor eigenvalues and conductivity tensor eigenvalues are shown graphically in Fig. 3.1. For comparison, the linear fit was reproduced with own measured diffusion coefficients from a healthy human subject. The results are shown in the right graph of Fig. 3.1. The numerical values derived for the own data

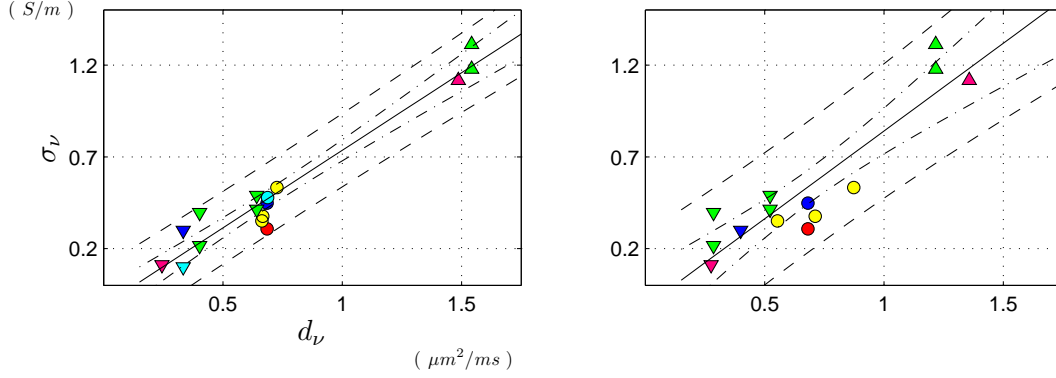


Fig. 3.1.: Graphical representation of the linear relationship between conductivity (σ_ν) and diffusion (d_ν) tensor eigenvalues as reported by Tuch et al. [42]. The conductivity values were taken from reported invasive measurements and the diffusion values from diffusion tensor MRI in the corresponding anatomical regions. The solid line depicts the linear fit, and the dashed lines the upper and lower confidence intervals on the linear fit. The left graph shows the original work of Tuch et al. [42] and the graph on the right side was created using own diffusion tensor measurements of a single healthy subject. The symbolic encoding of the different observations corresponds to the scheme used by Tuch. In detail: average over cortex (blue circle, [26]; (red circle, [86]), the average subcortical white matter perpendicular to the tract (blue inverted triangle, [26]), somatosensory cortex in three perpendicular directions (yellow circle, [100]), the parasagittal sulcus (light blue circle, [27]), the subcortical white matter beneath the parasagittal sulcus measured perpendicular to the tract (light blue inverted triangle, [27]), the cerebellum parallel (green triangle) and perpendicular (green inverted triangle) to the dominant fiber orientation [101], and the anterior internal capsule parallel (purple triangle) and perpendicular (inverted purple triangle) to the tract [78].

3. Volume conductor modeling

pairs are for $k = 0.9564 \pm 0.2647 \text{ S}\cdot\text{s}/\text{mm}^3$ and $d_e = 0.1206 \pm 0.2125 \mu\text{m}^2/\text{ms}$ with a correlation coefficient of $r^2 = 0.8378$.

Up to now an experimental proof of this approach is still missing. Oh et al. [102] showed in a phantom experiment using silk yarn a similar ratio for diffusion and conductivity measured parallel and perpendicular to the principal direction of the silk fibers. However, Akthari et al. [103] investigated freshly excised cortical tissue, in order to validate the EMA approach conducting diffusion tensor imaging as well as conductivity measurements. The authors found a negative, but not significant dependence of conductivity values to diffusivity, which is in contrast to the result derived by Tuch et al..

Besides the missing experimental evidence of the effective medium approach it has further limitations. First, a two phase medium is assumed, which is of course a reasonable simplification but surely not always applicable without any qualification. Second, the relationship is generated based on conductivity values measured 40 or more years ago mostly using animals. And third, the direct linear translation of diffusion eigenvalues to conductivity eigenvalues is problematic, since not all tissue types provide diffusion tensor data (e.g. skull) and high anisotropy can occur if one diffusion eigenvalue comes close to d_e or is lower than this value. Hence, different methods of relating the diffusion tensor to the conductivity tensor in order to assign these information to the used FEM models are proposed in 3.4.4.

3.4. Volume conductor construction

The different steps in creating anisotropic FE volume conductor models include data segmentation, coregistration of different image contrasts, tensor correction and adjustment and the generation of the mesh. These different steps are described in the following section.

3.4.1. MRI data segmentation

Volume conductor modeling typically starts with a T1w MRI volume scan. This MR contrast is known to provide good contrast between gray and white matter. The most common MR sequence which is applied for anatomical T1w images is called Magnetization Prepared Rapid Gradient Echo (MPRAGE) sequence. Typical protocol parameters for such a sequence are $TE = 3 \text{ ms}$, $TR = 2300 \text{ ms}$, $TI = 900 \text{ ms}$, flip angle $= 9^\circ$ with an acquisition time (TA) between 4 up to 10 minutes (depending if parallel acquisition is used or not) for a full isotropic volume with a resolution of 1 mm^3 . The following steps describe the segmentation of a MPRAGE data set into 5 different tissue types (gray

and white matter, skull, skin and cerebrospinal fluid).

Preprocessing In order to obtain reliable and reasonable results some preprocessing steps have to be performed. The most simple step is to average acquisitions of the same contrast type in order to get a higher signal to noise ratio. However, recent MR scanners, especially at higher fields (≥ 3 T) provide an acquisition quality that is sufficient for the following segmentation steps, so that repeated scans are not really necessary. Even the use of parallel acquisition provides images without losing too much quality but gaining acquisition speed (e.g. shorten the time of MR examination or acquire more data in the same amount of time). Nevertheless, higher fields and accelerated acquisition bring up new problems, which have to be considered. B1 field inhomogeneities and imperfect superposition of the antennas of a multi-channel coil may and in most cases they will lead to an inhomogeneous intensity distribution over the whole volume. This problem can be solved by applying an intensity correction algorithm iteratively [104].

The next preprocessing step lowers the noise of the image while preserving the tissue borders, which is very important for segmentation purposes. Therefore, an anisotropic filter is applied to the data. In order to use a priori information for the downstream segmentation process, the last preprocessing step co-registers the volume into the talairach standard space [105].

Cortical segmentation The first step toward cortical segmentation is to strip the skull in order to obtain the whole brain from a head scan. The gold standard to perform this task is still manual segmentation by an experienced observer; however, this procedure is very time consuming, demanding automatic approaches. Actually automatic approaches can be divided into three categories: region-based, boundary-based, and hybrid approaches. The *region-based methods* identify connected regions based on predefined criteria (typically intensity), employing thresholding, clustering, and morphological filtering to identify the targeted volume. While some published approaches are effective, region-based methods generally involve some degree of user interaction, and are sensitive to scanning parameters and intensity inhomogeneity. Different region-based skull stripping techniques were published by Atkins and Mackievich [106], Cox [107] or Lemieux et al. [108]. In general these approaches use thresholding and morphology techniques with subsequent filtering. One of the main drawbacks of these methods is that they suffer from over-segmentation, which is the reason why they are usually followed by a post-processing step to merge separate regions that belong to the same structure [109]. There are *Boundary-based methods*, which primarily rely on gradient information to locate the brain surface, usually modeled by an contour [110,111,112]. Compared to region-based methods, these approaches are more robust and less sensi-

3. Volume conductor modeling

tive to image artifacts, and require less user-interaction, however, their success often depends on the quality of initialization and manual adjustment to scanning parameters [109]. *Hybrid approaches* take advantage of both techniques in order to deal with the drawbacks. Such hybrid techniques were proposed by Shattuck and Leahy [113], who use adaptive anisotropic diffusion, edge detection and morphological erosions to identify the brain component. Other hybrid approaches deform the active surface under a gradient vector field computed from a binary edge map [114] or incorporate the nearly constant thickness of the cortex and use a coupled surface evolution to extract bounding surfaces of the cortex [115]. In general, such hybrid techniques give the best results to create volume conductor models. The method which was used in this work was proposed by Ségonne et al. [109]. It starts with the determination of global parameters, like coordinates of the centroid of the brain, maximal gray value for cerebrospinal fluid (CSF) and brain/head radius to determine a start point in the white matter and the upper and lower intensity bounds for white matter tissue. A watershed algorithm is applied to extract an initial brain volume, removing most of the nonbrain tissue, such as scalp, skull, neck tissue and so on. Ségonne et al. use a method which is based on the work by Hahn and Peitgen [116]. After the watershed computation, the segmented volume contains some non-brain tissue such as CSF or some parts of the skull, and often the full brain stem. Subsequently, a deformable model is applied, which incorporates geometric information, such as curvature, which will remove these regions. The successive correction of the watershed algorithm by comparing the brain outline with an atlas-based brain outline results in a very robust detection of the brain volume [109].

Further steps to segment or label the different parts of the brain are performed using a variety of quantities including image intensities, global position within the brain, positions relative to the neighboring brain structures as well as anatomical landmarks. Using T1 weighted MRI images the intensity alone is not able to distinguish between different brain segments - there is far too much overlap between intensity distributions. Additional MRI contrasts (e.g. proton density or T2 weighted) can help separate the different tissue classes, but spatial information is still required to make the classification unique [117].

The spatial information is supported by the use of a probabilistic atlas [118, 119, 120, 121]. In this type of atlas, information regarding the statistical properties of anatomical structures is stored in a space in which coordinates have anatomical meaning as opposed to the somewhat arbitrary coordinates in a raw image, which are dependent on the position, orientation, and shape of a subject's brain. Such an atlas helps to limit the number of possible tissue classes at a given position in the brain and it characterizes the spatial pattern of segments relative to another. For the segmentation process the individual brain data sets are registered to the atlas data and a class statistics (e.g.

means and covariance matrices) are obtained regionally throughout the atlas space [117]. Prior probabilities are computed via frequency histograms in the atlas space allowing the calculation that a given anatomical class occurs at a given atlas location. And finally, the prior probability of a given spatial arrangement of anatomical labels is incorporated into the final segmentation procedure. All these steps were performed using the Freesurfer software package [117, 109, 122].

After detailed subcortical segmentation the number of segments has to be reduced, since there are no conductivity information for all found segments. Therefore, an encoding table was setup, which translates the segment IDs generated by the Freesurfer software into a small number of IDs which are used during further segmentation process. The translation is shown in Table A.1. The resulting segments are shown as an overlay in Fig. 3.2b.

Skull The segmentation of the skull is the most difficult task, if only MR images are available. In typical MR contrast this tissue type gives a very low signal on the image and is hard to distinguish from background. However, this segment is very important for conductivity models, since this layer has – besides inner air volumes – the lowest conductivity. Misclassification of the skull segment can lead to significantly different results in EEG/MEG source localization [123, 124, 125]. In order to obtain the most reliable results for the skull segmentation, it is necessary to use T1 and T2 weighted MRI data sets. Both datasets have to be registered to each other. As long as the volumes are acquired during the same MR session and assuming no object motion it is sufficient to make use of the registration which can be generated using the meta information (slice positions and orientation) of both data sets. Otherwise registration using rigid transformation has to be performed. The segmentation itself can be performed using the brain extraction tool *BET2* [126]. This software extends the methods of a previous software version *BET* [112], by generating surface layers for the outer skin, inner and outer skull. Starting from the brain surface vertex positions, profiles perpendicular to the surface are generated running from 3 mm inside to 60 mm outside the surface using a trilinear interpolation with a step size of 0.5 mm. Using both profiles from T1 and T2 weighted volume the layer for outer skin and inner and outer skull are evaluated [127].

Ventricles and CSF The voxels which represent the ventricles (left, right, third) were already defined during the cortical segmentation. Thus, only the CSF which surrounds the brain volume (between pial surface and skull layer) has to be segmented. Manual selection starting from a T1 data set is very time consuming and difficult, since the signal of CSF is very low and hardly distinguishable from the skull layer. The skull layer, however, was already defined in the last step. Thus, one has to create a mask by

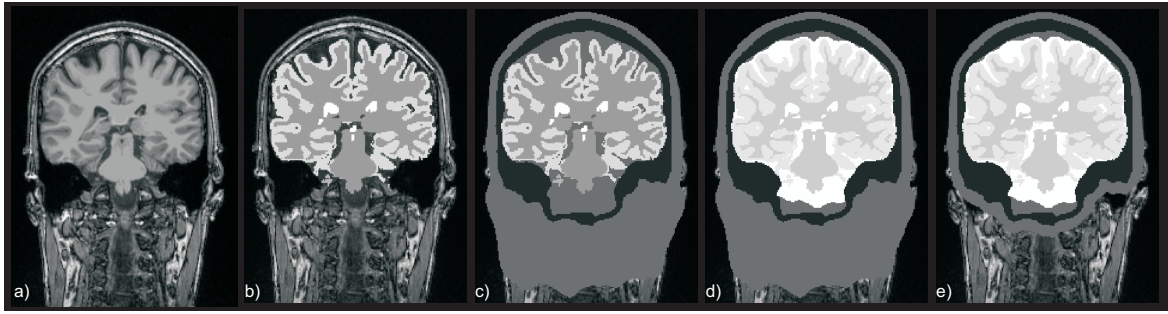


Fig. 3.2.: Steps during the segmentation process using a T1w data set: a) coronal slice of an already filtered T1w image, b) segmentation of gray and white matter as well as the ventricles, c) separation of the skull layer and the outer skin (fills also the unsegmented tissues within the skull), d) classification of the CSF and dilatation of gray matter in the direction of white matter, e) lower part of the segment removed.

ascribing every voxel which is within the inner skull layer and does not belong to the gray or white matter or to the ventricles to CSF. This mask should be compared to the apparent diffusion coefficient (ADC) volume. If voxels assigned to CSF by the previous procedure have a low ADC value (lower than $2 \mu\text{m}^2/\text{ms}$), these voxels should be reassigned to soft tissue. Such soft tissue segments mostly occur at the supra-mid-sagittal part of the brain.

Scalp and remaining segments Each voxel which is within the head surface and is not assigned to gray or white matter, CSF or skull segments is defined as scalp or soft tissue layer. Inner air volumes are neglected or assigned to soft tissue. However, since the final model is cropped at the lower part to reduce the size, the cavities (e.g. esophagus, air sinuses) are removed. This reduction of the model was achieved by generating a binary volume of the outer skull layer including everything inside. This binary volume was dilated iteratively in order to increase the object outline by 3 cm. An AND relation between the dilated object and a binary representation of the whole head object gives the final model outline. The final segmentation after the complete procedure is shown in Fig. 3.2e.

3.4.2. Spatial coregistration

In order to fuse data of different MRI acquisitions (e.g. T1 weighted anatomical data set with a diffusion tensor data set) one has to perform spatial coregistration. In case of diffusion tensor data, the fractional anisotropy map (FA map) (cf. 2.4.3) is aligned to the extracted brain volume derived from the T1w data set by using mutual information. Since the data usually do not have the same voxel size and slice thickness and suffer also from different geometric distortions, an affine transformation has to be performed

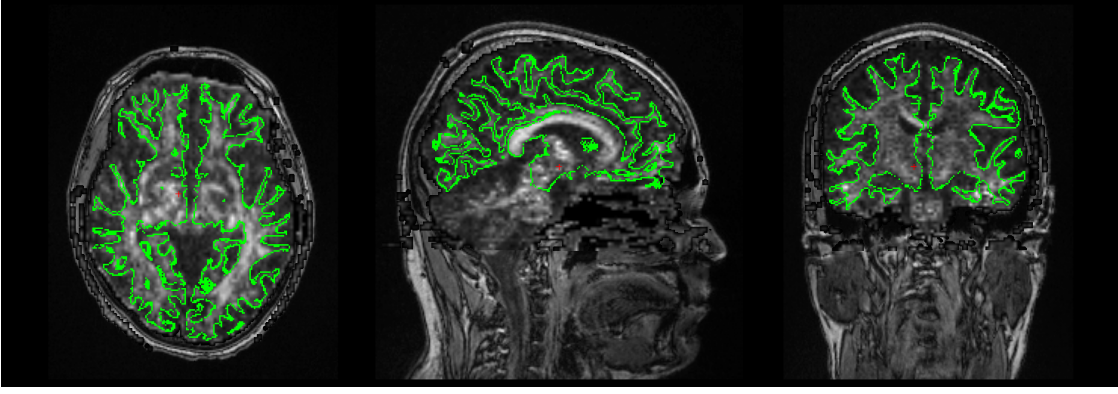


Fig. 3.3.: Result of the coregistration of a FA map volume to a T1w volume. From left to right: transverse, sagittal and coronal view.

to achieve good coregistration. The result of such a coregistration is shown in Fig. 3.3, where the FA map is overlaid on the corresponding T1w data set. In addition, the outline of the white matter mask which was derived from the segmentation processes is superimposed to demonstrate the quality of the coregistration procedure.

Usually, the diffusion tensor images are acquired with EPI sequences which are sensitive to local field inhomogeneities and thus producing distorted images, especially in regions of the frontal sinus and near the petrosal bone. Compensation of such deformations using affine linear transformation is limited. Thus, the acquisition should be performed with optimized sequence timings and parallel imaging technique if possible (cf. Fig. 2.19). In the optimal case (no geometric image distortions) the affine linear transformation corresponds to the rigid transformation. The calculated transformation matrix is then applied to the elements of the diffusion tensor data set. However, this only changes the spatial position of the tensors but not their orientation, which is still in the frame of reference of the MR scanner [128]. In order to correct this, one has to extract the rotation from the transformation matrix, which was used to align the tensor data set to the anatomical data set. If the linear transformation matrix (without the translation part) is given by

$$\mathbf{M} = \begin{bmatrix} M_{1,1} & M_{1,2} & M_{1,3} \\ M_{2,1} & M_{2,2} & M_{2,3} \\ M_{3,1} & M_{3,2} & M_{3,3} \end{bmatrix} \quad (3.19)$$

one can derive the rotation part, \mathbf{R} , by evaluating

$$\mathbf{R} = \mathbf{M} \sqrt{\mathbf{M}^T \mathbf{M}} \quad (3.20)$$

3. Volume conductor modeling

Finally the rotation matrix \mathbf{R} is applied to the tensor as given by

$$\mathbf{D}' = \mathbf{RDR}^T \quad (3.21)$$

Note that this transformation does not change the size or shape of the tensors, i.e. the eigenvalues are preserved, and only the orientation (eigenvectors) are affected.

However, this strategy has the limitation that the amount of reorientation can not vary over the image. Such a spatial variation of tensor reorientation can occur due to the nonrigid transformation part (shearing and stretching components) of the affine transformation matrix \mathbf{M} . This problem can be handled using the "Preservation of Principle Direction" (PPD) strategy proposed by Alexander et al. [128]. However, in intra-subject studies, where the transformation matrix between different image contrasts is nearly rigid, the benefit of the PPD strategy was not observed [128], so that in this work only the global reorientation strategy was used.

3.4.3. FE mesh generation

The last step in FE volume conductor modeling is the mesh generation, which represents the geometric and electric properties of the volume conductor. There are different approaches to generate such meshes from volume data, but in general they end up with tetrahedral or hexahedral elements. The latter element type was used in this work, which takes advantage of the spatial discretization given by the segmented volume. In Fig. 3.4 the steps of generating a hexahedral mesh are shown. The hexahedrization is performed by extracting the eight-nodes of the elements directly from corners of the voxels of the segmented volume (cf. Fig. 3.4, middle image).

Since the material interfaces are now characterized by abrupt transitions and right angles, a node shift was applied using the algorithm proposed by Camacho et al. [129]. This algorithm evaluates each node by determining the eight elements sharing this nodes. If a material type is represented by one, two or three elements, this material is designated minority elements. The node is then shifted into the direction of the centroid of the minority material type elements, there the node shift factor determines the shift length. If this factor is 1, the node is shifted on the position of the centroid of the minority material type elements. This would lead to elements with interior angles larger than 180° and negative Jacobian determinants. However, a node shift factor of less than 0.5 ensures positive defined Jacobian determinants for all hexahedral vertices after node shifting. The right subfigure in Fig. 3.4 shows the application of this procedure using a node shift factor of 0.49. The advantages of a smoothed hexahedral mesh using node shift was shown by Wolters et al. [130]. They found that node-shifting reduces both topography and magnitude errors in the EEG forward solution by more

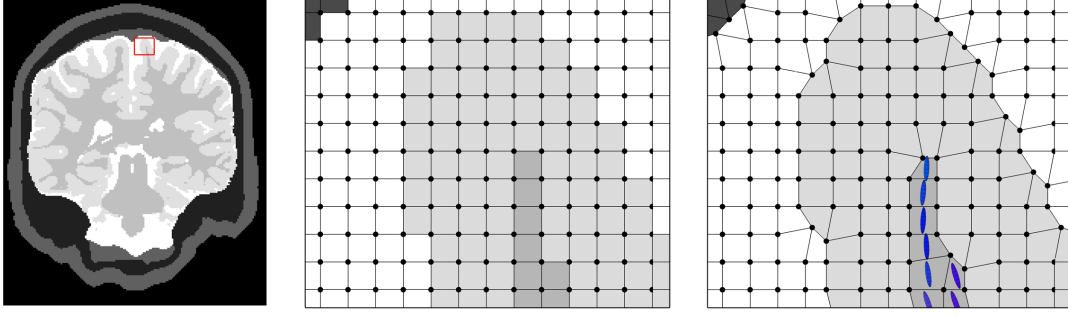


Fig. 3.4.: a) view on a segmented coronar slice, which indicates the positions of the zoomed section used in b) and c). b) shows a cubic grid at this subsection without node shift and c) shows the same subsection using node shift and the assigned conductivity tensor to the white matter elements.

than a factor of 2 for tangential and 1.5 for radial sources independent of the used dipole modeling approach. Thus, all models used in this work are generated using hexahedral elements with node shifting with a node shift factor of 0.49.

The electrical conductivity is finally assigned to the corresponding elements and in case of anisotropic conductivity tensors are used instead of scalar values (cf. Fig. 3.4, right).

3.4.4. Conductivity tensor preparation

Direct approach Using the effective medium approach (cf. 3.3) it is possible to map diffusion tensors to conductivity tensors. Thus, the eigenvalues of the conductivity tensor are calculated using Eq. (3.18), where $k=0.844 \text{ S} \cdot \text{s}/\text{mm}^3$ and $d_e = 0.124 \mu\text{m}^2/\text{ms}$. However, if this approach is applied directly to the diffusion tensor eigenvalues negative conductivities can occur if eigenvalues of the diffusion tensor are below d_e . If we assume that this occurs due to low signal to noise ratio, we can replace such elements by averaging the eigenvalues of the diffusion tensor of the surrounding voxels. The averaging is performed for first, second and third eigenvalue separately. Later in this work we will refer to this approach as direct transformation approach.

Direct approach with volume correction Application of the direct approach would lead to variations of the corresponding isotropic conductivity, which is assumed to correspond to the product of the three eigenvalues. It is known that such variations of conductivity have a strong influence on the forward computation of the magnetic field as well as of the electric potential as shown by Haueisen et al. [131]. In order to handle such variations a normalization has to be applied to the conductivity tensors. Based on the assumption, that the radius of a sphere built by an isotropic tensor corresponds to the scalar conductivity representation within a finite element, one can

3. Volume conductor modeling

apply a normalization which adjusts the eigenvalues of the conductivity tensors, so that the volume of the ellipsoid corresponds to the volume of an isotropic conductivity tensor with given scalar representation σ_{iso} . Thus, the normalization of the eigenvalues σ_{ν_i} is performed by calculating

$$\sigma'_{\nu_i} = \sigma_{\nu_i} \frac{\sigma_{iso}}{\sqrt[3]{\sigma_{\nu_1} \sigma_{\nu_2} \sigma_{\nu_3}}}. \quad (3.22)$$

The ratios between the eigenvalues and the orientation (eigenvectors) of the tensors remain unchanged. In this work we will refer to this as direct transformation approach with volume normalization.

Artificial anisotropy with volume constraint Both the direct transformation approach and an additional volume normalization can lead to large anisotropy ratios in the resulting conductivity tensors. Assuming a measured eigenvalue of the diffusion tensor along a fiber pathway of $2 \mu m^2/ms$ (this eigenvalue corresponds usually to the first eigenvector) and a value of $0.2 \mu m^2/ms$ perpendicular to that path results in a diffusion anisotropy ratio of 10:1. If one applies the direct transformation approach to this numbers, conductivity values of $1.583 S/m$ and $0.061 S/m$ would lead to an anisotropy ratio of 24:1. Higher anisotropy ratios occur if the diffusion tensor eigenvalues approach d_e up to ratios of inf. Furthermore, it is difficult to analyze the effect of anisotropic conductivity if the anisotropy varies over segments of same tissue type (white matter). Therefore, additionally to the approach with and without volume normalization, artificial anisotropies were modeled using only the orientation of the tensors and their corresponding largest eigenvector. For an artificial anisotropy ratio of 10:1 an eigenvalue σ_{\parallel} is assigned to the largest eigenvector which is ten times larger compared to the eigenvalues σ_{\perp} of the shorter eigenvectors. The latter two were set equal. The scaling of the eigenvalues was performed using volume normalization as performed with the direct transformed conductivities. The Eqs. (3.23) and (3.24) show how the longitudinal σ_{\parallel} and transversal σ_{\perp} conductivity tensor eigenvalues are determined from the isotropic conductivity value and the selected factor r (2 if 2:1, 5 if 5:1, and so on). This approach permits the controlled change of anisotropy ratios, whereas the tensor orientation information remains unchanged.

$$\sigma_{\parallel} = \sqrt[3]{\sigma_{iso}^3 r^2} \quad (3.23)$$

$$\sigma_{\perp} = \sqrt[3]{\frac{\sigma_{iso}^3}{r}} \quad (3.24)$$

4. EEG/MEG FEM-Simulations

4.1. Introduction

4.1.1. General approach

EEG and MEG source reconstruction of cerebral activity requires to solve a so-called inverse problem. In case of EEG/MEG the solution of the inverse problem is based on the solution of a corresponding forward problem in which the electric potential and/or magnetic field is calculated for a given source in the brain by using a volume conductor model. Such a source is evoked by electrolytic currents within the dendrites of the large pyramidal cells inducing a current sink under the pial surface and accompanied current sources distant from the sink [132,133]. In neurophysiological and neuropsychological experiments such dipolar source activity can be generated by presenting a defined stimulus to the subject. Typical experiments are the electric stimulation of peripheral nerves (e.g., nervus medianus or tibialis) or the presentation of visual or auditory stimuli. During stimulus presentation the occurring electric potentials and magnetic fields are recorded by electrodes placed on the subjects head and by magnetic field sensors surrounding the head, respectively. As illustrated in Fig. 4.1, solving

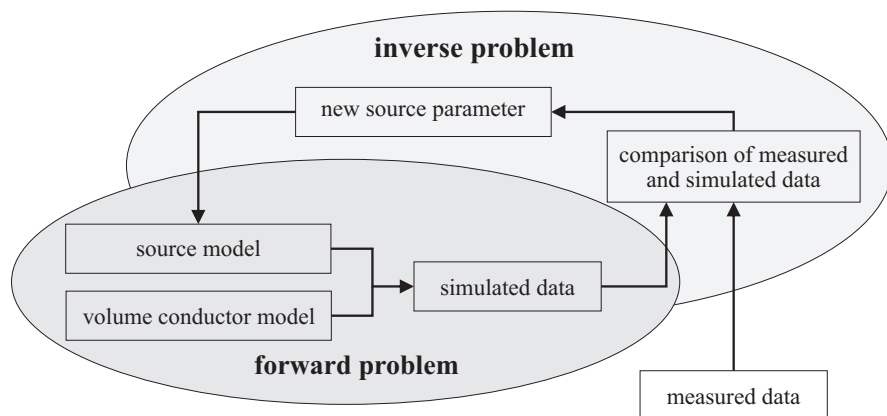


Fig. 4.1.: Schematic illustration of the procedure of solving the inverse problem including the forward problem in EEG/MEG experiments (adapted from Haueisen [29]).

the inverse problem means that the measured data have to be compared to simulated data, which in turn are generated by solving the forward problem, until a solution is found which adequately represents the measured data. The whole, iterative procedure comprises two complex steps: the forward simulation and the optimization process of determining the new source parameters for the next iteration. The former - the forward problem - is based on the quasi-static Maxwell equations (Eq. (3.1)- (3.4)), since the typical primary sources during brain activity have frequencies below 1 kHz, so that the capacitive component of tissue impedance, the inductive effect and the electromagnetic propagation effect can be neglected [134, 135].

4.1.2. The electric forward problem

Since the electric field \vec{E} is irrotational in the quasi-static regime, it is possible to express the electric field as the gradient of a scalar function, called the electrostatic potential ϕ ,

$$\vec{E} = -\nabla\phi \quad (4.1)$$

The current density \vec{J} from Eq. (3.2) is generally divided into two parts, the primary (impressed) \vec{J}_i and secondary (conducting) \vec{J}_c current density [134] given by

$$\vec{J} = \vec{J}_i + \underline{\underline{\sigma}}\vec{E}. \quad (4.2)$$

The primary current density \vec{J}_i is aroused by the expenditure of chemical energy and not by the electric field \vec{E} , since it originates in a source of energy, which is nonelectric in nature [136]. In contrast, the conducting current \vec{J}_c is described by Ohm's law – $\vec{J}_c = \underline{\underline{\sigma}}\vec{E}$. The primary currents \vec{J}_i have to be localized during the inverse problem and to be modeled in the forward problem.

If we now assume that the conductivity distribution $\underline{\underline{\sigma}}$ is given, we can obtain an expression for the potential distribution in the volume conductor by taking the divergence of Eq. (3.2) and using Eq. (4.1) and (4.2)

$$\nabla \cdot (\underline{\underline{\sigma}}\nabla\phi) = \nabla \cdot \vec{J}_i \quad (4.3)$$

In the forward problem, the primary (impressed) current \vec{J}_i and the conductivity distribution $\underline{\underline{\sigma}}$ in the volume conductor Ω are known so that Eq. (4.3) has to be solved for the unknown potential distribution [137].

4.1.3. The magnetic forward problem

Considering the magnetic forward problem, the magnetic potential \mathbf{A} with $\vec{\mathbf{B}} = \nabla \times \mathbf{A}$ is introduced and using Coulomb's gauge $\nabla \cdot \mathbf{A} = 0$, the Maxwell equation (3.2) transforms to [137]

$$\mu_0 \left(\vec{\mathbf{J}}_i - \underline{\underline{\sigma}} \nabla \phi \right) = \nabla \times (\nabla \times \mathbf{A}) = \nabla(\nabla \cdot \mathbf{A}) - \nabla^2 \mathbf{A} = -\nabla^2 \mathbf{A} \quad (4.4)$$

The solution of this Poisson equation is given by [137]

$$\mathbf{A}(\mathbf{x}) = \frac{\mu_0}{4\pi} \int_{\Omega} \frac{\vec{\mathbf{J}}_i(\mathbf{y}) - \underline{\underline{\sigma}}(\mathbf{y}) \nabla \phi(\mathbf{y})}{|\mathbf{x} - \mathbf{y}|} d\mathbf{y} \quad (4.5)$$

If we define F as the area, which is enclosed by the magnetometer coil $\Upsilon = \partial F$, the magnetic flux Ψ through Υ is determined, by [137]

$$\begin{aligned} \Psi = \int_F \mathbf{B} \cdot d\mathbf{f} &= \oint_{\Upsilon} \mathbf{A}(\mathbf{x}) = \oint_{\Upsilon} \frac{\mu_0}{4\pi} \int_{\Omega} \frac{\vec{\mathbf{J}}_i(\mathbf{y})}{|\mathbf{x} - \mathbf{y}|} d\mathbf{y} \cdot d\mathbf{x} \\ &+ \oint_{\Upsilon} \frac{\mu_0}{4\pi} \int_{\Omega} \frac{-\underline{\underline{\sigma}}(\mathbf{y}) \nabla \phi(\mathbf{y})}{|\mathbf{x} - \mathbf{y}|} d\mathbf{y} \cdot d\mathbf{x}. \end{aligned} \quad (4.6)$$

The division of the flux Ψ into two parts is reasonable, since we have two different sources of flux. The primary flux Ψ_p depends on the source model or rather the impressed current $\vec{\mathbf{J}}_i$ and is computed by evaluating an analytic formula [135]. However, the secondary flux Ψ_{sec} , which emerges from the secondary (return) current can only be determined if the potential distribution (Eq. (4.3)) is known.

4.1.4. The lead-field approach

To derive a numerical solution of Eq. (4.3) for the electric problem using FEM, a system of linear equations has to be set up.

$$\mathbf{L}_{ij} \phi_j = \mathbf{b}_i \quad (4.7)$$

Where \mathbf{L}_{ij} represents the stiffness matrix, ϕ_j are the unknown potential values at the nodes of the volume and the vector \mathbf{b}_i on the right-hand side incorporates the source currents $\vec{\mathbf{J}}_i$ and boundary conditions. The elements of \mathbf{L} can be calculated using a Rayleigh-Ritz or Galerkin method [138]. In order to solve Eq. (4.7) for ϕ_j , we have to invert \mathbf{L} . However, calculation of \mathbf{L} and performing the inversion is a very time consuming process. To reduce the computational effort, an element-oriented lead-field matrix (\mathbf{L}) construction method was proposed based on the *principle of reciprocity*

[139]. Since we only need to compute the potential at the electrode positions ϕ_j , we can apply a reduction matrix \mathbf{R} to the inverse of the lead-field matrix \mathbf{L} [139]

$$\phi_r = \mathbf{R}\mathbf{L}^{-1}\mathbf{b}_i \quad (4.8)$$

The reduction matrix \mathbf{R} is a $[K \times M]$ matrix mask (number of nodes by one less than the number of electrodes) which assigns the position of an electrode to a node of the grid. If the true location of the electrode does not correspond precisely to a node of the FE mesh, a weighting matrix instead of a mask has to be used with three or four (depending on the type of elements) non-zeros entries per row that represent the electrodes barycentric weightings for the outer surface triangle or quadrangle that contains the particular electrode position [139]. If we take a mesh containing 100,000 nodes and a EEG electrode setup with 64 channels, only 63 rows of the lead-field matrix have to be build up instead of 100,000, resulting in a speedup of more than 1,500.

This approach was carried out by Wolters et al. [137] to solve the magnetic forward problem and was implemented for both electric and magnetic forward calculations in Neurofem [140], a finite element software for fast computation of the forward solution in EEG/MEG, which is a part of the SIMBIO project [31]. This software package was used for the sensitivity analysis described in this chapter.

4.1.5. The inverse procedure

The inverse problem aims to determine the parameters of the source. Assuming a single dipole, six independent parameters have to be found. Further source types are multi-poles or distributed sources; however, the single dipole is the most simple and most appropriate source model for sensitivity simulation studies.

To determine source parameters is an optimization process, in which a goal function has to be minimized. This goal function is denoted by the difference between measured and simulated data (electric potential or magnetic flux). One method to perform this optimization is the Simplex or Nelder-Mead approach [141]. Assuming a 6 dimensional parameter space, 7 start points are selected and the goal function (e.g. difference of the electrode potentials calculated for dipoles with the selected parameters and the measured data) is determined for the 7 points. A new point is found by reflection, expansion and contraction of the simplex which is controlled by three parameters. A detailed description of the approach in connection with source reconstruction can be found in Haueisen [29]. The problem with the Simplex approach is that it can be stuck in local minima, especially if the initial simplex is chosen too small. However, for the sensitivity analysis this approach is sufficient, since the solution is known and the start parameters can be set close to the expected solution.

4.1.6. Simulations studies

The two following simulation studies described below focus on the influence of white matter anisotropy in an animal and in a human head model. Studies in human models [142, 143, 144] have shown that the electric surface potential as well as the magnetic field are influenced by incorporating anisotropy information in the volume conductor model. However, in these studies only a few dipole positions were investigated. The recent advances in speeding up computation of the forward solution allows for more extensive studies of sensitivity mapping. Additionally, in case of animal studies the possibility of invasive validation is provided, besides the advantage of precise available anatomical knowledge.

4.2. Sensitivity analysis using a rabbit head model

4.2.1. Objectives

As stated before, in source localization studies the anisotropy information is typically neglected when generating volume conductor models. However, in section 3.4, methods were discussed that allow to incorporate anisotropy information into FEM volume conductor models. Especially, the derivation of conductivity tensors from diffusion tensors measured using magnetic resonance diffusion tensor imaging (MR-DTI), is used to generate realistic anisotropic representations of the white matter segment within the brain.

The aim of this simulation study was to quantify the influence of anisotropic white matter tissue conductivity on EEG forward and inverse solutions in the rabbit head. Therefore, three sub-studies were conducted: In the first study (*study I*) the influence of white matter anisotropy determined from MR-DTI on the forward and inverse calculation of focal sources was investigated. For this purpose two different types of volume conductors were used: 1) with isotropic conductivity; 2) with anisotropic conductivity in white matter. For the forward computations the distribution of the electrical potential computed with model 1 and 2 were compared. For the inverse computations model 1 was used with the forward computations from model 2. Since the results obtained in the first study were relatively complex, the effects observed in *study I* were analyzed in more detail in the second study (*study II*). The irregularly shaped white matter compartment of the rabbit was replaced and modeled by an artificial cube of anisotropic conductivity tensors. This cube, due to its regular geometrical structure, allowed to quantify how the mutual interdependencies between dipole positions and orientations, location and orientation of the gray-white matter interface, and the orientation of the anisotropic conductivity influence the forward and inverse solutions. To

test these influences on multiple dipoles, three dipole positions selected from *study II* were chosen and a forward simulation with combinations of these dipoles (*study III*) was performed. The last study provides a validation of the simulations by means of source reconstruction based on measured electrocorticogram (ECoG) data.

4.2.2. Material and methods

MRI Acquisition

T1-weighted, high-resolution as well as diffusion weighted tensor MRI data were acquired at 1.5 T in a White New Zealand rabbit during a single session by using a surface coil (Siemens Magnetom Vision, Siemens Medical Systems, Germany, Erlangen). The T1-weighted data set was obtained by employing a 3D, rf-spoiled FLASH gradient echo sequence with TR/TE 40/11 ms and 204 slices with an isotropic resolution of 0.625 mm^3 . For the diffusion tensor scan an interleaved Turbo-STEAM sequence [64] with TR/TE 15614/68 ms, b-value 500 s/mm^2 , 20 slices, 16 averages with $1\text{ x }1\text{ x }2\text{ mm}^3$ voxels was employed. The diffusion gradients were oriented in six non-collinear directions and one null image (b_0) was acquired in order to normalize for nondiffusion attenuation. The diffusion scan was acquired twice in an interleaved manner to obtain overall 40 slices, which covered the head of the rabbit completely. Since the high-resolution, anatomic scan was run in sagittal orientation and the diffusion scan in coronal orientation, an additional low-resolution 3D, T1-weighted data set with the same location and orientation as the diffusion scan was acquired (TR/TE 600/14 ms, $0.5\text{ x }0.5\text{ mm}^2$ in-plane resolution, 4 mm slice thickness). The high-resolution sagittal data set was then co-registered to the low-resolution coronal data set by employing SPM2 [145].

Model construction

Since an animal model was used, the procedure of generating a segmented volume differs from that introduced in 3.4. The co-registered high-resolution T1 weighted data set was segmented semi-automatically using the Software Curry (Neuroscan, USA). The outermost surface (skin) and the outer brain boundary were determined with a region-growing algorithm. The outer skull boundary was obtained by dilating the outer brain boundary. In order to ensure a closed 3D skull layer a minimum thickness of one discretization step (0.6 mm) was used. The white matter volume was determined by applying a threshold-based, region-growing segmentation starting in a region known to comprised white matter structures. After mesh generation, the FEM model included 662,937 nodes with cubic elements (element length = 0.6 mm). The isotropic conductivities were set to $\sigma=0.33\text{ S/m}$ (skin), $\sigma=0.0042\text{ S/m}$ (skull), $\sigma=0.337\text{ S/m}$ (gray matter), and $\sigma_{iso}=0.14\text{ S/m}$ (white matter) (cf. Table 3.1). For the anisotropic finite element model

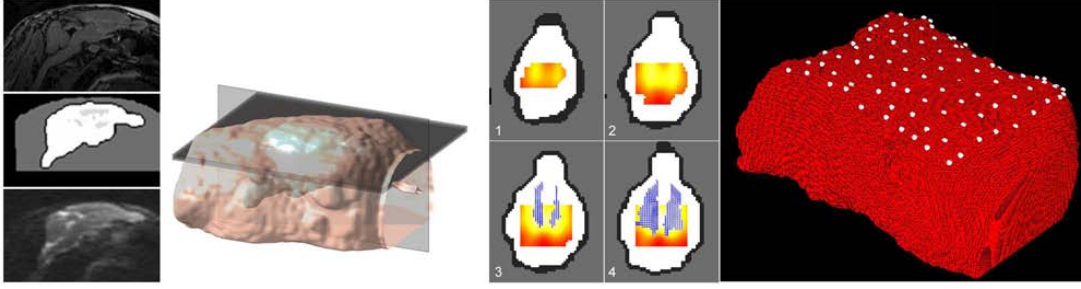


Fig. 4.2.: Overview of the setup for the forward simulation with conductivity tensors. The left column shows sagittal slices of the MRI 3D FLASH scan, the segmentation result including four compartments (skin, bone, gray and white matter), and a diffusion weighted image of the DTI scan. The second column shows a 3D model of the isosurface of the rabbit model which indicates the position of the sagittal slices in column one and the position of the four axial planes in which the dipole source space was located. The third column shows the four numbered (1-4) axial slices in which the dipoles were placed for the simulation. The dipole source space is color coded indicating the distance to the anisotropic tissue (yellow=close; red=distant). The fourth column shows the FEM model of the rabbit including the position of the 100 electrodes.

anisotropic conductivity tensors to all volume elements were assigned belonging to the white matter segment. The eigenvalues of the conductivity tensors were assigned using artificial anisotropy with volume constraint introduced in section 3.4.4 by assuming a ratio of 1:10 and an isotropic conductivity of $\sigma_{iso} = 0.14 \text{ S/m}$.

Electric Measurements

Cortical somatosensory potentials were evoked by electric stimulation of the median and the tibial nerve (0.5 mA constant current square wave pulses, interstimulus interval 500 ms) on a 6 months old White New Zealand rabbit. The rabbit was anaesthetized (Ketamin 24-30 mg/kg per h and Xylazin 2.4-3 mg/kg per h), kept normothermic and was allowed to breathe spontaneously. Small silver stimulation electrodes were placed on the right median and right tibial nerve. After removing the skin and skull bone ECoG (Neuroscan Synamps, USA) was recorded by using a grid of 4 x 4 electrodes over the left hemisphere. The diameter of each single electrode was 0.25 mm and the distance between adjacent electrodes was 1.25 mm. Data were recorded with a sampling rate of 2 kHz, a high pass filter of 0.3 Hz and a low pass filter of 300 Hz. 2048 trials were averaged. The position of the electrodes in relation to the somatosensory cortex was determined. The experiments were approved by the Ethics Committee of the University Clinics Jena, Germany.

Forward Studies

Study I: conductivity tensors derived from DTI The conductivity tensors of the rabbit's white matter, as derived from DTI measurements, were used in the anisotropic model. We calculated the electric potential produced by 1,360 cortically located dipoles (1 mm spacing) for both radial and tangential orientation (with respect to the skull) at 100 electrode positions on the rabbit skin (Fig. 4.2). The positions of the electrodes were arranged in such a way as to cover the dipolar potential distribution for each dipole position and orientation, which occurred in the study. The dipoles were placed only in gray matter with a minimum distance of 1 mm to the skull and white matter. The forward computed data obtained with the isotropic and anisotropic model were analyzed by calculating relative difference measure (*RDM*) values and magnitude difference (*MAG*) values of the electrical potential maps for each single dipole and each orientation. *RDM* and *MAG* were calculated according to Meijs et al. [19] as follows

$$RDM = \sqrt{\sum_{i=1}^n \left(\frac{ref_i}{\sqrt{\sum_{j=1}^n ref_j^2}} - \frac{meas_i}{\sqrt{\sum_{j=1}^n meas_j^2}} \right)^2} \quad (4.9)$$

$$MAG = \sqrt{\frac{\sum_{i=1}^n meas_i^2}{\sum_{i=1}^n ref_i^2}} \quad (4.10)$$

The values obtained with the isotropic model were interpreted as measurement (*meas*) and the values obtained with the anisotropic model were used as reference (*ref*). The indices *j* and *i* represent the number of electrodes used in the setup. *RDM* as well as *MAG* values were then represented as color-coded maps in the dipole source space, where 4 axially cut planes were used (Fig. 4.2). The *MAG* value, which occurs in the forward analysis and the dipole magnitude change (*MC*), which is computed in the inverse analysis, both have numerical values typically around unity, so that values below one indicate a decrease and values above one represent an increase of *MAG* and *MC*. Since the value ranges below and above unity into which *MAG* and *MC* are mapped are different – thus making statistical analysis difficult – an unsigned *MAG_{rel}* in the forward analysis and an unsigned relative magnitude change (*MC_{rel}*) in the inverse analysis are introduced. These latter quantities were calculated according to Eqs. (4.9) and (4.10), respectively.

$$MAG_{rel} = \left| 1 - \sqrt{\frac{\sum_{i=1}^n meas_i^2}{\sum_{i=1}^n ref_i^2}} \right| \quad (4.11)$$

$$MC = \left| \frac{magnitudo_{original} - magnitudo_{inverse}}{magnitudo_{original}} \right| \quad (4.12)$$

Study II: artificial anisotropic cube In order to obtain more specific information about the influence of anisotropic conductivity the experimentally derived conductivity tensors were replaced by an artificial cubic volume (dimension $12 \times 12 \times 12 \text{ mm}^3$) of anisotropic conductivity in the brain (Fig. 4.3). The anisotropy ratio in the cube was set to a ratio of 10:1:1 (long=0.65 S/m and trans=0.065 S/m) in left-right orientation. A total of 4104 single dipoles were placed around this cube in 3 layers. For each dipole location all three independent orientations (with respect to the orientation of the anisotropy within the artificial cube) were considered (cf. Fig. 4.3), i.e., dipoles were oriented in anterior-posterior (AP), left-right (LR) and inferior-superior (IS) direction. The electrical potential was computed at the same 100 electrodes as in *study I* and the forward computed data were compared analogously. The *RDM* and *MAG* values are represented as color-coded maps in the dipole source space above and below the cube (Fig. 4.6).

Study III: multiple dipoles The investigation of the influence of anisotropic conductivity to the forward solution in EEG using multiple dipoles leads to a vast number of possible spatial as well as directional dipole arrangements. Therefore, the particular source position from the dipoles of the AP, LR and IS data sets used in *study II* and showing the largest *RDM* were selected. The maximum *RDM* for the AP oriented dipoles was found on the right hand side of the block, for the LR oriented dipoles below the block and for the IS oriented dipoles also at the right hand side of the block. The distance between the two AP and IS oriented dipoles was 1.3 mm, their distances to the LR dipole were 8.05 and 7.42 mm, respectively. The forward simulation was performed with the combination of two dipoles (AP+LR, AP+IS, LR+IS) and all three dipoles (AP+LR+IS).

Source localization from simulations

To examine the influence of white matter anisotropy on source localization, the forward computed electric potential data, which were obtained from the anisotropic model for 4,104 single dipoles separately, were used and a single dipole was reconstructed from each simulated distribution of the electric potential using the isotropic model. The Sim-

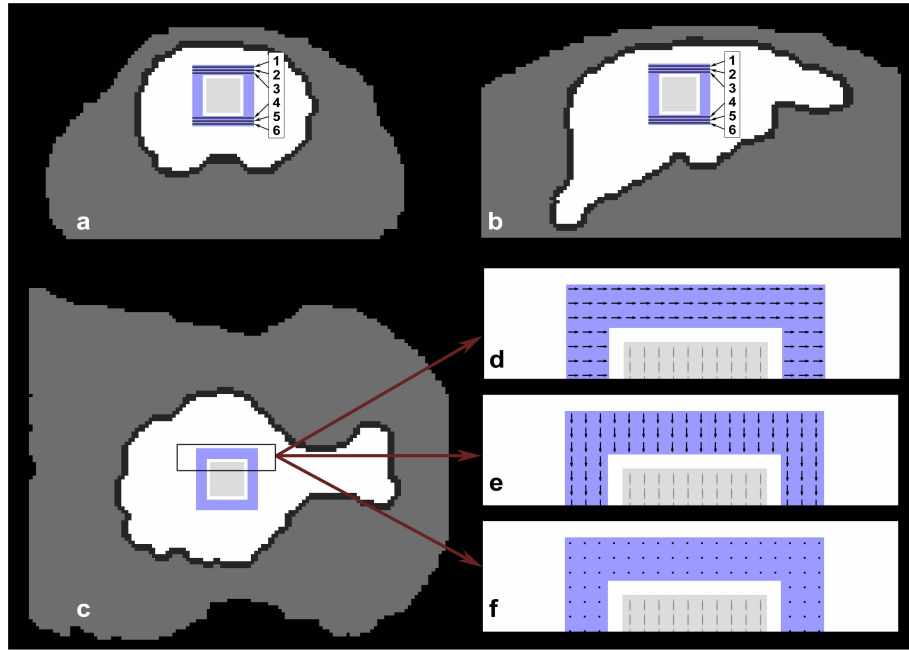


Fig. 4.3.: Schematic view of the positioning of the artificial anisotropic cube (light gray) employing the segmented rabbit model. Subfigures (a-c) show a coronal, sagittal and axial slice, respectively. In (a-b) the positions of the planes which were used for demonstration of the results (number 1-6) are shown. Subfigures (d-e) show a zoomed view of the axial slice in subfigure c and demonstrate the positioning and orientation of the dipoles as well as the conductivity tensors in the anisotropic cube used for the forward analysis - d) dipoles in anterior-posterior (AP) direction - e) dipoles in left-right (LR) direction - f) dipoles in inferior-superior (IS) direction. The full dipole source space is indicated by blue color.

plex algorithm (section 4.1.5) was applied to solve the non-linear optimization problem. The initial Simplex point for source localization was placed at an average distance of 1 mm from the position of the original dipole (thus mimicking a jitter on the dipole position), that had been used to compute the forward solution. Such an initial point should minimize the possibility for the algorithm to get stuck in local minima. The resulting dipole positions, orientations, and strengths were compared to the corresponding original dipole parameters and the changes (dipole shift, orientation change, and magnitude change) were visualized as color-coded maps in the dipole source space, similar to the comparison of the forward solutions described above. Source localization was performed separately for *studies I* and *II*.

Source localization from measurements

Based on the 16 channel ECoG measurements the dipolar source was reconstructed which evoked the potential map at the peak of the first cortical answer (P1, see Fig. 4.4)

following stimulation of both the median or tibial nerve. Since the electrodes were placed directly on the cortex, only the representation of gray and white matter for source localization with the isotropic and anisotropic FEM model (consisting of 40,902 elements) was used. Additionally, a crosscheck of the localization results with a Boundary Element Method (BEM) model comprising only the outer surface of the brain (one compartment model) with 4,000 elements was performed. The BEM grid was generated using Curry (Compumedics, Neuroscan, El Paso, USA) and the inverse solution was determined with the Simbio Toolbox [31,140]. Optimization was again performed using the Simplex algorithm.

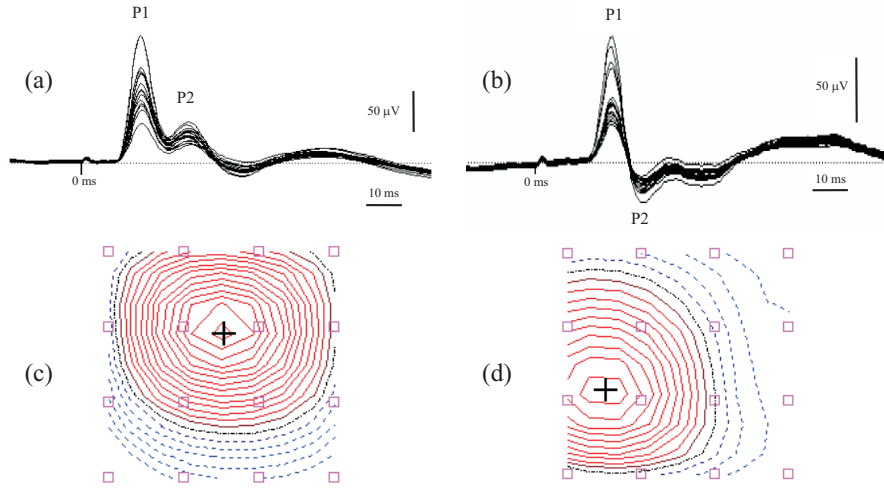


Fig. 4.4.: ECoG recordings: (a) signals of serveral trials measured at a single channel during medianus stimulation, (b) the same for tibialis stimulation, (c) surface potential map by means of isopotential lines measured at P1 for the medianus stimulation, (d) the same for the tibialis stimulation.

Statistics

To derive the mean and the variance of the distributions of the calculated quantities (RDM , MAG_{rel} , dipole shift, magnitude change (MC_{rel}), orientation change) a Rayleigh distribution was assumed since it fits to the derived distributions. The Rayleigh distribution is a special case of the Weibull distribution [146] and their probability density function is defined by:

$$f(x, b) = \frac{x}{b^2} e^{\frac{-x^2}{2b^2}} \quad (4.13)$$

For interpretation of the data the parameter b in Eq. (4.13) was fitted by finding its

maximum likelihood:

$$b = \sqrt{\frac{1}{2n} \sum_{i=1}^n x_i^2} \quad (4.14)$$

The mean and the variance were calculated according to:

$$m = b \sqrt{\frac{\pi}{2}} \quad (4.15)$$

$$v = \frac{4 - \pi}{2} b^2 \quad (4.16)$$

4.2.3. Results

Forward simulations

Study I: conductivity tensors derived from DTI Figure 4.5 summarizes the results of the *RDM* and *MAG* mapping, which was obtained from the comparison of the forward computation for the isotropic and anisotropic rabbit head model. As can be seen the histograms clearly show non-Gaussian distributions. The mean values for *RDM* and *MAG_{rel}* in case of radial dipoles are $1.046 \pm 0.003 \cdot 10^{-2}$ and $0.733 \pm 0.002 \cdot 10^{-2}$, respectively and in case of tangential dipoles $5.68 \pm 0.09 \cdot 10^{-2}$ and $4.06 \pm 0.05 \cdot 10^{-2}$. It is also clear from Fig. 4.5 that with smaller distance of the dipoles to the white matter, the *RDM* and *MAG* values are more deviating. The largest *RDM* and *MAG* values are found between anisotropic segments (cut plane 1 in the dipole source space). In general the *MAG/RDM* values were larger for tangential dipoles in comparison to radially oriented dipoles. This indicates that the electric potential distribution of tangential dipoles is more influenced by anisotropy than the one of radial dipoles.

Study II: artificial anisotropic cube Figure 4.6 displays the *RDM/MAG* values of six transverse slices above (1-3) and below (4-6) the artificial anisotropic cube (cf. Fig. 4.3). The *RDM* between the potential maps calculated with and without anisotropy was less than 0.02. The maximum *RDM* value for the AP, LR and IS oriented dipoles were 0.0099, 0.0073 and 0.019, respectively. The positions of these dipoles were used as source positions for the multiple dipole test in *study III*. The *RDM* values are very low with respect to the theoretical maximum of 2, where 2 means the compared signals are equal but of opposite sign. The values for *MAG* range from 0.94 to 1.04. Despite this relatively weak influence of the anisotropy, Fig. 4.6 nevertheless clearly demonstrates that the quantities depend on the distance between the source and the anisotropic tissue. Furthermore, the dipoles located below the anisotropic cube were more influenced than the dipoles above the cube. On the *RDM* maps the strongest influence is seen close to

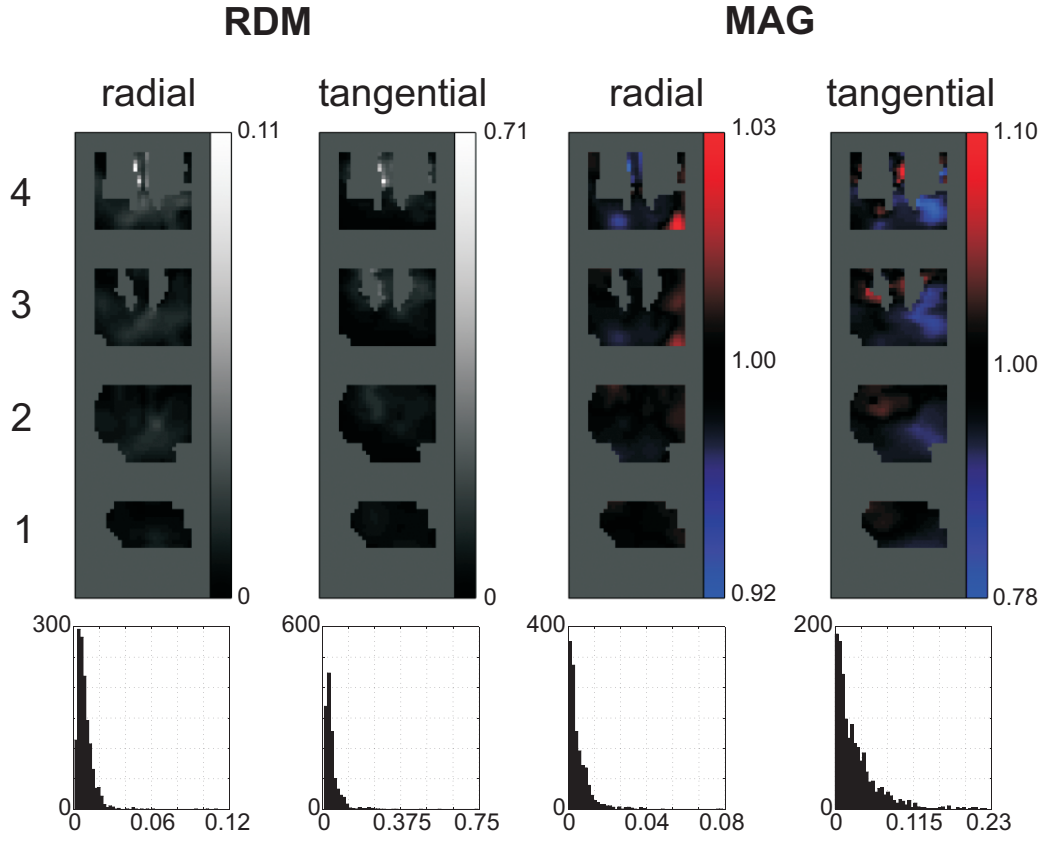


Fig. 4.5.: Mapping of the RDM and MAG values obtained in *study I* in the dipole source space for the radial and tangential dipoles. Note, that the color maps of the MAG values are not equidistant for values below and above one. Below the maps, the corresponding histograms are given, where the MAG analysis shows the relative MAG value according to (4.11).

the corners of the anisotropic cube for the two orthogonally oriented dipoles. The *MAG* maps show that the strongest influence of anisotropy is to be expected mainly central to areas of anisotropic tissue. It is also quite interesting to note that the *MAG* and *RDM* values appear to be spatially decoupled: with high *RDM* values the corresponding *MAG* values are high or low and vice versa. Again, the histograms in Fig. 4.6 show a non-Gaussian distribution.

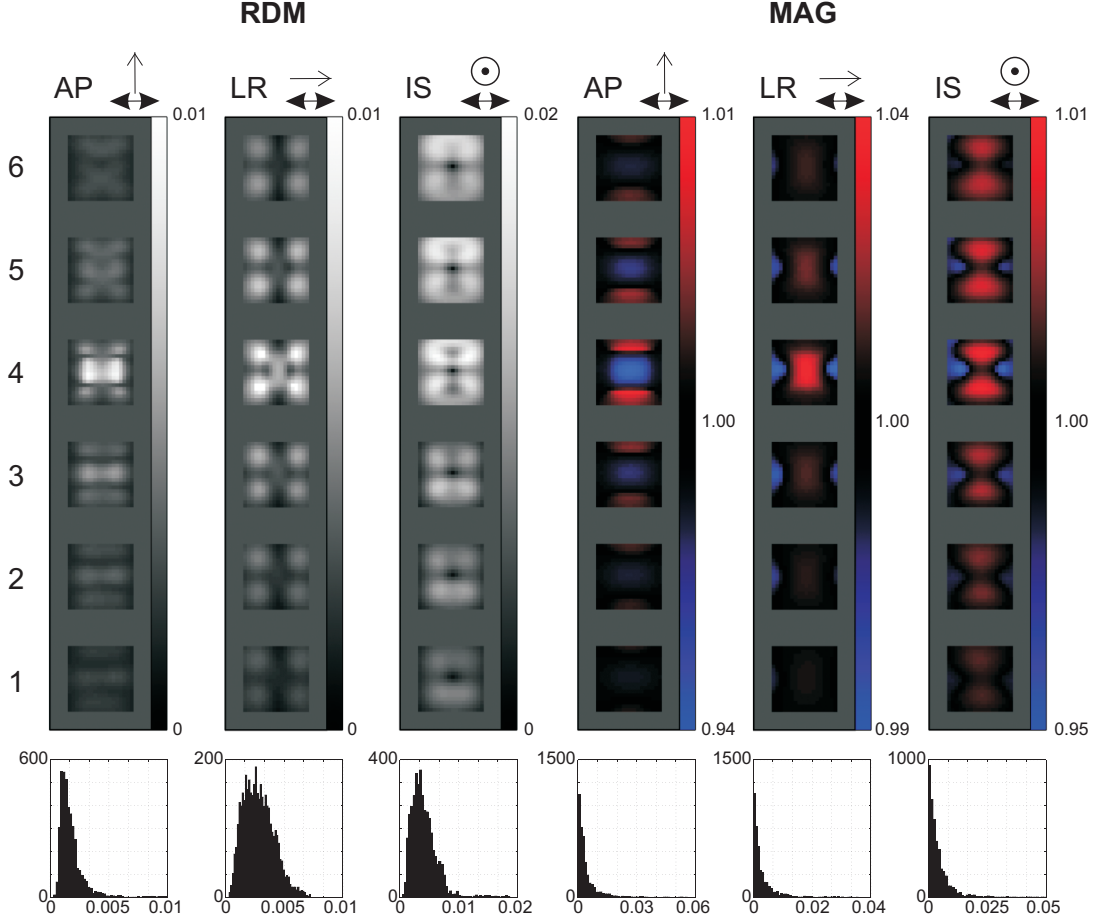


Fig. 4.6.: Mapping of the *RDM* and *MAG* values obtained in *study II* (anisotropic cube) in the dipole source space for dipoles in AP (anterior-posterior), LR (left-right) and IS (inferior-superior) direction. The arrows above the maps indicate the orientation of the dipoles and the main direction of the anisotropy. Note, that the scale of the color map of the *MAG* values is not equidistant for values below and above one. The histograms of the *MAG* analysis show the relative *MAG* value according to (4.11).

Study III: multiple dipoles For the combination of multiple dipoles the obtained values were: *RDM* and a *MAG* of 0.0356 and 1.001 for the AP+LR pair, 0.0137 and

0.970 for the AP+IS pair and 0.0215 and 1.0121 for the combination LR+IS. Using all three dipoles simultaneously as sources a RDM of 0.0449 and a MAG value of 0.993 was derived. Except for the AP+LR combination all RDM values are higher than the values obtained for a single dipole. The MAG values did not exceed the limits found in *study II*.

Source localization from simulations

Study I: conductivity tensors derived from DTI All dipoles were shifted in their location and changed their orientation due to the different volume conductor models, which were used for the forward and inverse solution. Shifts up to 0.84 mm and 1.26 mm were obtained for radial and tangential dipoles, respectively, with a mean value of 0.26 mm (radial: 0.24 mm; tangential: 0.28 mm). The mean deviation of the dipole's orientation was 10.32° (radial: 13.75° ; tangential: 4.92°) and the mean absolute magnitude change of the dipole was 28.8% (radial: 21.0%; tangential: 34.9%). In Fig. 4.7, the dipole shift and the changes in dipole magnitude and orientation are mapped onto the segmented slices of the rabbit's brain (see Fig. 4.2). Similar to the results of the forward solution (Fig. 4.5), the changes due to anisotropy are largest close to the anisotropic white matter.

Study II: artificial anisotropic cube The forward computed electric potential data obtained from the dipoles in the model with the artificial anisotropic cube were used to perform source localization with the model containing the isotropic cube. Figure 4.8 shows the resulting dipole shifts, dipole magnitude and orientation changes in six transverse slices above and below the cube (cf. Fig. 4.3). These maps clearly demonstrate an influence of anisotropy for the lower planes (4-6), similar to the forward computation (Fig. 4.6). For the upper planes the effect is less pronounced. For the dipole shift we obtained values up to 2.64 mm. However, in general the mean dipole shift was found to be very small. The influence on the orientation change was found to be significant at the edge of the anisotropic cube in case of dipoles oriented in AP and LR direction and centered below the cube in case of a IS dipole orientation.

Influence of distance

To investigate the influence of the distance between the dipoles and the anisotropic structure the results for AP, LR and IS dipoles were merged and grouped by their distance to the anisotropy. The mean and variance for RDM , MAG_{rel} , dipole shift, relative magnitude change and orientation change were computed according to Eqs. (4.15) and (4.16) and are displayed in Fig. 4.9. In addition, the upper (1-3) and lower (4-6)

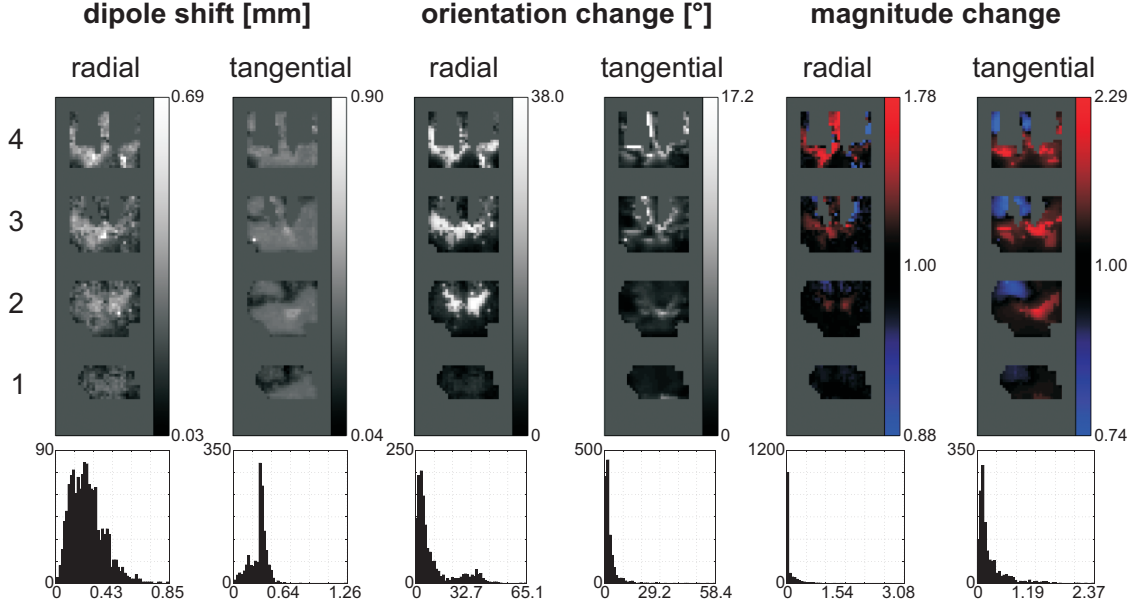


Fig. 4.7.: Mapping of the shift, orientation and magnitude change and corresponding histograms of the inverse calculation in *study I* in the dipole source space for the radial and tangential dipoles. The dipole shift is given in mm and the orientation change in degree. Note, that the scale of the colormap of the values for magnitude change is not equidistant for values below and above one. The histograms of the magnitude change analysis show the relative magnitude change value according to (4.11).

planes were considered separately. Fig. 4.9 clearly demonstrates that all values of all investigated quantities decrease with increasing distance. The values for MAG_{rel} and relative magnitude change show stronger decreases (more than linear) with distance as compared to RDM , dipole shift and orientation change. Furthermore, it is seen that in all cases the values in the planes below (4-6) the anisotropic cube are influenced more than the values in the planes above (1-3), which is also visible in Figs. 4.6 and 4.8.

Influence of original dipole orientation

Figure 4.10 displays the same data as Fig. 4.9, but this time grouped with respect to the three original dipole orientations (Fig. 4.3). Again the planes above and below the cube are considered separately. The results depicted in Fig. 4.10 are heterogeneous. There seems to be no prevailing configuration of dipole orientation versus anisotropy orientation producing larger or smaller errors than any other. Intuitively, it was expected that positions below the anisotropy are influenced most strongly. However, in almost half of the cases ($RDM(AP)$, $MAG(IS)$, dipole shift(AP), rel. magnitude change(AP, IS), orientation change(AP, LR)) the mean value of all dipoles was found to

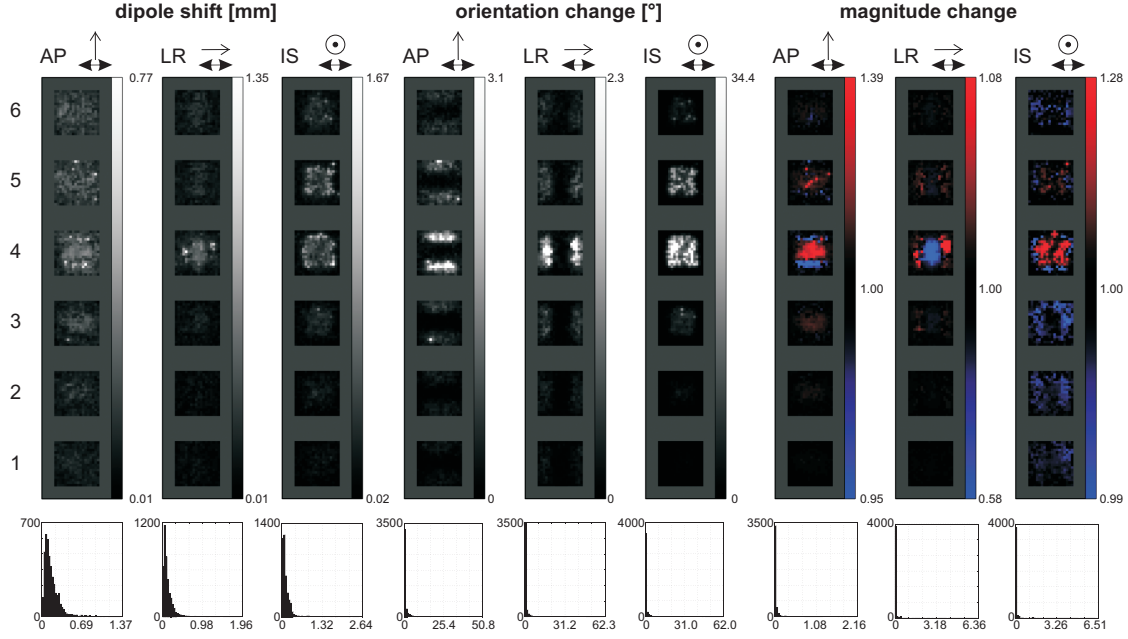


Fig. 4.8.: Mapping of the analysis and corresponding histograms of the inverse calculation in *study II* in the dipole source space for the radial and tangential dipoles. The dipole shift is given in mm and the orientation change in degree. Note, that the color map of the values for magnitude change is not equidistant for values below and above one. The histograms of the magnitude change analysis show the relative magnitude change value according to (4.11).

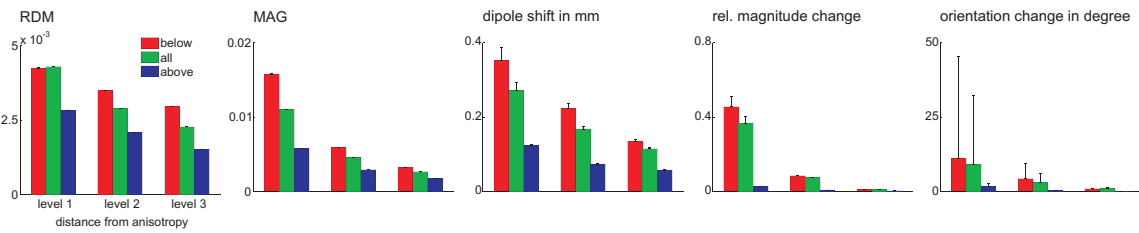


Fig. 4.9.: Analysis of the influence of the distance on RDM , MAG , dipole shift, relative magnitude change and orientation change for results of *study II*. The diagrams show the mean value with variance obtained by assuming a Rayleigh distribution. Note that the variances for RDM and MAG are too small to be visible. Level 1-3 indicates the different layers with respect to the anisotropic cube. The results are given for all (green), the upper (blue) levels 1, 2, 3 and lower (red) levels 4, 5, 6.

be higher than for the dipoles in the planes below the cube.

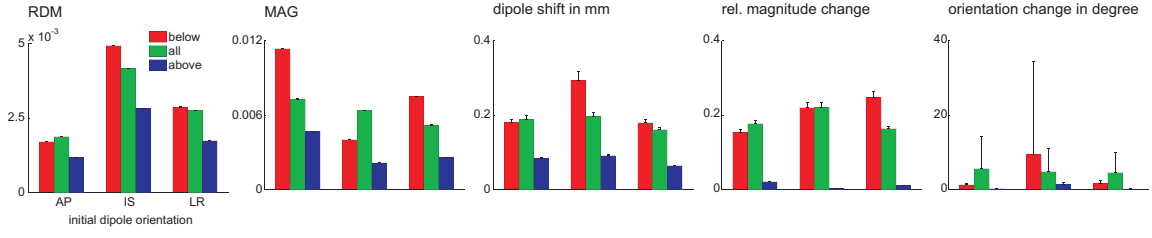


Fig. 4.10.: Analysis of the influence of the original dipole orientation on RDM , MAG , dipole shift, relative magnitude change and orientation change for results of *study II*. The diagrams show the mean value with variance obtained by assuming a Rayleigh distribution. Note that the variances for RDM and MAG are too small to be visible. AP (anterior-posterior), LR (left-right) and IS (inferior-superior) indicate the different original dipole orientation according to Fig. 4.3. The results are given for all (green), the upper (blue) and lower (red) levels.

Regions of strong influence

Figure 4.11 shows a qualitative analysis of the above results, which was realized by employing 3D models. From the upper 20 percent of the distribution of each calculated quantity, an isosurface was generated and visualized together with the anisotropic cube. Table 4.1 lists the corresponding threshold values to the 0.8 percentile used in Fig. 4.11. The strongest influence of anisotropy on RDM was found above the edges of the cube for dipoles in AP and LR orientation, which differs from the result for the IS orientation. The MAG_{rel} values are most strongly influenced if the dipole is oriented parallel to the surface of the anisotropic cube. Very similar results were obtained for the relative magnitude change. Thus, the MAG values of the forward computations predict quite well the results of the dipole magnitude changes in the inverse computations. On the contrary, the correlation between dipole shift and RDM was found to be rather low, indicating that RDM is not well predicting the dipole shifts. One reason for this might be due to the rather small values obtained for the dipole shift. The change of orientation was influenced most strongly for dipoles oriented perpendicular to the surface of the anisotropic cube.

Source localization from measurements

Source localization was performed for the time instant of the first peak in the ECoG signal (Fig. 4.4), which is known to be generated in the somatosensory cortex S1. The latency of this peak after median nerve stimulation was 17.5 ms and 22 ms for the tibial nerve. The electric potential pattern was monopolar. In all inverse solutions

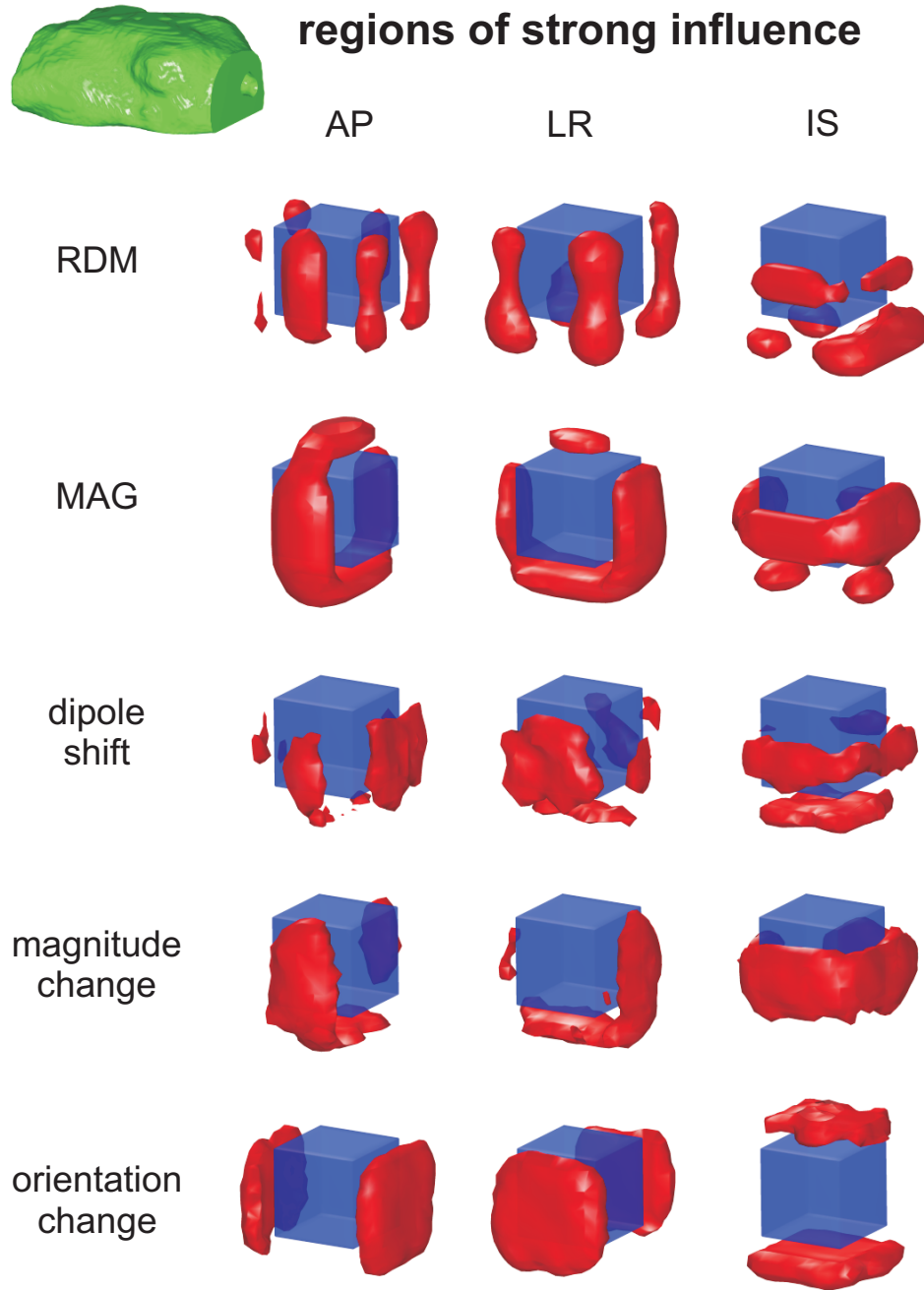
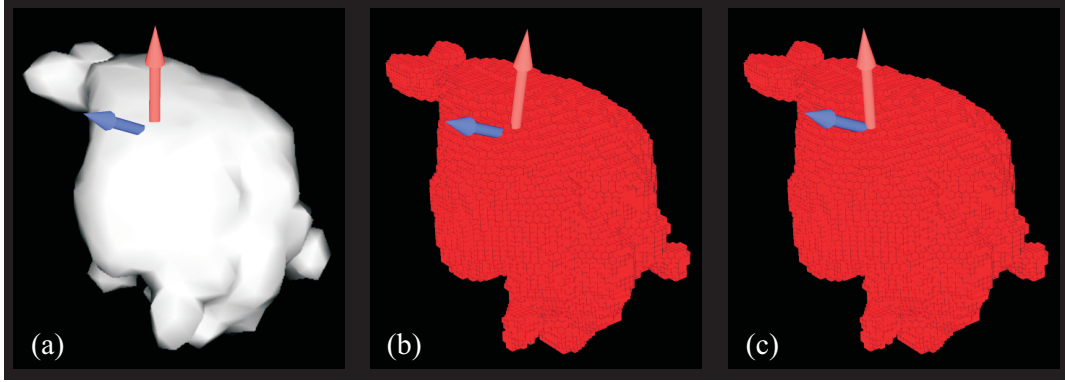


Fig. 4.11.: Visualization of regions of strong influence when neglecting the anisotropy information in *study II*. The matrix of 3D models shows the anisotropic cube in transparent blue, and regions of values above the 0.8 percentile for *RDM*, *MAG*, dipole shift, magnitude change and orientation change are visualized by red surfaces. The isosurface model of the rabbit head in the upper left corner indicates the orientation of 3D models.

Tab. 4.1.: Threshold values corresponding to the 0.8 percentile used in Fig. 4.11

	AP	LR	IS
RDM	0.0022	0.0039	0.0055
MAG_{rel}	0.0063	0.0047	0.0064
dipole shift in mm	0.24	0.19	0.20
relative magnitude change	0.035	0.023	0.035
orientation change in degree	1.04	0.82	0.68

**Fig. 4.12.:** Results of the source localization from measurements: (a) localization of the source for the tibialis (blue dipoles) and for the medianus (red dipole) stimulation using the BEM model, (b) the same using the isotropic FEM model, and (c) using the anisotropic FEM model.

(BEM, FEM isotropic, FEM anisotropic) the dipoles were found with slight differences in orientation and magnitude (Fig. 4.12). The spatial distance in dipole localization for both nerves averages to 2.0 mm (2.00 mm for the BEM, 1.89 mm for the isotropic FEM and 2.12 mm for the anisotropic FEM). This distance matches the expected anatomical distance between the two source positions of 2 mm. Moreover, the localized sources were within an accuracy of 1 mm in the expected cortical areas derived from anatomy. The dipole location difference between these BEM and isotropic FEM models was 0.42 mm for the tibial nerve and 0.51 mm for the median nerve stimulation. The dipole location difference between the results obtained with the anisotropic and the isotropic FEM model was 0.76 mm for the median nerve and 0.17 mm for the tibial nerve stimulation.

4.2.4. Discussion

In this animal study, the influence of anisotropic conductivity on the forward and inverse computation in EEG experiments was investigated by applying a high-resolution finite element method (FEM) model of a rabbit head. Although FEM models permit the inclusion of anisotropy, this information has been rarely used so far in EEG source

localization due to the calculation and memory expenses. Nowadays, the availability of affordable high-performance computing equipment and the recent development of fast and efficient solvers allow extensive studies in an acceptable time.

Strong influence of the anisotropy was found on the magnitude in the forward as well as in the inverse solution and on the orientation of dipoles in the inverse solution. On average, dipole shifts due to the anisotropy were within the limits of the procedural accuracy of EEG source localization. However, about two percent of the dipoles exhibited localization errors significantly higher than the procedural limit. The low localization errors and the relatively high magnitude changes are in good agreement with the results of Haueisen et al. [142]. Furthermore, anisotropy in the innermost layer of a four layer spherical volume conductor had a strong effect on the magnitude of the electric potential produced by a tangential dipole, but only a weak effect on the topology [36]. However, the presented results reflect only the influence of neglecting anisotropy information in the used model. There are further modeling errors which can lead to significant changes of the forward as well as inverse solution. Slight changes of the tissue conductivity next to the source, would affect the results significantly [76, 147] as would a neglect of parts of the model as shown by He et al. [148]. These modeling errors would superimpose the effect of neglecting anisotropy.

In contrast to the low *RDM* values for single dipoles found in *study II*, a tested setup of multiple dipoles (*study III*) showed significantly higher *RDM* values (up to 4 times). However, it was also found that *RDM* could be lower compared to a single dipole (based on the values obtained for the three dipoles in *study II*). Since the investigation of multiple dipoles can lead to a vast number of combinations, a general conclusion from this limited test cannot be drawn. Nevertheless, it shows that neglecting an anisotropic conductivity can strongly extend the error in the forward solution of multiple dipoles.

A clear result of *studies I* and *II* was that all investigated measures (*RDM*, *MAG*, shift, magnitude and orientation change) were more strongly influenced the closer the dipoles were placed to the anisotropy. Consequently, a stronger influence on all quantities is expected if the dipoles would be located inside the anisotropic tissue. *RDM* and dipole shift seem to be more linearly dependent on the distance between dipole and anisotropy, whereas, *MAG*, magnitude and orientation change seem to be non-linearly correlated to the distance.

One further result of *study II* was that all investigated measures were influenced stronger in planes below the cube than in planes above. This is in principal agreement with Anwender et al. [149] and Wolters et al. [144, 150]. Despite the three exceptions visible (see Fig. 4.11), the result measures seem to be less affected when the dipoles are positioned above the anisotropic cube. Such a setting is actually the most common for animal studies, like rabbit or rat, because of their lissencephalic brain. Also, in

the human brain such a geometrical situation is common for the crown of a gyrus. As presented in Figs. 4.10 and 4.11 of *study II*, the relation between the orientation of the dipole and the orientation of the anisotropy seems to have little influence on the estimated dipole orientation and magnitude when neglecting anisotropy. In other words, the influence of anisotropy seems not to be dependent on the direction of the dipole orientation relative to the anisotropy orientation, but on the dipole direction relative to the cube as such. If the dipoles point perpendicular to the cube the influence is less than if they are oriented parallel to the cube. Since the orientation of the dipole was strongly influenced by the anisotropy in the inverse computation, we would expect a correlation between orientation of the dipole and orientation of the anisotropy. However, the results reflect that the anisotropic block as such has more influence on the reconstructed orientation than the relation between the orientation of the dipole and the orientation of the anisotropy. As an experimental confirmation for this observation we can consider at least in part the results by Liehr and Hauelsen [151]. They investigated a variety of dipole orientations relative to anisotropy orientations by using magnetic measurements in a physical phantom and found that for dipoles both at 0° and 90° the orientation error was minimal. The corresponding magnitude changes, however, are not directly comparable to the results since their dipolar source was located within the anisotropic material. Nevertheless, the tendency that a 0° setup (here: LR) has lower MAG values and relative magnitude change values is also seen in our data (Table 4.1). A setup with dipoles within the anisotropic material cannot be modeled with our current software and will be investigated in future studies.

Figure 4.11 indicates a negative correlation between the magnitude and orientation change (strong changes in orientation correlate with weak changes in magnitude and vice versa). This is, however, true only for the largest 20 percent of the values presented in this figure. For smaller values, there is a positive correlation between both result measures, also independent of the orientation of the dipoles.

The distribution (relative occurrence) of the result measures was found to be clearly non-Gaussian, whereas a Rayleigh distribution fitted the data well. Visually similar distributions were observed in a simulation study with a spherical head model including anisotropy [152].

In the localization study with values taken from real measurements (SEP after stimulation of median and tibial nerve, DTI derived conductivity data of the rabbit white matter) we employed three different volume conductor models (BEM, isotropic and anisotropic FEM). We found comparable results with all three models: the localization was in agreement with the anatomical expectation and the distance between the two dipoles (median and tibial nerve) was also as anatomically expected. These results both verify the modeling approach itself and are consistent with the above discussed

relatively small influence found in the simulations of dipoles located above a white matter tract. The distance between our simulated dipole layers and the anisotropic cube (*study II*) represents a typical anatomical distance for the rabbit brain [153].

Finally, it is concluded that source localization procedures in animals will improve when including white matter anisotropy information. This holds for dipole orientation and magnitude estimations more than for dipole localizations. The influence of anisotropy on source estimation however, was found to be complex. Therefore, direct transfer of the results to other species (including humans) has to be considered with caution.

4.3. Sensitivity analysis using a human head model

4.3.1. Objectives

The interesting results in the animal study could not be directly transferred to human studies, since the object (rabbit head) is very small compared to the human head and the distribution of possible dipole positions is limited due to the simpler structure of the rodents brain. Nevertheless, despite these limitations one would expect similar effects when neglecting anisotropy information within the volume conductor of a human brain.

The human study was performed using high resolution finite element head models. These models comprise different anisotropic representations of the white matter tissue segment (see section 3.4.4). Using these models the influence of anisotropic white matter on the EEG and MEG forward as well as inverse solution was investigated for almost all possible dipole positions in the cortical ribbon (the gray matter segment between the pial and the white matter surface). This allows to map the different error measures (similar to the mapping in section 4.2.3) onto the cortical surface and to identify anatomical regions which are highly affected. Similar to the animal study (section 4.2), the human study is also divided into a forward analysis part, which however examines both EEG and MEG. In the forward analysis the question is, how the magnetic field or electric potential generated by a dipolar source is affected if the white matter segment is modeled anisotropic, in the inverse analysis the question is, what happens if a magnetic field or electric potential was measured from a anisotropic model, but reconstructed using an isotropic model.

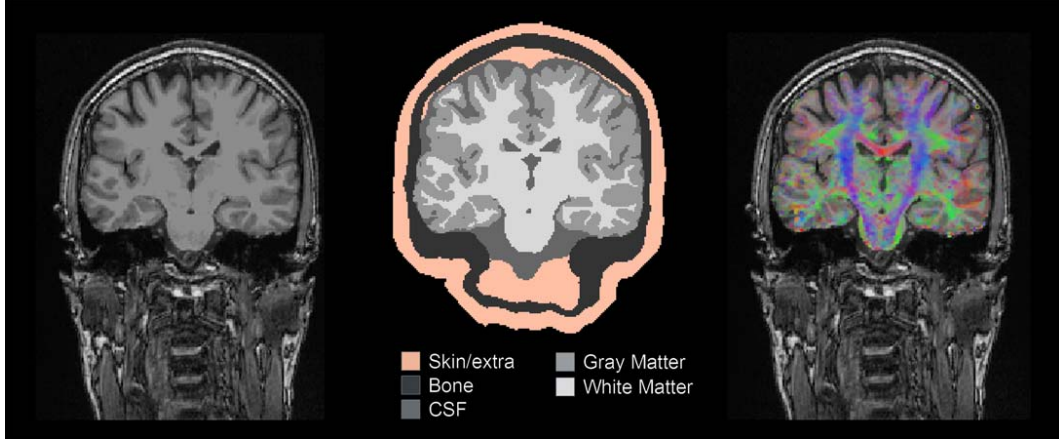


Fig. 4.13.: From left to right: coronal section of the T1-weighted data set; same slice after segmentation into five different tissue types, diffusion tensor data visualized by color-coded representation of the first principal component (largest eigenvector), registered and overlaid on the T1-weighted slice.

4.3.2. Material and Methods

Generation of the anisotropic FEM models

In order to generate the high resolution FEM models high resolution isotropic T1 and T2 weighted images (1 mm^3 , $\text{FOV}=256\text{ mm}$) were acquired. Diffusion tensor data were acquired using a TSRE-EPI sequence with a resolution of 2 mm^3 , 30 different diffusion directions and a b-value of 1000 s/mm^2 . Calculation of the diffusion tensors was performed with b-matrices, which comprise the contributions of the imaging gradients and cross terms (see 2.3.1). All MR measurements were performed using a 3T MRI scanner (Tim Trio, Siemens Medical, Erlangen, Germany). Following the procedure outlined in 3 the segmented volume was set up with 5 different tissue types (skin/extra, CSF, white and gray matter, bone) (cf. Fig. 4.13 left and middle image). The tensor data were transformed to the T1 data as described before (section 3.4.2). Intermediate results of this process are shown in Fig. 4.13. Based on the segmented data a FE mesh was generated using cubic elements and a node shift of 0.49 (see section 3.4.3). The FE model consists of 3.2×10^6 cubic elements with an element size of approximately 1 mm^3 .

Different conductivity tensor generation methods (see section 3.4.4) led to 7 different FEM models. One model was generated with isotropic tensors in white matter elements and four models were set up with artificial anisotropy ratios of 1:2, 1:5, 1:10 and 1:100, taking only the orientation of the diffusion tensors into account. The conductivity tensors of the two other models were set up using the *direct* approach and the direct approach with volume constraint (*directv*), respectively (section 3.4.4). The conductivity values σ_{\parallel} and σ_{\perp} , which were determined using the different approaches

Tab. 4.2.: Longitudinal σ_{\parallel} and transversal σ_{\perp} conductivities in S/m of the white matter tensor elements which were set for the 7 different models. For the models generated using the direct approach and the direct approach using volume constraint the mean and (minima/maxima) are given. σ_{iso} in S/m denotes the scalar equivalent of the tensors, which is equal for all models except the *direct*. *aniso ratio* shows the ratio of the first to the second and third eigenvalue of the conductivity tensors, which is predefined for the artificial anisotropies and equal for the *direct* and *directv* approach.

	1:1	1:2	1:5	1:10	1:100	<i>direct</i>	<i>directv</i>
σ_{\parallel}	0.14	0.222	0.409	0.650	3.016	0.915 (0.048/3.535)	0.2791 (0.14/241.6)
σ_{\perp}	0.14	0.111	0.082	0.065	0.030	0.439 (0.81e-5/3.096)	0.113 (0.2e-3/2.961)
σ_{iso}	0.14	0.14	0.14	0.14	0.14	0.531 (7.52e-4/2.981)	0.14
<i>aniso ratio</i>	1	2	5	10	100	3.152 (1.0/7.168e4)	3.152 (1.0/7.168e4)

are listed in Table 4.2. Since the anisotropy ratio for the *direct* and *directv* model vary within the white matter segment, the fourth line lists the minimal, maximal and the mean occurring anisotropy. A detailed view of the model comprising anisotropic conductivity within the white matter segment with an artificial anisotropy ratio of 1:5 is shown in Fig. 4.14.

EEG and MEG sensor setup

To obtain good coverage of the surface potential, 130 electrodes were placed on the superior part of the FE model. The positions were chosen as follows: a surface of the head was generated and the Nasion (root of the nose) and Inion (the most prominent projection of the occipital bone at the lower rear part of the skull) position were selected interactively. The number of triangles of the surface (comprising the whole head) was reduced to 500 while preserving the shape of the surface using MATLAB (R2007a, The Mathworks, Natick, MA, USA). A virtual transverse plane tilted coronally in such a way that the Inion and the Nasion were in this plane was defined to divide the surface in the superior and a inferior part. The vertices of the surface, built from the reduced patches on the superior part, were selected as dipole positions. The selected positions are shown as black dots on the model surface in Fig. 4.15, together with the MEG sensors.

The MEG sensors were set up using the sensor positions of a 306-channel whole head MEG system (Elekta AB, Stockholm, Sweden) installed in the Biomagnetic Center of the clinic of Neurology in Jena. This system comprises 306 channels and incorporates

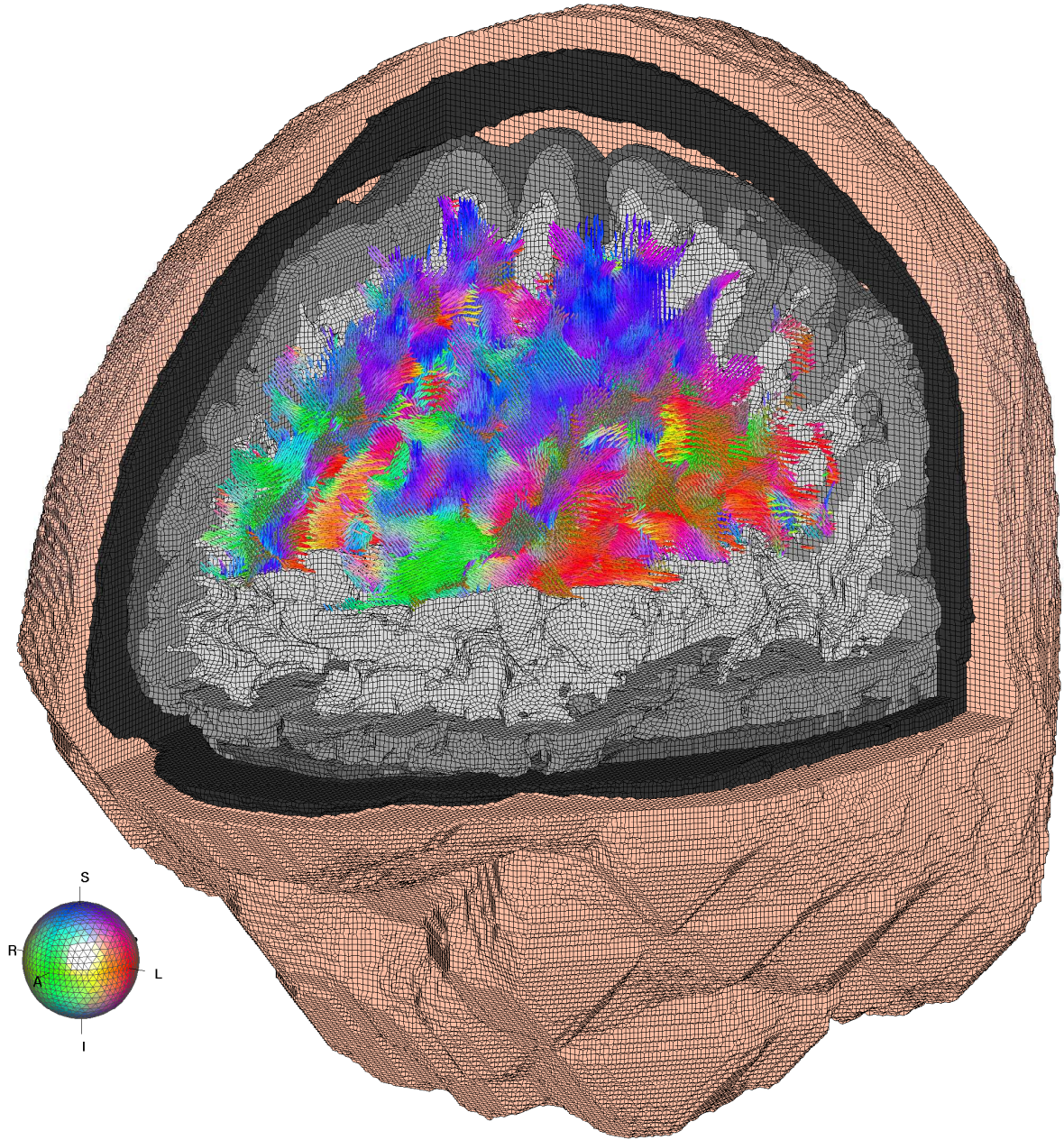


Fig. 4.14.: High resolution FE volume conductor model which was used for the forward and inverse study. The cropped section allows an insight into the model with the conductivity tensors in the white matter FE elements. The tensors have an artificial anisotropy of 1:5 and the color codes the principal direction (largest eigenvector) of the tensors (green: anterior-posterior, red: left-right, blue: inferior-superior). This plot was generated using Matlab (R2007b, The Mathworks, Nattick, MA, USA).

unique vector sensors, that comprise two orthogonal planar gradiometer and one magnetometer each, in 102 positions within a helmet system. These 102 sensor positions were used for the simulation. A pickup and a reference coil with counter windings were placed in each of these positions having a normal, which equals the magnetometers from the whole head system (typically perpendicular to the subjects head).

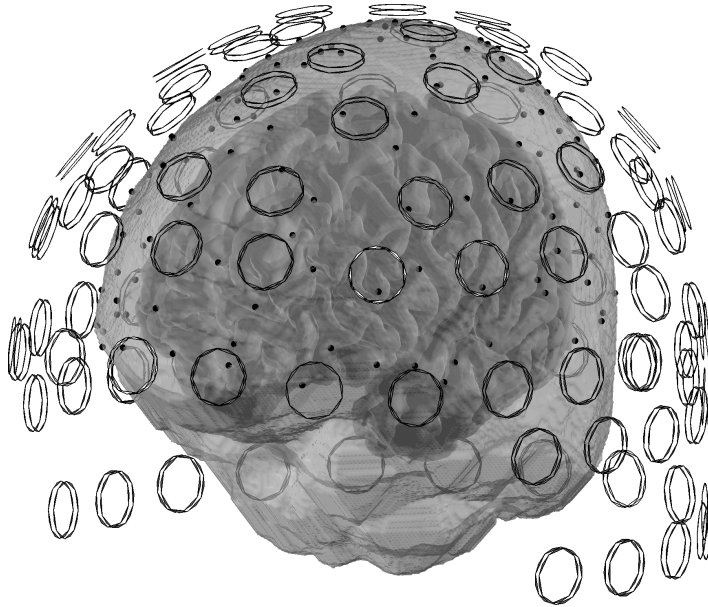


Fig. 4.15: FEM model of a human head with setup of the electrodes (black dots) and the magnetic field sensors (modeled as two loops – pickup and reference – with opposite winding).

Forward studies

For the forward studies over 25,000 dipoles were placed in the cortical ribbon of the head volume. The cortical ribbon corresponds to the outer gray matter segment and is enclosed between the pial surface and the surface of the white matter segment. Since dipolar sources are assumed to originate from the pyramidal cells, which are perpendicular to the pial surface and thus also perpendicular to the white matter surface, the orientation of the dipoles was defined as follows: from the segmented data set white matter was extracted as a binary mask. Subsequent smoothing with a 3D Gaussian kernel (3x3) was applied to generate a gradient and smooth the aliasing of the binary mask. The intensity gradient, which surrounds the mask after smoothing was used to determine a normal vector with respect to white matter. The position of the dipoles was then determined by shifting the white matter vertices by 2 mm in the direction of the corresponding normal vector. For most positions this would lead to dipole positions in CSF, since the cortical thickness is only 2.5 mm on average [117]; however, the cortical gray matter segment was artificially dilated by shrinking the white matter volume as described in section 3.4.1, so that a broader cortical ribbon band was available. The orientation of the dipoles was determined by selecting the normal of the white matter

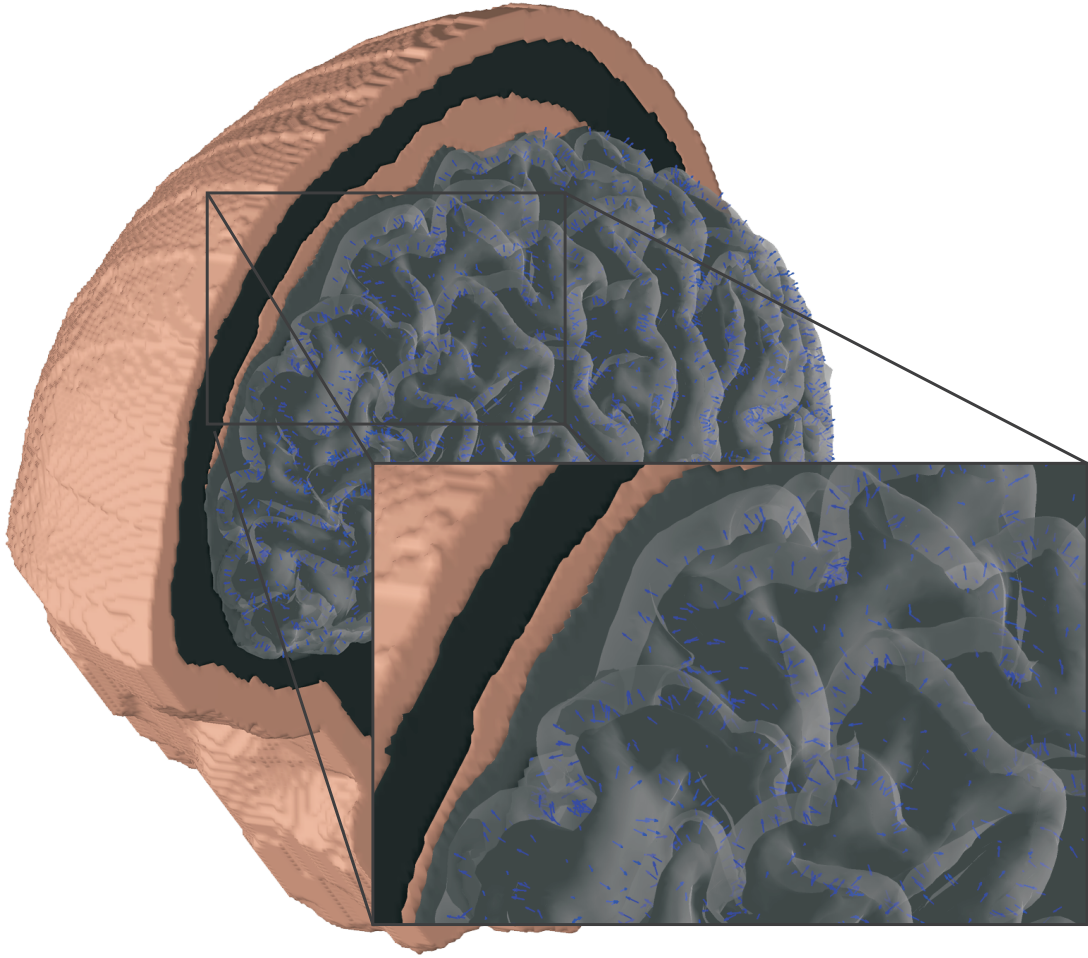


Fig. 4.16.: Insight into the FEM model with gray and white matter surfaces delineating the cortical ribbon. The close up view demonstrates the orientation of the dipoles with respect to the cortical ribbon.

surface that is closest to the point found by shifting the vertices. This must not always be the vertex from which the dipole position originates. Subsequently, the number of dipoles was reduced, so that the distance to the next dipole position was about 2 mm. The positions and orientations of the dipoles with respect to the FE model are shown graphically in Fig. 4.16. For each of the selected dipoles the MEG and EEG forward solution was determined for all seven FEM models separately using the sensor setup described above. To determine the influence of neglecting anisotropic white matter tissue, the forward solutions derived with the anisotropic models were compared to the data derived with the isotropic model by means of RDM and MAG (Eqs. (4.9) and (4.10)).

Inverse study

The influence of neglecting anisotropy with the inverse problem was investigated by employing the forward solution, which was derived using the anisotropic models, as *measured* data for the source localization procedure using the isotropic model. The estimated dipolar sources were then compared to the corresponding initial dipoles which were used for the forward simulation by means of dipole shift (localization error), change in dipole orientation and change in dipole magnitude.

Mapping of the measures

For visual inspection all quantities (*RDM*, *MAG*, dipole shift length, dipole orientation change, dipole magnitude change) were mapped on the inflated white matter surface of the head model to obtain a qualitative impression of the cortical areas, where the EEG and MEG forward as well as inverse solutions are strongly affected by anisotropy. Since the number of vertices of the white matter surface was much higher, 162,012 vertices *vs.* 12,770 dipole positions for the right hemisphere and 159,514 surface vertices *vs.* 13,152 dipole positions for the left hemisphere, the closest dipole position for each surface vertex was determined. If the distance between a vertex and the next dipole was found to be smaller than 7 mm, the corresponding value (*RDM*, *MAG*, dipole shift length, dipole orientation change, dipole magnitude change) was assigned to the vertex (similar to nearest neighbor interpolation). Subsequent smoothing was applied to linearly interpolate the transitions between the vertex groups with different dipole positions as sources and thus different measures.

4.3.3. Results

Forward simulations

RDM and MAG values were computed according to Eqs. 4.9 and 4.10 using the fields and potentials derived with the anisotropic models as *measurement* data and the data from the isotropic model as *reference* data, and density function plots were created (Fig. 4.17). To establish the density plots, the edge defining vector for the RDM plots was set from 0 to 1 with a step size of 0.0075 and from 0.3 to 1.4 with a step size of 0.0075. Similar to the results in the animal study non-Gaussian distributions were observed for RDM and MAG, which made it difficult to define classic statistical moments like mean or variance. Thus, in order to quantify the differences of the data derived with the different anisotropic models and modalities, the 5th, 50th and 95th percentile of the distributions were determined and listed in Table 4.3. The 50th percentile equals the median. The 5th and the 95th percentile can be interpreted as upper and lower

bounds of the distribution in case of RDM. However, for MAG they represent the upper bounds for increasing as well as decreasing magnitude changes. Both the diagrams (blue lines in Fig. 4.17) as well as the values in the table, clearly show that MAG values decreased whereas RDM values increased with higher anisotropy in the white matter segment.

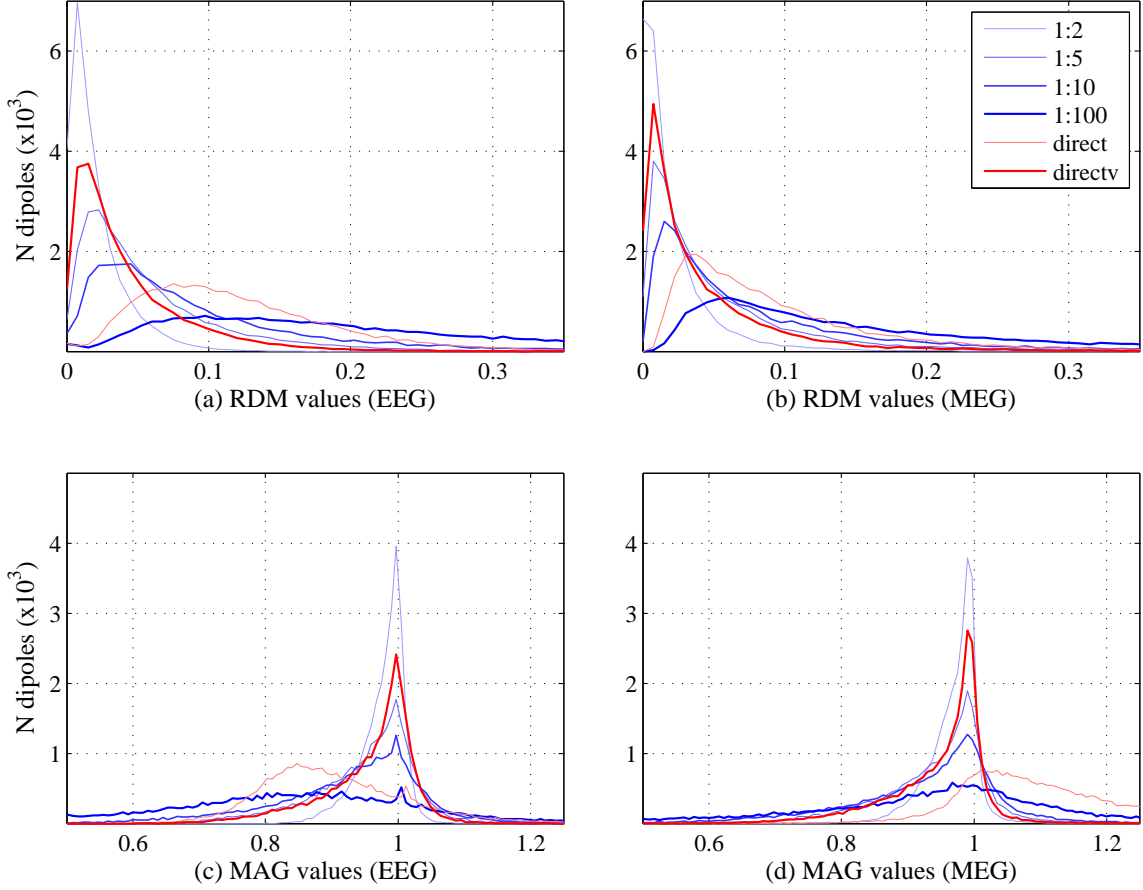


Fig. 4.17.: Density functions for the measures RDM and MAG derived in the forward study for EEG and MEG.

RDM and MAG obtained with the model using *direct* transformed conductivities (light red line in Fig. 4.17) exhibit distributions which are between the graphs corresponding to the models with anisotropy of 10:1 and 100:1. However, the model with volume corrected direct (*directv*) transformed conductivities shows a density distribution which is between the data from model 2:1 and 5:1. This holds true for MEG as well as EEG as can be seen in Fig. 4.17 and Table 4.3. Comparison of the data for MEG and EEG shows that RDM and MAG are similar for the models with artificial anisotropies. Especially the MAG values are almost identical for both modalities. With respect to RDM the median values (50th percentile) are lower for MEG, whereas the

Tab. 4.3.: RDM and MAG values of the 5th, 50th and 95th percentile from the density distributions for the different anisotropic models

measure	modality	1:2	1:5	1:10	1:100	direct	directv
RDM	EEG	0.004	0.011	0.016	0.050	0.038	0.008
		0.018	0.045	0.071	0.191	0.112	0.033
		0.064	0.170	0.265	0.643	0.255	0.130
	MEG	0.003	0.008	0.012	0.037	0.025	0.006
		0.015	0.037	0.056	0.141	0.078	0.028
		0.079	0.206	0.320	0.761	0.287	0.156
MAG	EEG	0.916	0.797	0.707	0.460	0.756	0.816
		0.989	0.971	0.952	0.850	0.893	0.982
		1.021	1.051	1.077	1.191	1.110	1.040
	MEG	0.903	0.782	0.700	0.545	0.940	0.801
		0.982	0.965	0.958	0.968	1.093	0.974
		1.015	1.048	1.090	1.362	1.427	1.027

95th percentiles in turn are higher. Also of note is that the distributions of MAG for the *direct* model are very different between EEG and MEG. Usually, one would expect that the magnitude of the field is lower ($MAG < 1$) with the anisotropic model, however, for the *direct* model and MEG most dipoles generate a stronger field.

Logarithmized MAG values To investigate the MAG distribution in more detail an additional measure was introduced: $\log(MAG)$. The $\log(MAG)$ has two key features, which facilitates an easier interpretation: (1) positive values correspond to increased magnitudes, negative values represent decreased magnitudes, (2) the amounts of positive and negative $\log(MAG)$ values are equal, so that a value of -0.693 equals a decreased magnitude of $1/2$ and a value of 0.693 equals an increased magnitude by a factor of 2. In addition to calculating the logarithm of the MAG values, their distribution was plotted as a cumulative distribution function (CDF) (Fig. 4.18). Horizontal lines in the plots denote the 5th, 50th and 95th percentile and the vertical line divides the data into positive and negative values. The value at which the graphs intersect the vertical line are listed in Tab. 4.4 in percent. From the values in Table 4.4 one can see that the number of dipoles generating lower magnitudes in the anisotropic models increases for EEG, but decreases for MEG with increasing anisotropy.

Result maps For visual inspection of the results the values for each dipole position were mapped on the inflated surface of the hemispheres as proposed in section 4.3.2. The patterns which were obtained similar for the right and left hemisphere. Therefore, only the right hemisphere is shown in the following figures. Furthermore, only results derived with the model comprising anisotropic white matter with a ratio of 10:1 were

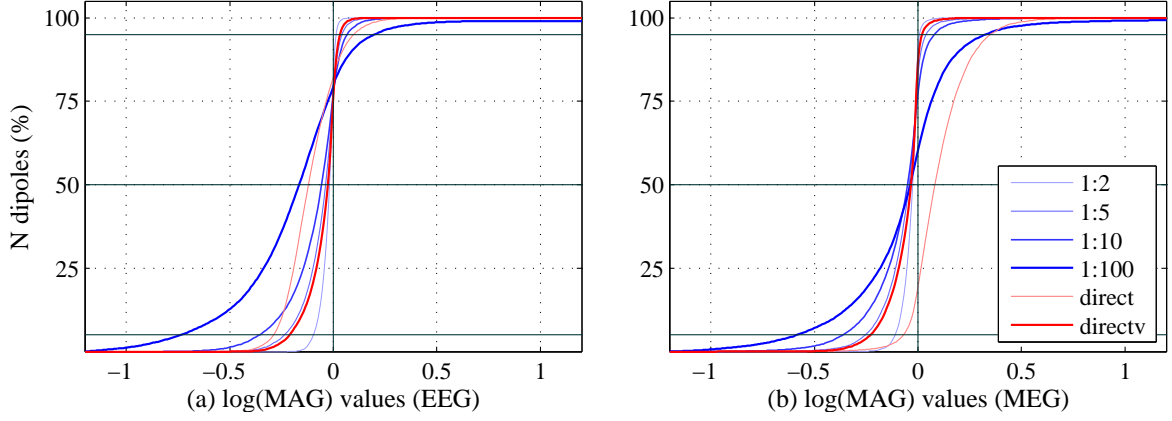


Fig. 4.18.: Cumulative distribution functions for the logarithmized MAG values derived in the forward study for EEG and MEG. The horizontal lines represent the 5th, 50th and 95th percentile level and the vertical line divides the data in positive and negative values. The value at which the graphs intersect the vertical line are shown in Tab. 4.4.

Tab. 4.4.: 5th, 50th and 95th percentile of the logarithmized MAG values for the different models. The fourth line within each modality shows the amount of dipoles in percent which generate a lower magnitude in the anisotropic models compared to the solution in the isotropic model.

measure	modality	1:2	1:5	1:10	1:100	direct	directv
log(MAG)	EEG	-0.088	-0.227	-0.347	-0.777	-0.280	-0.204
		-0.011	-0.030	-0.049	-0.163	-0.113	-0.019
		0.021	0.049	0.074	0.175	0.105	0.040
		68.2%	71.2%	73.0%	78.9%	80.7%	67.9%
	MEG	-0.103	-0.246	-0.356	-0.608	-0.062	-0.222
		-0.018	-0.035	-0.043	-0.032	0.089	-0.026
		0.014	0.047	0.086	0.309	0.355	0.027
		81.0%	76.8%	73.0%	58.8%	16.7%	78.3%

chosen for display. Transformation of the measures RDM and $\log(\text{MAG})$ to surface maps was performed using Matlab (R2007a, The Mathworks, Nattick, MA, USA) and *tksurfer* from the Freesurfer software package was used for visualization.

Comparing the lateral views of Fig. 4.19 and 4.20, the overlay patterns look very similar. Focusing on the binarized curvature pattern, which delineate sulci and gyri areas, areas representing sulci appear to be more affected than the gyri areas. Surprisingly, for both modalities we observed not only decrease magnitudes in the sulci for the $\log(\text{MAG})$ maps, but also positions where the dipoles generate increased magnitudes, thus, it is not possible to postulate that sulci areas correlate with a decreased magnitude only, however, with highly affected areas in general.

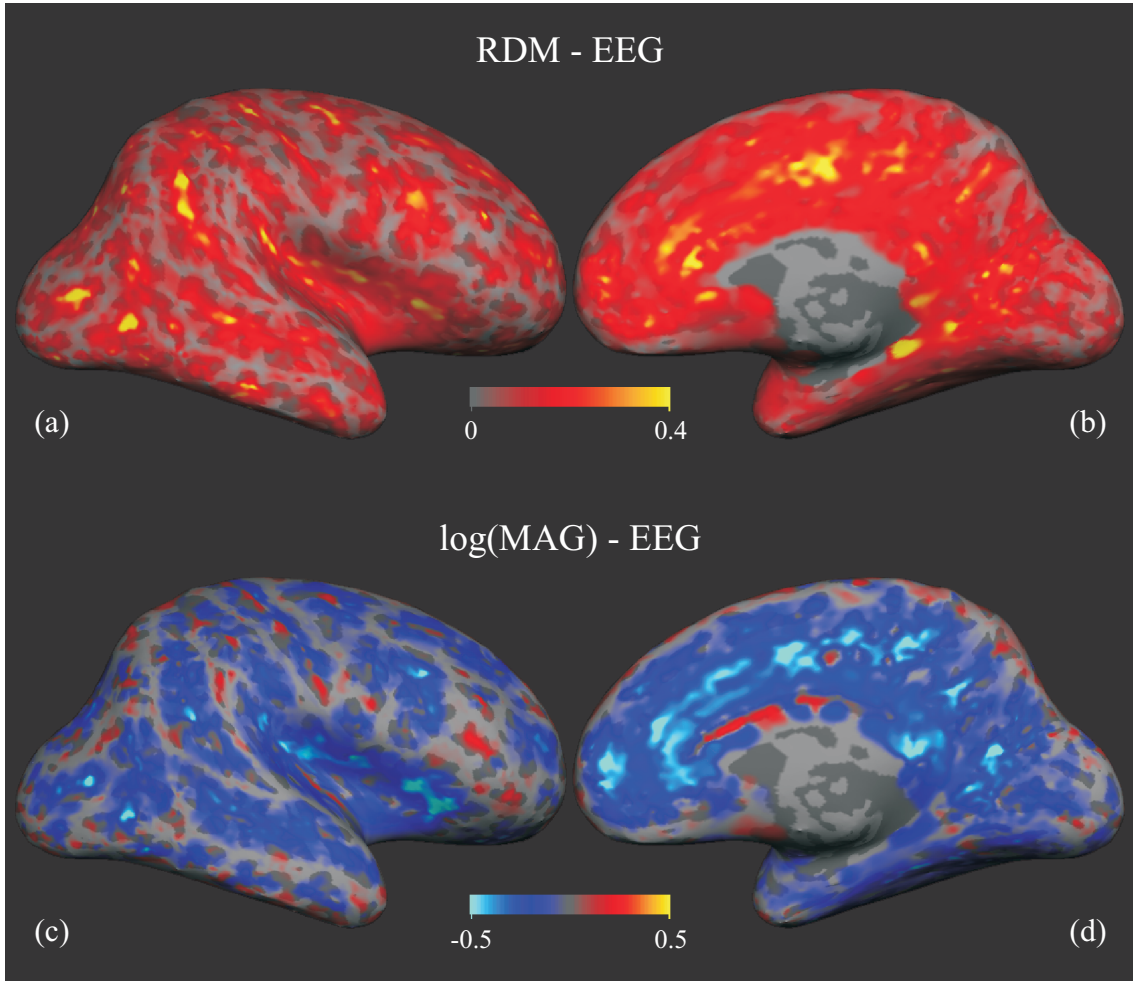


Fig. 4.19.: EEG-Results: Mapping of RDM (a,b) and $\log(\text{MAG})$ (c,d) on the inflated white matter surface of the right hemisphere. The left column (a,c) shows the lateral views and the right column (b,d) shows the medial views. The gray pattern on the surface delineates sulci (dark gray) from gyri (light gray) areas.

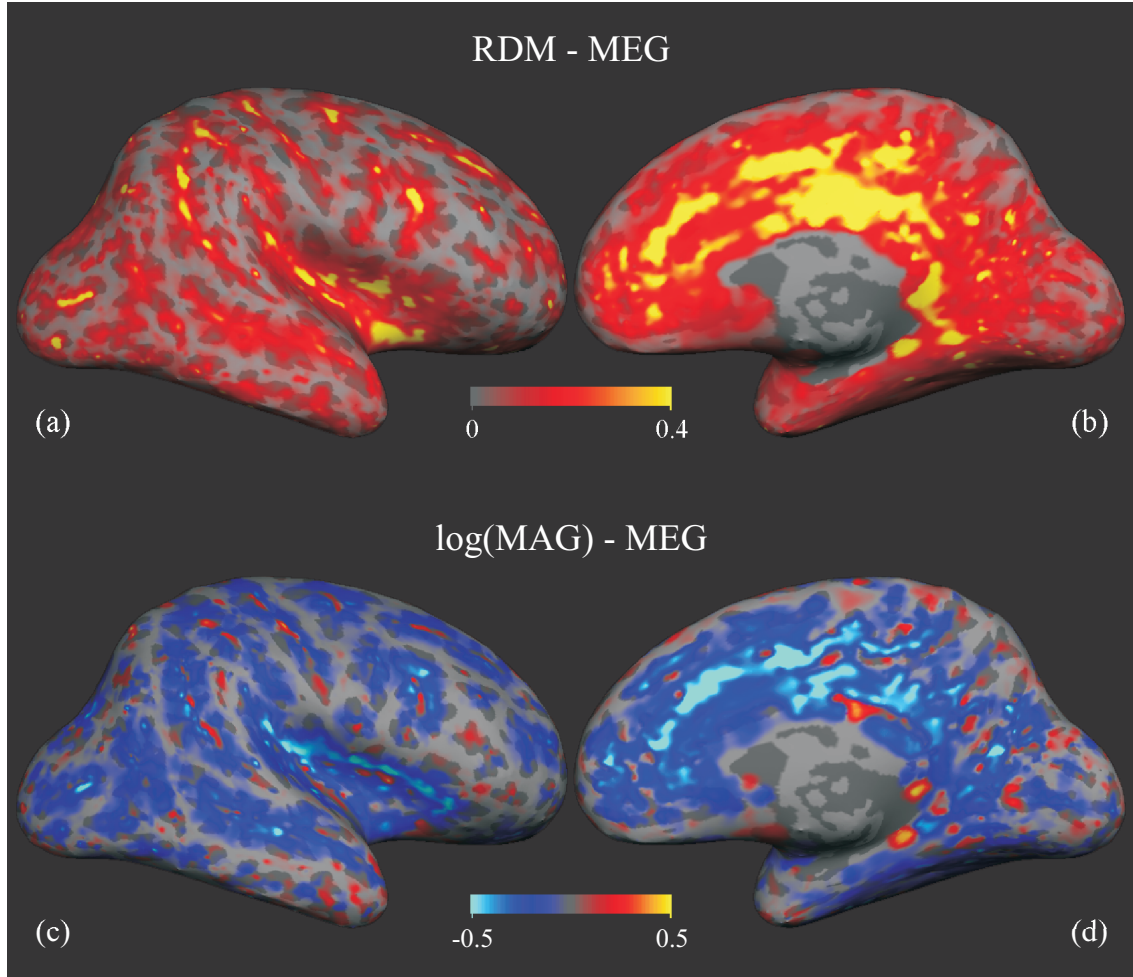


Fig. 4.20.: MEG-Results: Mapping of RDM (a,b) and log(MAG) (c,d) onto the inflated white matter surface of the right hemisphere. The left column (a,c) shows the lateral views and the right column (b,d) the medial views. The gray pattern on the surface delineates sulci (dark gray) from gyri (light gray) areas.

From the RDM mapping one can see that the pattern for MEG appears *sharper* in comparison to EEG. This confirms the findings shown in Table 4.4. In general, the MEG modality is less affected, but the extreme values are higher. For the lateral region the areas, which are affected most by anisotropic conductivity within the white matter segment, are the lateral sulcus, the superior temporal sulcus, the postcentral sulcus and the transverse occipital sulcus. Positions in the precentral and central sulcus, which are interesting for motor functions, are also affected.

The medial parts of the cortex – in particular the cingulate, the parietooccipital and the calcarine sulcus – are more affected than lateral regions (Fig. 4.19(b,d) and Fig. 4.20(b,d)). Comparing MEG and EEG for the medial parts one can see, that with MEG these parts are more affected than with EEG. Although not that prominent as for the lateral areas, the pattern on the medial part appear shaper with MEG.

Inverse analysis

The results from the inverse analysis were compared by means of dipole shift in mm, magnitude error and orientation error in degree. The estimated dipole, which was found with the isotropic model, was compared to the dipole which was used to simulate a potential or field employing an anisotropic model.

As with the results in the forward analysis, density functions were created for the three measures for both modalities. To establish the density plots, the edge defining vector for the dipole shift plots was set from 0 mm to 20 mm with a step size of 0.05 mm, for the magnitude change from 0.2 to 3.4 with a step size of 0.0075 and for the orientation change from 0° to 150° with a step size of 0.5° . Again, non-Gaussian distributions were observed, so that percentile values were used again. The density plots are shown in Fig. 4.21, using the same line style encoding as used for representing the forward study. Similar to the results in the forwards study dipole shifts and orientation changes increase whereas magnitude errors decreases with higher anisotropy in the white matter segment. For the model with *direct* transformed conductivities (light red line) we observe an effect which is between the data from model 1:2 and 1:5, as shown in the graphs in Fig. 4.21 and by the numerical values in Table 4.5. The values for the dipole shift in Table 4.5 clearly demonstrate that MEG is able to localize the dipole more accurately compared to EEG, if anisotropy information is neglected. The values for the magnitude error, however, are very similar for both MEG and EEG. For the orientation error we observe that EEG is somewhat less affect than MEG.

Logarithmized magnitude change Following the procedure for the $\log(MAG)$ in the forward analysis, the logarithmized magnitude changes were determined and plotted as

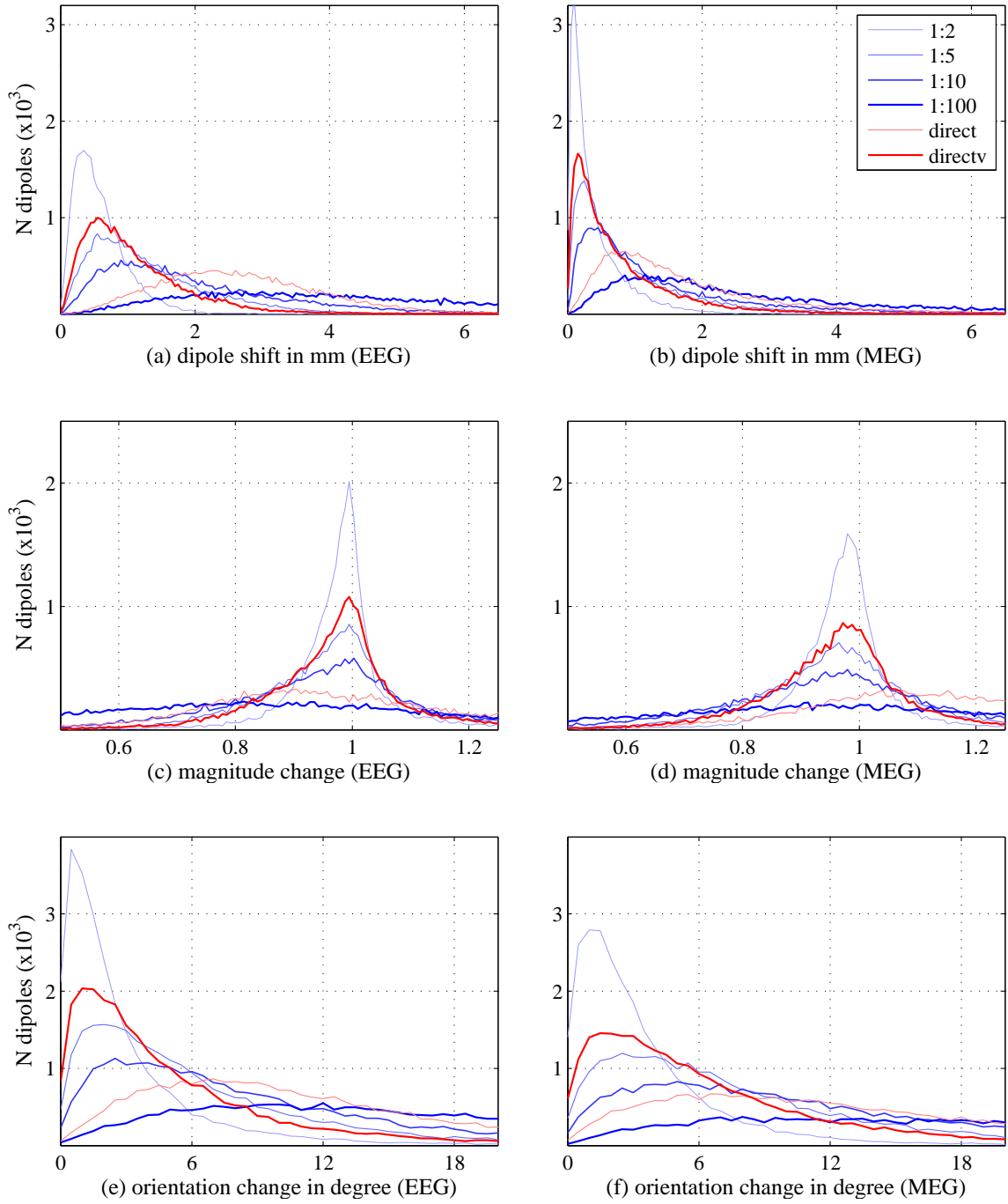


Fig. 4.21.: Density functions for the measures localization error, magnitude error and orientation error derived in the inverse analysis for EEG and MEG modalities.

Tab. 4.5.: Values of dipole shift, magnitude change and orientation change from the 5th, 50th and 95th percentile of the density distributions for the different anisotropic models

measure	modality	1:2	1:5	1:10	1:100	direct	directv
dipole shift [mm]	EEG	0.157	0.301	0.447	1.227	0.959	0.251
		0.532	1.121	1.672	4.284	2.599	0.919
		1.404	3.104	4.720	11.431	4.962	2.618
	MEG	0.059	0.123	0.186	0.547	0.376	0.098
		0.276	0.639	0.938	2.291	1.388	0.545
		1.319	2.923	4.420	10.681	4.607	2.405
magnitude change	EEG	0.846	0.739	0.657	0.413	0.626	0.761
		0.989	0.986	0.985	0.934	1.017	0.988
		1.194	1.597	1.844	2.313	2.475	1.484
	MEG	0.836	0.705	0.620	0.463	0.747	0.736
		0.980	0.972	0.976	1.071	1.176	0.976
		1.170	1.506	1.735	2.750	2.382	1.426
orientation change [°]	EEG	0.371	0.878	1.329	3.576	2.489	0.640
		2.089	4.932	7.122	15.82	10.09	3.848
		10.65	18.48	23.35	43.70	28.02	16.42
	MEG	0.474	1.124	1.697	4.311	2.482	0.830
		2.714	6.465	9.633	22.80	12.29	5.189
		10.85	21.83	30.98	70.40	38.51	19.01

a cumulative distribution function (CDF) (Fig. 4.22). The corresponding percentiles are listed in Table 4.6. Overall, the percentiles are very similar for EEG and MEG. The 5th and 95th percentiles are somewhat higher with MEG, indicating that determination of the dipole magnitude is more influenced by neglecting anisotropic with MEG. With very high anisotropy (100:1), MEG and EEG seem to behave contrary. Their median values are equal, but of opposite sign and more dipoles with higher magnitude were observed with the high anisotropic model.

Result maps Comparing the color overlay maps in Fig. 4.23 and 4.24, which show the three different measure: dipole shift, magnitude change and orientation change for both EEG and MEG, one can see that again, that the pattern for MEG is *sharper* compared to the pattern for EEG. The pattern of the dipole shift was found to be very similar to the RDM pattern shown in Fig. 4.19 and 4.20. The maps for the magnitude changes for EEG and MEG (Fig. 4.23(c,d) and Fig. 4.24(c,d)) reflect the values listed in Table 4.6.

Dipole shifts One outstanding possibility of this study is the ability to visualize the dipole shift using displacement vectors. This not only allows to evaluate the size of

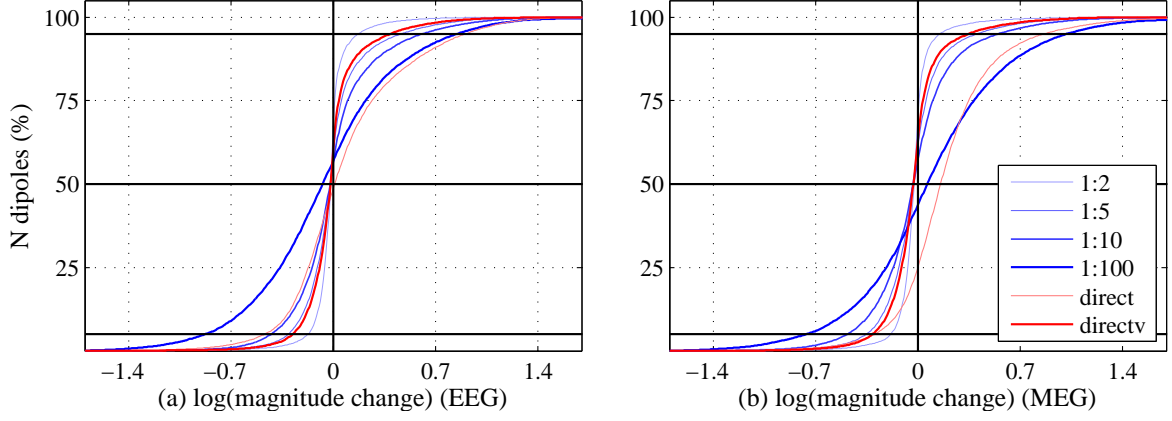


Fig. 4.22.: Cumulative distribution functions for the logarithmized magnitude changes derived in the inverse study for EEG and MEG modalities. Like in Fig. 4.18, the horizontal lines represent the 5th, 50th and 95th percentile level and the vertical line divides the data into positive and negative values. The value at which the graphs intersect the vertical line are shown in Tab. 4.6.

Tab. 4.6.: 5th, 50th and 95th percentile of the logarithmized magnitude changes for the different anisotropic models. The fourth line within each modality shows the amount dipoles in percent which generate a lower magnitude in the anisotropic models compared to the solution in the isotropic model.

measure	modality	1:2	1:5	1:10	1:100	direct	directv
log(mag. change)	EEG	-0.167	-0.303	-0.421	-0.885	-0.468	-0.273
		-0.011	-0.014	-0.015	-0.068	0.016	-0.012
		0.177	0.468	0.612	0.839	0.906	0.395
		60.8%	56.1%	54.3%	56.5%	47.8%	56.6%
	MEG	-0.179	-0.349	-0.478	-0.770	-0.292	-0.306
		-0.020	-0.028	-0.024	0.068	0.162	-0.024
		0.157	0.410	0.551	1.012	0.868	0.355
		65.5%	59.3%	55.7%	43.2%	24.0%	60.5%

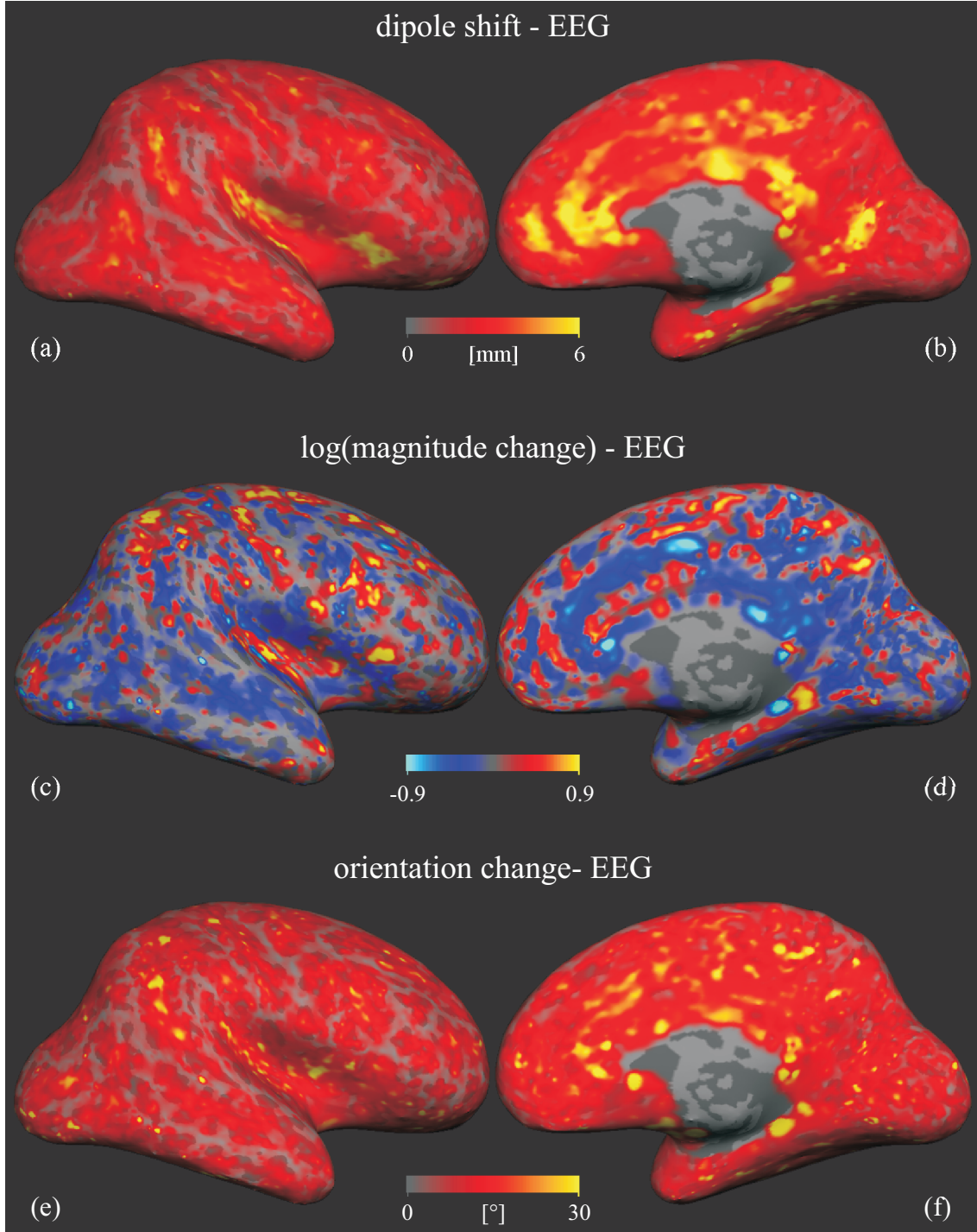


Fig. 4.23.: EEG-Results: Mapping of the measures dipole shift (a,b), magnitude change(c,d) and orientation change (e,f) on the inflated white matter surface of the right hemisphere. The left column (a,c,e) shows the lateral views and the right column (b,d,f) shows the medial views. The gray pattern on the surface delineates sulci (dark gray) from gyri (light gray) areas.

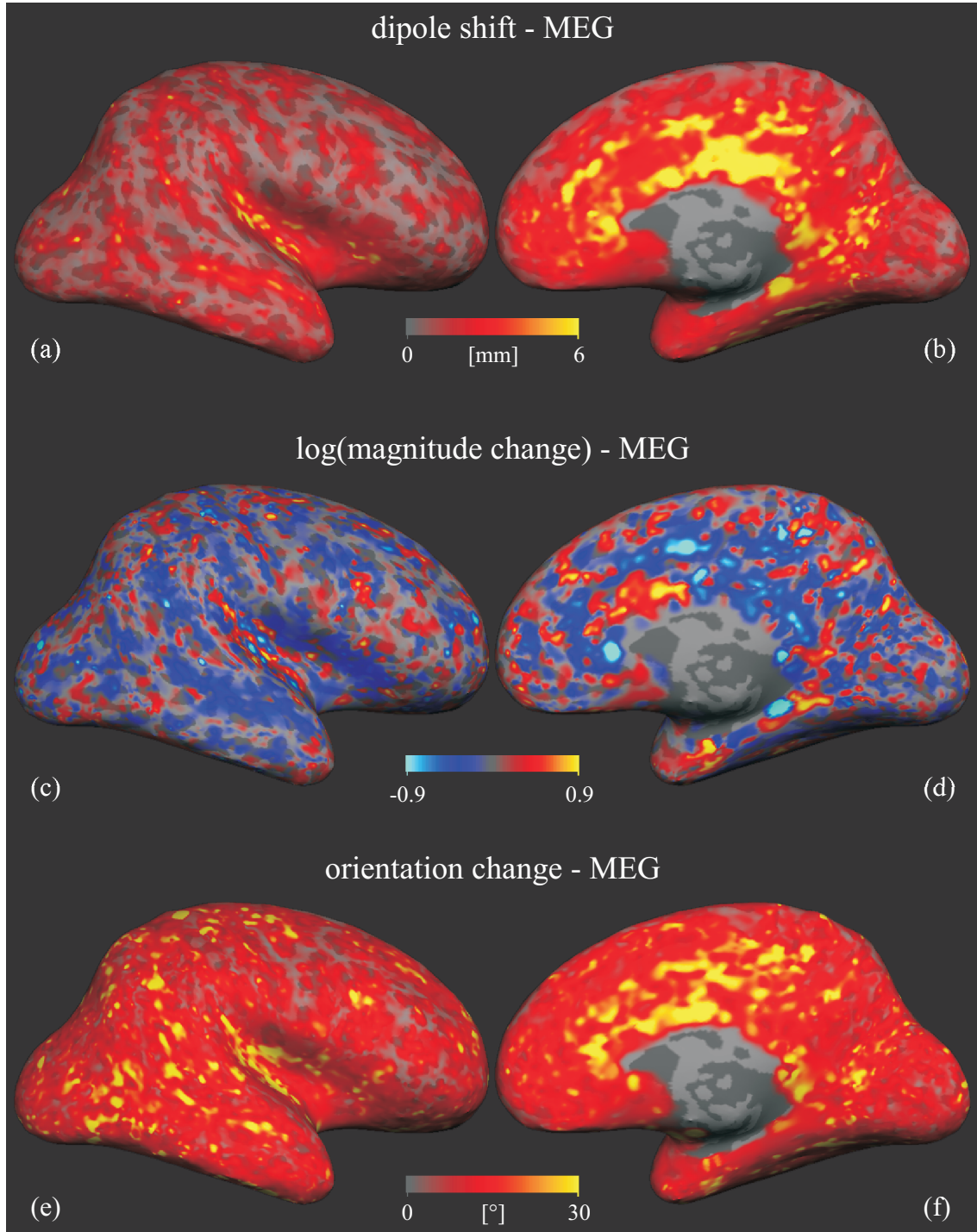


Fig. 4.24.: MEG-Results: Mapping of the measures dipole shift (a,b), magnitude change(c,d) and orientation change (e,f) on the inflated white matter surface of the right hemisphere. The left column (a,c,e) shows the lateral views and the right column (b,d,f) shows the medial views. The gray pattern on the surface delineates sulci (dark gray) from gyri (light gray) areas.

misdisplacement, but also to determine the direction in which the dipole was shifted. To visualize these displacements, a coronal section with a thickness of about 2 cm was selected from the model intersecting regions where the dipole shifts were found to be high. For each dipole within this section a vector connecting the original position and the estimated position was drawn. In order to be able to compare the displacements with respect to the white matter segment and to the conductivity tensor orientations within this segment, the FEM segment for white matter including the tensors is also shown in the figures for MEG and MEG. The coronal slices for EEG and for MEG investigated with the model comprising an artificial anisotropy of 10:1 are shown in Fig. 4.25 and 4.26, respectively. For length comparison a scale indicating the equivalent distance of 1 cm is shown in each sectioning graph.

In particular for EEG it is seen that the displacement vectors (dipole shift) directs out of the sulci. The principal direction is not always directly toward the surface. The direction of the shift appears to be correlated to the orientation of the white matter anisotropy. From the EEG case Fig. 4.25 one can also see, that the dipoles on the top of the gyri are shifted, even though less, toward the white matter segment instead away from it. These effects can also be observed for the MEG case in Fig. 4.26, but as already seen from the values in Table 4.5 and the maps in Fig. 4.24(a,b), the dipole shift smaller with MEG.

4.3.4. Discussion

In this study the sensitivity of the EEG and MEG forward as well as inverse solution on white matter anisotropy was investigated using high resolution finite element volume conductor models of a human head. The information about the anisotropy was derived from diffusion tensor data using different approaches (cf. 3.4.4). The results from the forward analysis show that with increasing anisotropy of the conductivities in the white matter segment the topography error (RDM) as well as the amount of magnitude error increases. RDM was found to be less affected by anisotropy with MEG compared to EEG. In contrast, the magnitude error (MAG) shows similar pattern for EEG and MEG. For a more appropriate evaluation of the magnitude error (MAG) the formalism of $\log(\text{MAG})$ was introduced. The subsequent mapping of the measures RDM and $\log(\text{MAG})$ showed clearly that deep structures in sulci areas are more affected. The maps also revealed that with MEG the amount of the error depends more on the position of the dipole than with EEG, since the MEG maps appear *sharper*. Comparing the different artificial anisotropy ratios with the models generated using the *direct* and *directv* approach, the results from the *directv* model integrate between the models with artificial ratios of 2:1 and 5:1. This is not very surprising, since the mean anisotropy

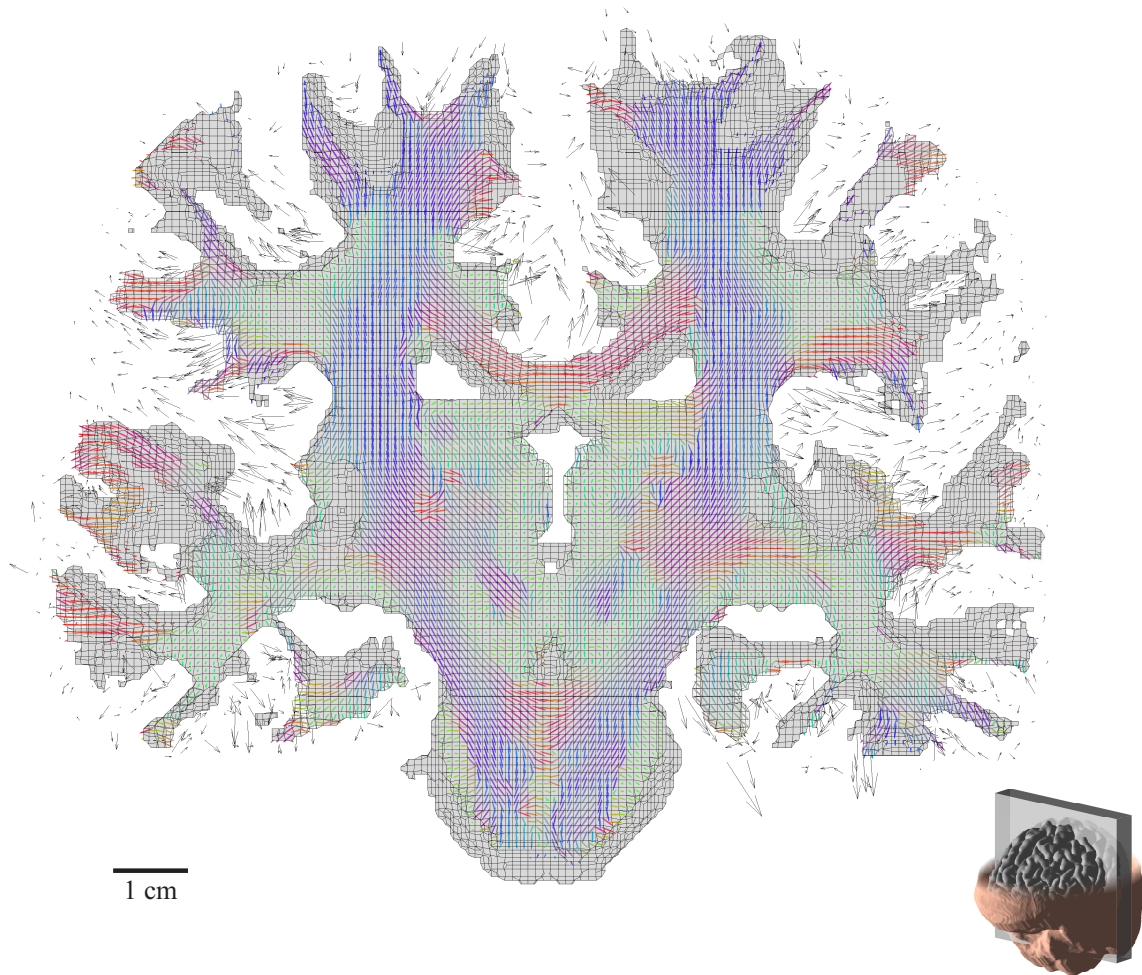


Fig. 4.25.: EEG-Result: Dipole displacements visualized as vectors showing the amount and direction of the dipole shift if an anisotropy of the conductivity of 1:10 is neglected during the inverse procedure. The FE mesh of elements assigned to white matter for the slice section is also shown. In the elements of the forefront the assigned conductivity tensor is drawn. The color of each tensor codes the principal direction (largest eigenvector) of the tensor.

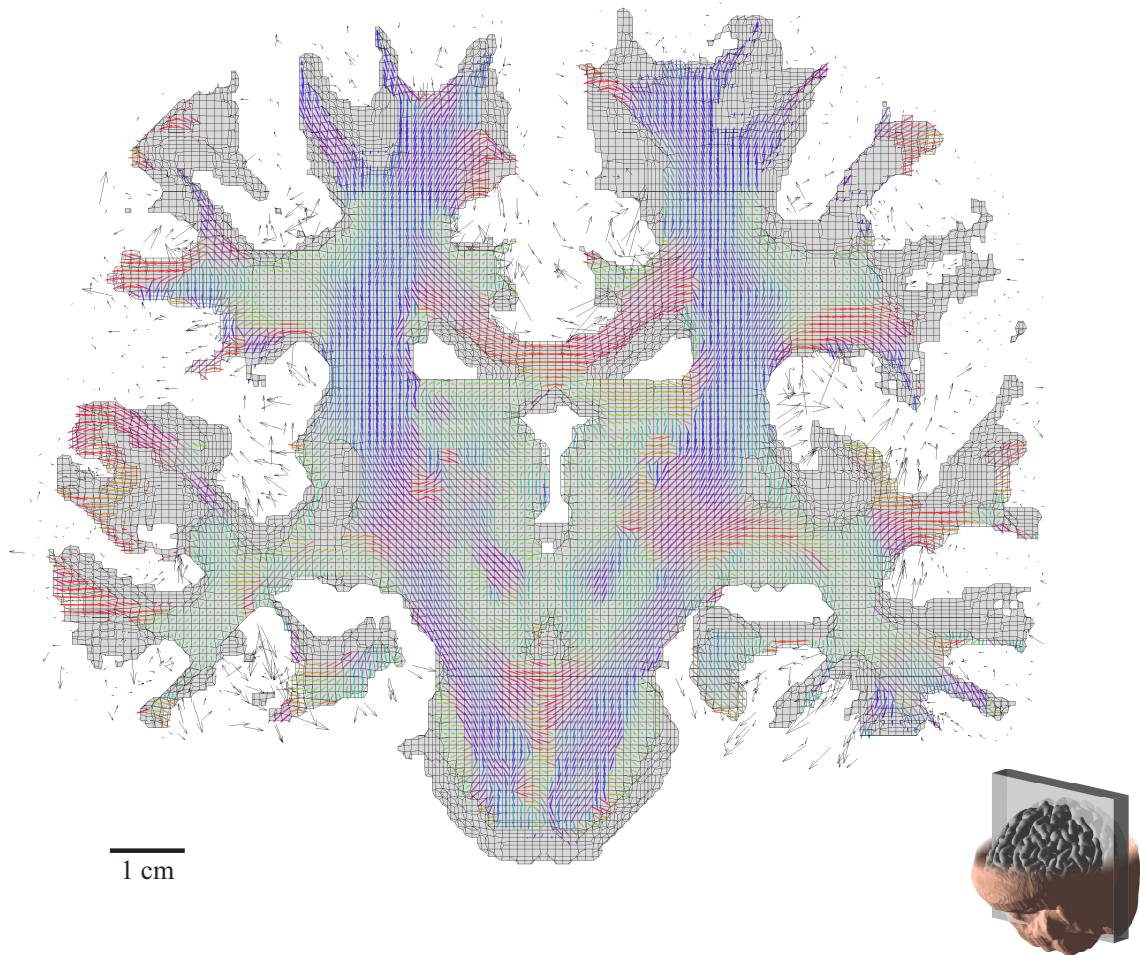


Fig. 4.26.: MEG result inverse anylsis: Dipole displacements visualized as vectors showing the amount and direction of the dipole shift if an anisotropy of the conductivity of 1:10 is neglected during the inverse procedure. The FE mesh of elements assigned to white matter for the slice section is also shown. In the elements of the forefront the assigned conductivity tensor is drawn. The color of each tensor codes the principal direction (largest eigenvector) of the tensor.

ratio for the *directv* model was determined with 3.152:1 as shown in Table 4.2. In contrast, the data derived employing the model generated using the *direct* approach behaves different. RDM, orientation change and magnitude change (inverse analysis) from this model integrate between the artificial models with ratios of 10:1 and 100:1, though the mean anisotropy ratio is also 3.152, but the mean scalar equivalent (σ_{iso}) of the tensors in this model was five times higher than for all other models. Additionally, the MAG values showed different results for EEG and MEG. With EEG the magnitude errors are more decreased, on the other hand increased with MEG.

Comparison of the results to other studies which investigated the influence of white matter anisotropy in the human brain affirm the findings. One of the first studies which investigated the effect of white matter anisotropy on EEG as well as MEG was published by Haueisen et al. [142]. In this study the anisotropy for the FEM model was directly derived from DTI data as proposed by Tuch et al. [42], which corresponds to the *direct* model used in this study, but gray and white matter was model anisotropic. The authors found minor influence of anisotropy on the EEG and MEG topography error (correlation coefficient, which is similar to RDM) but a strong effect on the magnitude. Especially, the statement, that the magnetic field tends to increase in the anisotropic model, whereas the electric potential decreases, can be confirmed completely by this study. As shown in Table 4.4 the mean $\log(\text{MAG})$ for the EEG is -0.113 and 80.7% of the dipoles exhibit lower magnitude compared to the isotropic model. With MEG the mean $\log(\text{MAG})$ was 0.089 and only 16.7% of the dipoles generate a lower magnitude. Since with the *direct* model not only the anisotropy ratio changes from 1:1 to around 3.152:1, but also the mean scalar representation of the tensors σ_{iso} increases by a factor of 3.8 from 0.14 to 0.531 (see Table. 4.2).

Anwander et al. [149] presented a study which investigated not only anisotropic white matter but also the influence of an anisotropic skull layer. The conductivity tensors for the white matter segment were determined using the orientation (eigenvectors) from a diffusion tensor measurement and the eigenvalues were selected to model anisotropies of 2:1 5:1 and 10:1, as performed in this study for the models with artificial anisotropy ratios. They found that with increasing white matter anisotropy the RDM for the radial and, even though less, for the tangential source increases with EEG, whereas the amount of RDM for the investigated anisotropy ratios is between the 50th and 95th percentile compared to the results of this study. The effect of skull anisotropy, which was not considered in the present study, was only found to affect the results of the forward analysis for the radial oriented dipole with EEG. With MEG they found, that skull anisotropy has a negligible effect on the forwards solution. However, the white matter anisotropy, shows to have an effect on the MEG forward solution of an radial source (much larger compared to the tangential source) and it is explained by the authors that

tissue anisotropy only affects the secondary (conducting) currents and the ratio of the secondary to the whole magnetic flux (cf. Eq. (4.6)) increases with the ratio of the radial dipole orientation component. An inverse analysis in the study of Anwander et al. [149] investigated the localization error with EEG if an anisotropy of 10:1 is neglected. The determined localization errors for 43 radial and 46 tangential dipoles were found to be 5.1 mm on average for the radial sources and 8.8 mm on tangential sources. This is far above the values derived in the present study, where an localization error of 1.6 mm (50th percentile) and 4.72 mm (95th percentile) was observed for an anisotropy of 10:1. This could be explained by the fact, that the dipoles used by Anwander et al. were placed very closed to or even in the white matter segment.

Wolters et al. studied the influence of skull and white matter anisotropy on EEG and MEG forward and an inverse solution in a high resolution FEM model [144]. The model was also set up using an artificial white matter and skull anisotropy, whereas the skull anisotropy ratio was set to 10:1 and for the white matter anisotropy ratios of 2:1, 5:1, 10:1 and 100:1 were assumed, like in the presented study. Three different dipole configuration were investigated: a tangential, a radial and a deep thalamic (close to the Thalamus) source. For all three dipole configurations the results of the forward analysis are comparable to the results of the presented study. RDM for both MEG and EEG increases with nearly the same gradient, if the anisotropy of the white matter segment increases. But the amount of RDM determined by Wolters et al. corresponds approximately to the 95th percentile determined in the present study. Similar results were also found for the MAG results, but as with the RDM only the most 5th percentile (most decreased) corresponds to the data from Wolters et al.. This shows that it is necessary to investigate not only a few dipole configurations in order to determine the sensitivity of the anisotropy to the forward and inverse solution in EEG and MEG.

Hallez et al. performed investigations with EEG on skull and white matter anisotropy using a finite difference method (FDM) model consisting of 5 concentric shells [152]. Considering only the effect of white matter anisotropy they found localization error of, on average, 11.21 mm with a maximum of 26.3 mm, and if skull anisotropy is also considered, the average localization error was found to increase to 13.73 mm with a maximum of 24.51 mm. However, these results are difficult to compare to the this study, since Hallez et al. used a spherical shaped model and FDM instead of FEM.

Several studies investigated the influence of anisotropic conductivity of the skull on EEG [143, 123, 154]. The results of these studies are very similar indicating that skull anisotropy causes a smearing effect on the surface potential, which leads to errors in the inverse solution if the skull layer is neglected. The effect of skull anisotropy on MEG is considered in [155, 124, 149, 144, 124] showing that anisotropy of the skull layer can in general be neglected.

However, not only neglecting anisotropy can lead to errors in EEG/MEG source localization studies. Broek et al. [124] showed that a hole in the skull can have a large effect on EEG, especially if the source is directly under the hole and localization errors up to 15 mm may occur. Similar effects considering holes in the skull were shown in [156] and [157]. Also lesions have to be taken into account if the source is close to it [124]. The EEG as well as the MEG forward solution was found to be sensitive to conductivity changes in the vicinity of the source changes [131]. With EEG this holds true also if the conductivity in the vicinity of the sensors (electrodes) changes [131].

Further studies investigated the effect of uncertainties of conductivity values on the EEG solution [147, 158, 159, 160], with the result, that if the conductivities of the head tissues and the distribution of these tissues throughout the head are modeled accurately, localization accuracy to within a few millimeters is achievable. Also the advantage of realistic head models in comparison to spherical or ellipsoidal shaped models were investigated [161, 162, 163, 164]. In general the localization error due to the use of inadequate spherical models was found to be between 5 mm up to 20 mm.

The effect of anisotropic conductivity was also investigated with transcranial magnetic stimulation (TMS) [165], showing that anisotropy has minor effects both on the position of the main focus of activation and on its intensity and a considerably more effect on the spatial distribution of the induced electric field. Also the effect on deep brain stimulation (DBS) was investigated. Butson et al. and McIntyre et al. [166, 167, 168] substantiate an effect of white matter anisotropy on the potential distribution in the patient's head, when applying deep brain stimulation (DBS). Both, TMS as well as DBS studies, generated the necessary volume conductor models comprising anisotropic segments based on DTI data.

The use of anisotropic conductivity models is not limited to the head or brain. Comparing the forward solution of a human heart modeled with isotropic and anisotropic myocardium showed that the body surface potentials (BSPMs) [169, 170] as well as the current density distribution [171, 172] changes sometimes dramatically. The idea to derive the conductivity tensors or the fiber orientation for the myocardial layer from DTI is not as easy to apply as it is with the brain. The standard MR acquisition techniques used for the brain are not appropriate for the moving heart. But MR imaging techniques have been developed [173] to tackle these problems and measure DTI of the heart in vivo [174], so that it might be possible to generate realistic volume conductor models of the heart based on DTI data.

A big issue with all these simulation studies is the lack of validation. One way to perform a validation in order to reveal if the anisotropic model achieves more accurate results in EEG/MEG source localization is to use implanted sources [175, 176, 177]. However, these studies showed that the attainable accuracy (minimal localization error)

is above the observed localization error found in the present study, but these studies used volume conductor models (spherical models or boundary element models) which are known to do not achieve a better accuracy. Liehr et al. [178] showed experimentally the influence of anisotropic conductivity on the magnetic field and the electric surface potential using an artificial dipole placed within an anisotropic compartment. They found that for electric and magnetic measurements, the angle difference between observed signal orientations and true dipole orientations continuously increase with the angle between dipole and anisotropy up to 80° and then decrease back to zero at their orthogonal orientation. Liehr et al. also showed that both, EEG and MEG signal, decreases with increasing angle between dipole and anisotropy, and proposes furthermore, that the magnetic field shows a generally stronger shape change, while the changed shape of the electric potential shows similarity to an extended source, which is in accordance with the findings of the present study.

Comparison of the results of human model with the study which employed the animal model revealed a larger influence of the white matter anisotropy with the human model. With the animal model neglecting the anisotropy information in the inverse procedure lead to localization errors up to 0.84 mm and 1.26 mm for radial and tangential sources, respectively. Whereas, with the human model, the 95th percentile for the localization error was 4.72 mm for EEG. In the animal study the largest deviations measured using RDM and MAG were found, when dipoles are placed between anisotropic segments. This could be confirmed with the human study if one considers the cortical ribbon in the sulci areas as positions, which are between anisotropic segments. The same holds true for the findings considering the dipole orientation, where a stronger influence on tangential dipoles was found in the animal study. If one considers dipoles oriented perpendicular in the cortical ribbon used in the human model, the dipoles on the crown of the gyri are oriented more radially and in the sulci more tangentially with respect to the surface of the model. As in the study using the human model positive as well as negative magnitude changes were observed in the animal model, depending on the orientation of the dipole with respect to the white matter segment. In contrast to the animal study a visual comparison between the RDM mapping in the forward solution and the localization error in the inverse analysis suggests a correlation between these two quantities in the human model, however, a numerical correlation could not be determined.

In general the findings of this study are very complex and have to be interpreted considering all limitations. First, the models of only one individual individual subject were investigated, so that a generalization for other studies can not be applied directly. Secondly, only dipoles in the cortical ribbon were investigated assuming that the typical dipolar source is oriented parallel to the pyramidal cells in the cortex and

thus perpendicular to the white matter surface. The influence on deeper (thalamic) sources was not investigated. Thirdly, only the white matter anisotropy was modeled using anisotropic conductivity, although the skull is also known to conduct anisotropy, however, the information about skull anisotropy could not be determined using diffusion tensor imaging. Fourthly, the results of the inverse study do not consider noise in the input data, which would increase the quantities and may have a higher influence on the localizations errors as observed by neglecting the anisotropy. And fifthly, the different conductivity values (for scalp, gray and white matter, CSF and skull) assigned to the isotropic parts of the model and used to generate the artificial anisotropic white matter segment are taken from the literature and were assumed to be correct. If this assumption fails, the effects on the results could change dramatically, so that they are not transferable to experimental validation and other studies investigating white matter anisotropy.

Despite these limitations, the presented study showed that it is possible to investigate the influence of anisotropic conductivity on the forward and inverse problem in EEG and MEG. The effects which were observed are manifold and demonstrate the complexity of the problem. To the best of my knowledge up to now no other study showed the effect of anisotropic conductivity of white matter in such a great detail. Especially the mapping of the error quantities for the whole cortex of the a human brain and the demonstration of the localization shift within the sulci areas are unique. Despite the fact that only one individual subject was used in this study, the results might help to identify localization errors due to anisotropy in EEG/MEG source localization studies. For example, it is known that there are several white matter disease like Alzheimer, multiple sclerosis and Shizophrenia, which are known to show differences in the white matter structure [179,180,181,182,183,184] compared to healthy subjects. These local changes in white matter might change the conductivity in particular the anisotropy at the position of the lesions. A dipolar source in the vicinity of such regions would generate a different electrical surface potential or magnetic field compared to a source at the same position in a healthy subject. Such effects were observed in [185,186]. But the use of diffusion tensor imaging to generate anisotropic volume conductor models could also be used in case of stroke patients with large lesions, which are known to have a strong influence on the EEG as well as MEG forward solution [124]. Such lesions appear as isotropic regions with reduced diffusivity (ADC) compared to healthy tissue and thus it is easy to identify and incorporate such regions into the volume conductor model using the diffusion tensor data. Finally, it is claimed that if one uses high resolution volume conductor models for EEG/MEG studies, the anisotropy of the tissue has to be considered, since the average error of neglecting anisotropy is larger than the accuracy that can be achieved using such models.

5. Conclusion and Outlook

In the present work anisotropic electric tissue properties were modeled into high resolution finite element volume conductors by means of diffusion tensor imaging. The first part of the work showed the influence of not considering imaging gradient in the calculation of the b-matrices on the correct determination of diffusion tensor data and it was found that especially with high resolution imaging protocols the contributions of the imaging gradients are not negligible. It was also shown how correct b-matrices, considering all applied gradients, can be calculated correctly. For the case that information about the sequence are missing an experimental approach of determining a parameterized b-matrix using phantom measurements is proposed. In the second part the procedure of generating anisotropic volume conductor models is regarded. The main focus of this part was to demonstrate the possibility to derive anisotropy information from DTI measurements and the inclusion of this information into an anisotropic volume conductor. It was also shown, that it is possible to generate a sophisticated high resolution anisotropic model without any manual steps into five different tissue layers. The third part studied the influence of anisotropic white matter employing an animal as well as a human model. To compare the different ways of comprising the anisotropy information from DTI in the volume conductor model, different models having artificial as well as measured anisotropy were investigated. In the animal study the EEG and in the human study the EEG and MEG forward solution simulated using the anisotropic models was compared to the solution derived using the isotropic model. It was found that both, the topography error (RDM) as well as the magnitude error (MAG), showed to be affected significantly if anisotropy is considered in the volume conductor. It was also shown, that the position as well as the orientation of the dipole with respect to white matter has a large effect on the amount of the error quantities. In the inverse studies the effect of neglecting anisotropy information was investigated. The results showed similar effect for the animal and the human model. In the animal study, additionally to the use of a realistic modeled white matter segment, the use of an artificial cube showed that the effects mainly depend on the geometry of the anisotropic segment and on the orientation of the source with respect to that segment, but not to the orientation of the anisotropy within the anisotropic segment. For the human study small localization errors due to neglecting anisotropy were found, which are smaller

5. *Conclusion and Outlook*

compared to errors which would be expected if other modeling errors like misclassified tissue or the use of non realistic head models apply. However, if high resolution FE models were used to perform source localization in EEG and MEG experiments and the quality of the measured data permits a localization accuracy of 1 mm and below, the influence of anisotropic compartments can not be neglected anymore.

Further studies have to be performed to validate the findings. Such a validation could be performed using an artificial dipole with known position and orientation, but any part of the whole validation procedure has to be performed as accurate as possible with measurement uncertainties in each separate step which are smaller than the expected effect. Furthermore, the effect of local white matter changes which were found in several diseases like multiples sclerosis, schizophrenia and Alzheimer should be investigated regarding differences in source localization between patients and subjects. Also the effect of lesions in acute stroke modeled into a volume conductor using diffusion tensor data should be evaluated.

Bibliography

- [1] Human brain, April 2008. Wikipedia, http://en.wikipedia.org/wiki/Human_brain.
- [2] R. H. Wilkins. Neurosurgical classic-xvii. edwin smith surgical papyrus. *J Neurosurgery*, 21:240–244, 1964.
- [3] History of the brain, April 2008. Wikipedia, http://en.wikipedia.org/wiki/History_of_the_brain.
- [4] M. F. Bear, B. W. Connors, and M. A. Paradiso. *Neuroscience: Exploring the Brain*. Baltimore: Lippincott, 2001.
- [5] P. Dear. *Revolutionizing the Sciences: European Knowledge and Its Ambitions, 1500-1700*. Princeton, NJ: Princeton University Press, 2001.
- [6] T. Schwann and M. J. Schleyden. *Microscopical researches into the accordance in the structure and growth of animals and plants*. London: Printed for the Sydenham Society, 1847.
- [7] J.-B. Lamarck. *Philosophie Zoologique*. Paris, 1809.
- [8] H. Dutrochet. *Anatomical and Physiological Researches on the Intimate Structures of Animals and Plants, and Their Motility*. Paris, 1824.
- [9] Pyramidal hippocampal neuron, June 2007. Wikipedia, http://commons.wikimedia.org/wiki/Image:Pyramidal_hippocampal_neuron_40x.jpg.
- [10] W. Pravdich-Neminsky. Ein Versuch der Registrierung der elektrischen Gehirnerscheinungen. *Zbl Physiol*, 27:951–960, 1913.
- [11] H. Berger. *Über das Elektrenkephalogramm des Menschen*. Freiburg, 2004.
- [12] D. Cohen. Magnetoencephalography: evidence of magnetic fields produced by alpha-rhythm currents. *Science*, 161(843):784–786, Aug 1968.

- [13] J. E. Zimmerman, P. Theine, and J. T. Harding. Design and operation of stable rf-biased superconducting point-contact quantum devices, etc. *J Appl Phys*, 41:1572–1580, 1970.
- [14] D. Cohen. Magnetoencephalography: detection of the brain’s electrical activity with a superconducting magnetometer. *Science*, 175:664–66, 1972.
- [15] W. G. Walter and H. W. Shipton. A new toposcopic display system. *Electroencephalogr Clin Neurophysiol*, 3(3):281–292, Aug 1951.
- [16] J. C. de Munck and M. Peters. A fast method to compute the potential in the multi sphere model. *IEEE Trans Biomed Eng*, 40:1166–1174, 1993.
- [17] J.C. de Munck. The potential distribution in a layered anisotropic spheroidal volume conductor. *J Appl Phys*, 64:465–469, 1988.
- [18] M. S. Hämmäläinen and J. Sarvas. Realistic conductivity geometry model of the human head for interpretation of neuromagnetic data. *IEEE Trans Biomed Eng*, 36(2):165–171, Feb 1989.
- [19] J. W. Meijs, O. W. Weier, M. J. Peters, and A. van Oosterom. On the numerical accuracy of the boundary element method. *IEEE Trans Biomed Eng*, 36(10):1038–1049, Oct 1989.
- [20] J. C. de Munck. A linear discretization of the volume conductor boundary integral equation using analytically integrated elements. *IEEE Trans Biomed Eng*, 39:986–990, 1992.
- [21] M. Fuchs, R. Drenckhahn, H. A. Wischmann, and M. Wagner. An improved boundary element method for realistic volume-conductor modeling. *IEEE Trans Biomed Eng*, 45(8):980–997, Aug 1998.
- [22] J. Haueisen. *Methods of numerical field calculation for neuromagnetic source localization*. PhD thesis, Technical University Ilmenau, Germany, June 1996. ISBN 3-8265-1691-5.
- [23] H. Buchner, G. Knoll, M. Fuchs, A. Rienäcker, R. Beckmann, M. Wagner, J. Silny, and J. Pesch. Inverse localization of electric dipole current sources in finite element models of the human head. *Electroencephalogr Clin Neurophysiol*, 102(4):267–278, Apr 1997.
- [24] K. A. Awada, D. R. Jackson, J. T. Williams, D. R. Wilton, S. B. Baumann, and A. C. Papanicolaou. Computational aspects of finite element modeling in eeg source localization. *IEEE Trans Biomed Eng*, 44(8):736–752, Aug 1997.

- [25] L. A. Geddes and L. E. Baker. The specific resistance of biological material—a compendium of data for the biomedical engineer and physiologist. *Med Biol Eng*, 5(3):271–293, May 1967.
- [26] W. H. Freygang and W. M. Landau. Some relations between resistivity and electrical activity in the cerebral cortex of the cat. *J Cell Physiol*, 45(3):377–392, Jun 1955.
- [27] A. van Harreveld, T. Murphy, and K. W. Nobel. Specific impedance of rabbit’s cortical tissue. *Am J Physiol*, 205:203–207, Jul 1963.
- [28] G. W. Crile, H. R. Hosmer, and A. F. Rowland. The electrical conductivity of animal tissues under normal and pathological conditions. *Am J Physiol*, 60:59–106, 1922.
- [29] J. Haueisen. Numerische Berechnung und Analyse biomagnetischer Felder. Habilitation, Technische Universität Ilmenau, Deutschland, 2002.
- [30] H. J. Wieringa. *MEG, EEG and the Integration with Magnetic Resonance Images*. PhD thesis, University of Twente, Enschede, The Netherlands, October 1993.
- [31] A Generic Environment for Bionumerical Simulation. IST Programme Framework V Project IST-1999-10378, 1999-2003. Simbio, <http://www.simbio.de>.
- [32] P. C. Lauterbur. Image formation by induced local interactions: Examples employing nuclear magnetic resonance. *Nature*, 242:190–191, 1973.
- [33] A. Kumar, D. Welti, and P.R. Ernst. Nmr fourier zeugmotography. *J Magn Reson*, 18(1):69–83, 1975.
- [34] P. Mansfield. Multi-planar image formation using nmr spin echoes. *J Phys C Solid State*, 10(3):55–58, 1977.
- [35] B. Chapman, R. Turner, R. J. Ordidge, M. Doyle, M. Cawley, R. Coxon, P. Glover, and P. Mansfield. Real-time movie imaging from a single cardiac cycle by nmr. *Magn Reson Med*, 5:246–254, 1987.
- [36] C. L. Dumoulin, S. P. Souza, and H. R. Hart. Rapid scan magnetic resonance angiography. *Magn Reson Med*, 5:238–245, 1987.
- [37] H. C. Torrey. Bloch equations with diffusion terms. *Phys Rev*, 104(3):563–565, 1956.

- [38] E. O. Stejskal and J. E. Tanner. Spin diffusion measurements: Spin echoes in the presence of a time-dependent field gradient. *J Chem Phys*, 42(1):288–292, 1965.
- [39] D. LeBihan. Ivim method measures diffusion and perfusion. *Diagn Imaging (San Franc)*, 12(6):133–133, 1990.
- [40] P. J. Basser, J. Mattiello, and D. LeBihan. Estimation of the effective self-diffusion tensor from the nmr spin echo. *J Magn Reson B*, 103(3):247–254, Mar 1994.
- [41] D. S. Tuch, V. J. Wedeen, A. M. Dale, J. S. George, and J. W. Belliveau. Conductivity mapping of biological tissue using diffusion mri. *Ann N Y Acad Sci*, 888:314–316, Oct 1999.
- [42] D. S. Tuch, V. J. Wedeen, A. M. Dale, J. S. George, and J. W. Belliveau. Conductivity tensor mapping of the human brain using diffusion tensor mri. *Proc Natl Acad Sci U S A*, 98(20):11697–11701, Sep 2001.
- [43] J. Sedlacik. *New Advances in Susceptibility Weighted MRI to Determine Physiological Parameters*. PhD thesis, Technical University Ilmenau, 2007.
- [44] J. M. Hutchison, R. J. Sutherland, and J. R. Mallard. Nmr imaging: image recovery under magnetic fields with large non-uniformities. *J Phys [E]*, 11(3):217–21, 1978.
- [45] G. Johnson, J. M. S. Hutchison, T. W. Redpath, and L. M. Eastwodd. Improvements in performance time for simultaneous three-dimensional nmr imaging. *J Magn Reson*, 54(3):374–384, 1983.
- [46] E. L. Hahn. Spin echoes. *Phys Rev*, 80:580–594, 1950.
- [47] F. Bloch. Nuclear induction. *Phys Rev*, 70(7):460–474, 1946.
- [48] C. R. Becker, L. R. Schad, and W. J. Lorenz. Measurement of diffusion coefficients using a quick echo split nmr imaging technique. *Magn Reson Imaging*, 12(8):1167–1174, 1994.
- [49] J. Fischer and A. Weiss. Transport properties of liquids. v. selfdiffusion, viscosity, and mass density of ellipsoidal shaped molecules in the pure liquid phase. *Berichte der Bunsen-Gesellschaft-Physical Chemistry Chemical Physics*, 90(10):896–905, Oct 1986.
- [50] G. Graner, E. Hirota, T. Iijima, K. Kuchitsu, D. A. Ramsay, J. Vogt, and N. Vogt. *Structure Data of Free Polyatomic Molecules. Inorganic Molecules.*, volume 25A. Berlin: Springer-Verlag, Landolt-Börnstein New Series II edition, 1998.

- [51] W. S. Price. Pulsed-field gradient nuclear magnetic resonance as a tool for studying translational diffusion: Part 1. basic theory. *Concepts Magn Reson*, 9(5):299–336, 1997.
- [52] J. Mattiello, P. J. Basser, and D. Le Bihan. The b matrix in diffusion tensor echo-planar imaging. *Magn Reson Med*, 37(2):292–300, Feb 1997.
- [53] M. Neeman, J. P. Freyer, and L. O. Sillerud. A simple method for obtaining cross-term-free images for diffusion anisotropy studies in nmr microimaging. *Magn Reson Med*, 21(1):138–143, Sep 1991.
- [54] M. Neeman, J. P. Freyer, and L. O. Sillerud. Pulsed-gradient spin-echo diffusion studies in nmr imaging. effects of the imaging gradients on the determination of diffusion coefficients. *J Magn Reson*, 90(2):303–312, 1990.
- [55] D. Güllmar, J. Haueisen, and J. R. Reichenbach. Analysis of b-value calculations in diffusion weighted and diffusion tensor imaging. *Concepts Magn Reson*, 25A:53–66, Mar 2005.
- [56] P. W. Holland and R. E. Welsch. Robust regression using iteratively reweighted least-squares. *Communications in Statistics: Theory and Methods*, A6:813–827, 1977.
- [57] T. G. Reese, O. Heid, R. M. Weisskoff, and V. J. Wedeen. Reduction of eddy-current-induced distortion in diffusion mri using a twice-refocused spin echo. *Magn Reson Med*, 49(1):177–82, 2003.
- [58] K. D. Merboldt, W. Hänicke, and J. Frahm. Diffusion imaging using stimulated echoes. *Magn Reson Med*, 19(2):233–239, Jun 1991.
- [59] M. N. Yongbi, S. Ding, and J. F. Dunn. A modified sub-second fast-steam sequence incorporating bipolar gradients for in vivo diffusion imaging. *Magn Reson Med*, 35(6):911–916, Jun 1996.
- [60] K. A. Il’yasov and J. Hennig. Single-shot diffusion-weighted rare sequence: application for temperature monitoring during hyperthermia session. *J Magn Reson Imaging*, 8(6):1296–1305, 1998.
- [61] R. Turner, D. Le Bihan, J. Maier, R. Vavrek, L. K. Hedges, and J. Pekar. Echo-planar imaging of intravoxel incoherent motion. *Radiology*, 177(2):407–414, Nov 1990.

- [62] R. Turner, D. Le Bihan, and A. S. Chesnick. Echo-planar imaging of diffusion and perfusion. *Magn Reson Med*, 19(2):247–253, Jun 1991.
- [63] D. Le Bihan, R. Turner, and P. Douek. Is water diffusion restricted in human brain white matter? an echo-planar nmr imaging study. *Neuroreport*, 4(7):887–890, Jul 1993.
- [64] U. G. Nolte, J. Finsterbusch, and J. Frahm. Rapid isotropic diffusion mapping without susceptibility artifacts: whole brain studies using diffusion-weighted single-shot steam mr imaging. *Magn Reson Med*, 44(5):731–736, Nov 2000.
- [65] J. Carballido-Gamio, D. Xu, D. Newitt, E. T. Han, D. B. Vigneron, and S. Majumdar. Single-shot fast spin-echo diffusion tensor imaging of the lumbar spine at 1.5 and 3 t. *Magn Reson Imaging*, 25(5):665–670, Jun 2007.
- [66] J. E. Sarlls, R. D. Newbould, M. I. Altbach, A. F. Gmitro, J. Seeger, and T. P. Trouard. Isotropic diffusion weighting in radial fast spin-echo magnetic resonance imaging. *Magn Reson Med*, 53(6):1347–1354, Jun 2005.
- [67] D. K. Jones. The effect of gradient sampling schemes on measures derived from diffusion tensor mri: a monte carlo study. *Magn Reson Med*, 51(4):807–15, 2004.
- [68] D. K. Jones, M. A. Horsfield, and A. Simmons. Optimal strategies for measuring diffusion in anisotropic systems by magnetic resonance imaging. *Magn Reson Med*, 42(3):515–25, 1999.
- [69] S. Skare, M. Hedehus, M. E. Moseley, and T. Q. Li. Condition number as a measure of noise performance of diffusion tensor data acquisition schemes with mri. *J Magn Reson*, 147(2):340–52, 2000.
- [70] N. G. Papadakis, D. Xing, C. L. Huang, L. D. Hall, and T. A. Carpenter. A comparative study of acquisition schemes for diffusion tensor imaging using mri. *J Magn Reson*, 137(1):67–82, 1999.
- [71] P. G. Batchelor, D. Atkinson, D. L. Hill, F. Calamante, and A. Connelly. Anisotropic noise propagation in diffusion tensor mri sampling schemes. *Magn Reson Med*, 49(6):1143–51, 2003.
- [72] C. Pierpaoli and P. J. Basser. Toward a quantitative assessment of diffusion anisotropy. *Magn Reson Med*, 36(6):893–906, 1996.
- [73] P. J. Basser and C. Pierpaoli. Microstructural and physiological features of tissues elucidated by quantitative-diffusion-tensor mri. *J Magn Reson B*, 111(3):209–219, Jun 1996.

- [74] S. Pajevic and C. Pierpaoli. Color schemes to represent the orientation of anisotropic tissues from diffusion tensor data: application to white matter fiber tract mapping in the human brain. *Magn Reson Med*, 42(3):526–40, 1999.
- [75] J. C. Maxwell. A dynamical theory of the electromagnetic field. *Royal Society Transactions*, 155:459–512, 1865.
- [76] J. Haueisen, C. Ramon, M. Eiselt, H. Brauer, and H. Nowak. Influence of tissue resistivities on neuromagnetic fields and potentials studied with a finite element model of the head. *IEEE Trans Biomed Eng*, 44(8):727–735, 1997.
- [77] R. Pohlmeier, H. Buchner, G. Knoll, A. Rienacker, R. Beckmann, and J. Pesch. The influence of skull-conductivity misspecification on inverse source localization in realistically shaped finite element head models. *Brain Topogr*, 9(3):157–162, 1997.
- [78] P. W. Nicholson. Specific impedance of cerebral white matter. *Exp Neurol*, 13(4):386–401, Dec 1965.
- [79] F. L. Gielen, H. E. Cruts, B. A. Albers, K. L. Boon, W. Wallinga de Jonge, and H. B. Boom. Model of electrical conductivity of skeletal muscle based on tissue structure. *Med Biol Eng Comput*, 24(1):34–40, Jan 1986.
- [80] Y. C. Okada, J. C. Huang, M. E. Rice, D. Tranchina, and C. Nicholson. Origin of the apparent tissue conductivity in the molecular and granular layers of the in vitro turtle cerebellum and the interpretation of current source-density analysis. *J Neurophysiol*, 72(2):742–753, Aug 1994.
- [81] A. R. Gardner-Medwin and C. Nicholson. Changes of extracellular potassium activity induced by electric current through brain tissue in the rat. *J Physiol*, 335:375–392, Feb 1983.
- [82] C. Nicholson and J. M. Phillips. Ion diffusion modified by tortuosity and volume fraction in the extracellular microenvironment of the rat cerebellum. *J Physiol*, 321:225–257, Dec 1981.
- [83] S. B. Baumann, D. R. Wozny, S. K. Kelly, and F. M. Meno. The electrical conductivity of human cerebrospinal fluid at body temperature. *IEEE Trans Biomed Eng*, 44(3):220–223, Mar 1997.
- [84] C. H. Wolters. *Influence of Tissue Conductivity Inhomogeneity and Anisotropy on EEG/MEG based Source Localization in the Human Brain*. PhD thesis, University Leipzig, Germany, 2002.

- [85] T. F. Oostendorp, J. Delbeke, and D. F. Stegeman. The conductivity of the human skull: results of in vivo and in vitro measurements. *IEEE Trans Biomed Eng*, 47(11):1487–1492, Nov 2000.
- [86] J. B. Ranck. Specific impedance of rabbit cerebral cortex. *Exp Neurol*, 7:144–152, Feb 1963.
- [87] O. Kwon, E. J. Woo, J. R. Yoon, and J. K. Seo. Magnetic resonance electrical impedance tomography (mreit): simulation study of j-substitution algorithm. *IEEE Trans Biomed Eng*, 49(2):160–167, Feb 2002.
- [88] S. H. Oh, J. Y. Han, S. Y. Lee, M. H. Cho, B. I. Lee, and E. J. Woo. Electrical conductivity imaging by magnetic resonance electrical impedance tomography (mreit). *Magn Reson Med*, 50(4):875–878, Oct 2003.
- [89] H. S. Khang, B. I. Lee, S. H. Oh, E. J. Woo, S. Y. Lee, M. H. Cho, O. Kwon, J. R. Yoon, and J. K. Seo. J-substitution algorithm in magnetic resonance electrical impedance tomography (mreit): phantom experiments for static resistivity images. *IEEE Trans Med Imaging*, 21(6):695–702, Jun 2002.
- [90] S. H. Lee, J. K. Seo, C. Park, B. I. Lee, E. J. Woo, S. Y. Lee, O. Kwon, and J. Hahn. Conductivity image reconstruction from defective data in mreit: numerical simulation and animal experiment. *IEEE Trans Med Imaging*, 25(2):168–176, Feb 2006.
- [91] N. G. Gencer, Y. Ziya, and S. J. Williamson. Electrical impedance tomography: induced-current imaging achieved with a multiple coil system. *IEEE Trans Biomed Eng*, 43(2):139–149, Feb 1996.
- [92] H. C. Pyo, O. Kwon, J. K. Seo, and E. J. Woo. Identification of current density distribution in electrically conducting subject with anisotropic conductivity distribution. *Phys Med Biol*, 50(13):3183–3196, Jul 2005.
- [93] J. K. Seo, J. R. Yoon, E. J. Woo, and O. Kwon. Reconstruction of conductivity and current density images using only one component of magnetic field measurements. *IEEE Trans Biomed Eng*, 50(9):1121–1124, Sep 2003.
- [94] H. Wen, J. Shah, and R. S. Balaban. Hall effect imaging. *IEEE Trans Biomed Eng*, 45(1):119–124, Jan 1998.
- [95] H. Wen and R. S. Balaban. The potential for hall effect breast imaging. *Breast Dis*, 10(3-4):191–195, Aug 1998.

- [96] U. Katscher, T. Dorniok, C. Findekleee, and P. Vernickel. In vivo determination of electric conductivity and permittivity using electric properties tomography (ept). In *Proc Intl Soc Mag Reson Med 15*, page 3034. ISMRM, 2007.
- [97] C. Findekleee, M. Hanft, U. Katscher, and P. Vernickel. Electric properties tomography (ept) via mri. In *Proc Intl Soc Mag Reson Med 14*, page 3037. ISMRM, 2006.
- [98] C. Findekleee, M. Hanft, U. Katscher, and P. Vernickel. Experimental verification of electric properties tomography (ept). In *Proc Intl Soc Mag Reson Med 14*, page 3035. ISMRM, 2006.
- [99] A. K. Sen and S. Torquato. Effective conductivity of anisotropic two-phase composite media. *Phys Rev B Condens Matter*, 39(7):4504–4515, Mar 1989.
- [100] P. B. Hoeltzell and R. W. Dykes. Conductivity in the somatosensory cortex of the cat – evidence for cortical anisotropy. *Brain Res*, 177(1):61–82, Nov 1979.
- [101] C. Nicholson and J. A. Freeman. Theory of current source-density analysis and determination of conductivity tensor for anuran cerebellum. *J Neurophysiol*, 38(2):356–368, Mar 1975.
- [102] S. H. Oh, S. Y. Lee, M. H. Cho, T.-S. Kim, and I. H. Kim. Electrical conductivity estimation from diffusion tensor and t2: A silk yarn phantom study. In *Proc Intl Soc Mag Reson Med 14*, page 3034, 2006.
- [103] M. Akhtari, N. Salamon, R. Duncan, I. Fried, and G. W. Mathern. Electrical conductivities of the freshly excised cerebral cortex in epilepsy surgery patients; correlation with pathology, seizure duration, and diffusion tensor imaging. *Brain Topogr*, 18(4):281–90, 2006.
- [104] J. G. Sled, A. P. Zijdenbos, and A. C. Evans. A nonparametric method for automatic correction of intensity nonuniformity in mri data. *IEEE Trans Med Imaging*, 17(1):87–97, Feb 1998.
- [105] J. Talairach and P. Tournoux. *Co planar stereotaxic atlas of the human brain : 3-dimensional proportional system: an approach to cerebral imaging*. Stuttgart ; New York : Thieme, 1988.
- [106] M. S. Atkins and B. T. Mackiewicz. Fully automatic segmentation of the brain in mri. *IEEE Trans Med Imaging*, 17(1):98–107, Feb 1998.

- [107] R. W. Cox. Afni: software for analysis and visualization of functional magnetic resonance neuroimages. *Comput Biomed Res*, 29(3):162–173, Jun 1996.
- [108] L. Lemieux, G. Hagemann, K. Krakow, and F. G. Woermann. Fast, accurate, and reproducible automatic segmentation of the brain in t1-weighted volume mri data. *Magn Reson Med*, 42(1):127–135, Jul 1999.
- [109] F. Ségonne, A. M. Dale, E. Busa, M. Glessner, D. Salat, H. K. Hahn, and B. Fischl. A hybrid approach to the skull stripping problem in mri. *Neuroimage*, 22(3):1060–1075, Jul 2004.
- [110] A. M. Dale, B. Fischl, and M. I. Sereno. Cortical surface-based analysis. i. segmentation and surface reconstruction. *Neuroimage*, 9(2):179–194, Feb 1999.
- [111] T. Kapur, W. E. Grimson, W. M. Wells, and R. Kikinis. Segmentation of brain tissue from magnetic resonance images. *Med Image Anal*, 1(2):109–127, Jun 1996.
- [112] S. M. Smith. Fast robust automated brain extraction. *Hum Brain Mapp*, 17(3):143–155, Nov 2002.
- [113] D. W. Shattuck and R. M. Leahy. Brainsuite: an automated cortical surface identification tool. *Med Image Anal*, 6(2):129–142, Jun 2002.
- [114] C. Xu, D. L. Pham, M. E. Rettmann, D. N. Yu, and J. L. Prince. Reconstruction of the human cerebral cortex from magnetic resonance images. *IEEE Trans Med Imaging*, 18(6):467–480, Jun 1999.
- [115] X. Zeng, L. H. Staib, R. T. Schultz, and J. S. Duncan. Segmentation and measurement of the cortex from 3-d mr images using coupled-surfaces propagation. *IEEE Trans Med Imaging*, 18(10):927–937, Oct 1999.
- [116] H. K. Hahn and H.-O. Peitgen. The skull stripping problem in mri solved by a single 3d watershed transform. In *MICCAI, Pittsburgh, PA, USA*, pages 134–143, 2000.
- [117] B. Fischl, D. H. Salat, E. Busa, M. Albert, M. Dieterich, C. Haselgrove, A. van der Kouwe, R. Killiany, D. Kennedy, S. Klaveness, A. Montillo, N. Makris, B. Rosen, and A. M. Dale. Whole brain segmentation: automated labeling of neuroanatomical structures in the human brain. *Neuron*, 33(3):341–355, Jan 2002.
- [118] D. L. Collins, P. Neelin, T. M. Peters, and A. C. Evans. Automatic 3d intersubject registration of mr volumetric data in standardized talairach space. *J Comput Assist Tomogr*, 18(2):192–205, 1994.

- [119] P. T. Fox, S. Mikiten, G. Davis, and J. Lancaster. *Functional neuroimaging*, chapter Brain map: a database of human functional brain mapping., pages 95–105. San Diego: Academic Press., 1994.
- [120] J. C. Mazziotta, A. W. Toga, A. Evans, P. Fox, and J. Lancaster. A probabilistic atlas of the human brain: theory and rationale for its development. the international consortium for brain mapping (icbm). *Neuroimage*, 2(2):89–101, Jun 1995.
- [121] P. M. Thompson, D. MacDonald, M. S. Mega, C. J. Holmes, A. C. Evans, and A. W. Toga. Detection and mapping of abnormal brain structure with a probabilistic atlas of cortical surfaces. *J Comput Assist Tomogr*, 21(4):567–581, 1997.
- [122] X. Han and B. Fischl. Atlas renormalization for improved brain mr image segmentation across scanner platforms. *IEEE Trans Med Imaging*, 26(4):479–486, Apr 2007.
- [123] N. Chauveau, X. Franceries, B. Doyon, B. Rigaud, J. P. Morucci, and P. Celsis. Effects of skull thickness, anisotropy, and inhomogeneity on forward eeg/erp computations using a spherical three-dimensional resistor mesh model. *Hum Brain Mapp*, 21(2):86–97, Feb 2004.
- [124] S. P. van den Broek, F. Reinders, M. Donderwinkel, and M. J. Peters. Volume conduction effects in eeg and meg. *Electroencephalogr Clin Neurophysiol*, 106(6):522–534, Jun 1998.
- [125] J. O. Ollikainen, M. Vauhkonen, P. A. Karjalainen, and J. P. Kaipio. Effects of local skull inhomogeneities on eeg source estimation. *Med Eng Phys*, 21(3):143–154, Apr 1999.
- [126] M. Jenkinson, M. Pechaud, and S. Smith. Bet2: Mr-based estimation of brain, skull and scalp surfaces. In *Eleventh Annual Meeting of the Organization for Human Brain Mapping*. Human Brain Mapping, 2005.
- [127] M. Pechaud, M. Jenkinson, and S. M. Smith. Bet2 - mri-based estimation of brain, skull and scalp surfaces. Technical report, Oxford University Center for Functional MRI of the brain (FMRIB), 2006.
- [128] D. C. Alexander, C. Pierpaoli, P. J. Basser, and J. C. Gee. Spatial transformations of diffusion tensor magnetic resonance images. *IEEE Trans Med Imaging*, 20(11):1131–9, 2001.

- [129] D. L. Camacho, R. H. Hopper, G. M. Lin, and B. S. Myers. An improved method for finite element mesh generation of geometrically complex structures with application to the skullbase. *J Biomech*, 30(10):1067–1070, Oct 1997.
- [130] C. H. Wolters, A. Anwander, G. Berti, and U. Hartmann. Geometry-adapted hexahedral meshes improve accuracy of finite-element-method-based eeg source analysis. *IEEE Trans Biomed Eng*, 54(8):1446–1453, Aug 2007.
- [131] J. Haueisen, C. Ramon, M. Eiselt, H. Brauer, and H. Nowak. Influence of tissue resistivities on neuromagnetic fields and electric potentials studied with a finite element model of the head. *IEEE Trans Biomed Eng*, 44(8):727–735, Aug 1997.
- [132] W. Andrae and H. Nowak, editors. *Magnetism in medicine - a handbook*. Wiley-VCH, Berlin Weinheim New York Chichester Brisbane Singapore Toronto, 1998.
- [133] U. Mitzdorf. Current source-density method and application in cat cerebral cortex: investigation of evoked potentials and eeg phenomena. *Physiol Rev*, 65(1):37–100, Jan 1985.
- [134] R. Plonsey and D. B. Heppner. Considerations of quasi-stationarity in electrophysiological systems. *Bull Math Biophys*, 29(4):657–664, Dec 1967.
- [135] J. Sarvas. Basic mathematical and electromagnetic concepts of the biomagnetic inverse problem. *Phys Med Biol*, 32(1):11–22, Jan 1987.
- [136] Jaakko Malmivuo and Robert Plonsey. *Bioelectromagnetism - Principles and Applications of Bioelectric and Biomagnetic Fields*. Oxford University Press, 1995.
- [137] C. H. Wolters, L. Grasedyck, and W. Hackbusch. Efficient computation of lead field bases and influence matrix for the fem-based eeg and meg inverse problem. *Inverse Problems*, 20:1099–1116, 2004.
- [138] J. Jin, editor. *The Finite Element Method in Electromagnetics*. Wiley, 1993.
- [139] D. Weinstein, L. Zhukov, and C. Johnson. Lead-field bases for electroencephalography source imaging. *Ann Biomed Eng*, 28(9):1059–1065, Sep 2000.
- [140] C. H. Wolters and A. Anwander. Neurofem, finite element software for fast computation of the forward solution in eeg/meg source localization, 2003-2007.
- [141] J. A. Nedler and R. Mead. A simplex method for function minimization. *Comput J (UK)*, 7:308–313, 1965.

- [142] J. Haueisen, D. S. Tuch, C. Ramon, P. H. Schimpf, V. J. Wedeen, J. S. George, and J. W. Belliveau. The influence of brain tissue anisotropy on human eeg and meg. *Neuroimage*, 15(1):159–166, Jan 2002.
- [143] G. Marin, C. Guerin, S. Baillet, L. Garnero, and G. Meunier. Influence of skull anisotropy for the forward and inverse problem in eeg: simulation studies using fem on realistic head models. *Hum Brain Mapp*, 6(4):250–269, 1998.
- [144] C. H. Wolters, A. Anwander, X. Tricoche, D. Weinstein, M. A. Koch, and R. S. MacLeod. Influence of tissue conductivity anisotropy on eeg/meg field and return current computation in a realistic head model: a simulation and visualization study using high-resolution finite element modeling. *Neuroimage*, 30(3):813–826, Apr 2006.
- [145] Statistical parametric mapping, August 2007. SPM2, <http://www.fil.ion.ucl.ac.uk/spm/spm2.html>.
- [146] M. Evans, N. Hastings, and B. Peacock, editors. *Statistical Distributions, 2nd edition*. Wiley, 1993.
- [147] K. A. Awada, D. R. Jackson, S. B. Baumann, J. T. Williams, D. R. Wilton, P. W. Fink, and B. R. Prasky. Effect of conductivity uncertainties and modeling errors on eeg source localization using a 2-d model. *IEEE Trans Biomed Eng*, 45(9):1135–1145, Sep 1998.
- [148] B. He, T. Musha, Y. Okamoto, S. Homma, Y. Nakajima, and T. Sato. Electric dipole tracing in the brain by means of the boundary element method and its accuracy. *IEEE Trans Biomed Eng*, 34(6):406–414, Jun 1987.
- [149] A. Anwander, C. H. Wolters, M. DümpeImann, and T. Knösche. Influence of realistic skull and white matter anisotropy on the inverse problem in eeg/meg-source localization. In *Int Conf Biomag*, pages 679–681, 2002.
- [150] C. H. Wolters, A. Anwander, X. Tricoche, S. Lew, and C. R. Johnson. Influence of local and remote white matter conductivity anisotropy for a thalamic source on eeg/meg field and return current computation. *Int J Bioelectromagnetism*, 7(1):203–206, May 2005.
- [151] M. Liehr and J. Haueisen. Experimentally observed influence of anisotropic compartments in a volume conductor on the magnetic field distribution generated by artificial current dipoles. *Int J Bioelectromagnetism*, 7(1):131, May 2005.

- [152] H. Hallez, B. Vanrumste, P. V. Hese, Y. D’Asseler, I. Lemahieu, and R. V. de Walle. A finite difference method with reciprocity used to incorporate anisotropy in electroencephalogram dipole source localization. *Phys Med Biol*, 50(16):3787–3806, Aug 2005.
- [153] H. J. Gould. Body surface maps in the somatosensory cortex of rabbit. *J Comp Neurol*, 243(2):207–233, Jan 1986.
- [154] P. Wen. The impact of inhomogeneous tissue anisotropy on potential distribution within head model. *Australas Phys Eng Sci Med*, 26(3):115–118, Sep 2003.
- [155] C. H. Wolters, A. Anwander, B. Maess, R. S. Macleod, and A. D. Friederici. The influence of volume conduction effects on the eeg/meg reconstruction of the sources of the early left anterior negativity. *Conf Proc IEEE Eng Med Biol Soc*, 5:3569–3572, 2004.
- [156] J. Li, K. Wang, S. Zhu, and B. He. Effects of holes on eeg forward solutions using a realistic geometry head model. *J Neural Eng*, 4(3):197–204, Sep 2007.
- [157] C. G. Bénar and J. Gotman. Modeling of post-surgical brain and skull defects in the eeg inverse problem with the boundary element method. *Clin Neurophysiol*, 113(1):48–56, Jan 2002.
- [158] C. Ramon, P. H. Schimpf, and J. Haueisen. Influence of head models on eeg simulations and inverse source localizations. *Biomed Eng Online*, 5:10, 2006.
- [159] N. G. Gençer and C. E. Acar. Sensitivity of eeg and meg measurements to tissue conductivity. *Phys Med Biol*, 49(5):701–717, Mar 2004.
- [160] R. V. Uitert, C. Johnson, and L. Zhukov. Influence of head tissue conductivity in forward and inverse magnetoencephalographic simulations using realistic head models. *IEEE Trans Biomed Eng*, 51(12):2129–2137, Dec 2004.
- [161] B. N. Cuffin. Effects of modeling errors and eeg measurement montage on source localization accuracy. *J Clin Neurophysiol*, 18(1):37–44, Jan 2001.
- [162] B. Yvert, O. Bertrand, M. Thévenet, J. F. Echallier, and J. Pernier. A systematic evaluation of the spherical model accuracy in eeg dipole localization. *Electroencephalogr Clin Neurophysiol*, 102(5):452–459, May 1997.
- [163] B. Vanrumste, G. V. Hoey, R. V. de Walle, M. R. P. D’Havé, I. A. Lemahieu, and P. A. J. M. Boon. Comparison of performance of spherical and realistic head models in dipole localization from noisy eeg. *Med Eng Phys*, 24(6):403–418, Jul 2002.

- [164] A. Crouzeix, B. Yvert, O. Bertrand, and J. Pernier. An evaluation of dipole reconstruction accuracy with spherical and realistic head models in meg. *Clin Neurophysiol*, 110(12):2176–2188, Dec 1999.
- [165] M. De Lucia, G. J M Parker, K. Embleton, J. M. Newton, and V. Walsh. Diffusion tensor mri-based estimation of the influence of brain tissue anisotropy on the effects of transcranial magnetic stimulation. *Neuroimage*, 36(4):1159–1170, Jul 2007.
- [166] C. R. Butson, S. E. Cooper, J. M. Henderson, and C. C. McIntyre. Predicting the effects of deep brain stimulation with diffusion tensor based electric field models. *Int Conf Med Image Comput Assist Interv*, 9(Pt 2):429–437, 2006.
- [167] C. R. Butson, S. E. Cooper, J. M. Henderson, and C. C. McIntyre. Patient-specific analysis of the volume of tissue activated during deep brain stimulation. *Neuroimage*, 34(2):661–670, Jan 2007.
- [168] C. C. McIntyre, S. Mori, D. L. Sherman, N. V. Thakor, and J. L. Vitek. Electric field and stimulating influence generated by deep brain stimulation of the subthalamic nucleus. *Clin Neurophysiol*, 115(3):589–595, Mar 2004.
- [169] C. Ramon, P. Schimpf, Y. Wang, J. Haueisen, and A. Ishimaru. The effect of volume currents due to myocardial anisotropy on body surface potentials. *Phys Med Biol*, 47(7):1167–1184, Apr 2002.
- [170] D. Wei, O. Okazaki, and K. Harumi. Comparison of body surface potential maps simulated with isotropic and anisotropic computer heart models. *J Electrocardiol*, 28(4):346–347, Oct 1995.
- [171] C. Ramon, Y. Wang, J. Haueisen, P. Schimpf, S. Jaruvatanadilok, and A. Ishimaru. Effect of myocardial anisotropy on the torso current flow patterns, potentials and magnetic fields. *Phys Med Biol*, 45(5):1141–1150, May 2000.
- [172] M. Thivierge, R. M. Gulrajani, and P. Savard. Effects of rotational myocardial anisotropy in forward potential computations with equivalent heart dipoles. *Ann Biomed Eng*, 25(3):477–498, 1997.
- [173] P. Helm, M. F. Beg, M. I. Miller, and R. L Winslow. Measuring and mapping cardiac fiber and laminar architecture using diffusion tensor mr imaging. *Ann N Y Acad Sci*, 1047:296–307, Jun 2005.
- [174] J. Dou, T. G. Reese, W.-Y. I. Tseng, and V. J. Wedeen. Cardiac diffusion mri without motion effects. *Magn Reson Med*, 48(1):105–114, Jul 2002.

- [175] B. N. Cuffin, D. Cohen, K. Yunokuchi, R. Maniewski, C. Purcell, G. R. Cosgrove, J. Ives, J. Kennedy, and D. Schomer. Tests of eeg localization accuracy using implanted sources in the human brain. *Ann Neurol*, 29(2):132–138, Feb 1991.
- [176] T. Krings, K. H. Chiappa, B. N. Cuffin, J. I. Cochius, S. Connolly, and G. R. Cosgrove. Accuracy of eeg dipole source localization using implanted sources in the human brain. *Clin Neurophysiol*, 110(1):106–114, Jan 1999.
- [177] B. N. Cuffin, D. L. Schomer, J. R. Ives, and H. Blume. Experimental tests of eeg source localization accuracy in spherical head models. *Clin Neurophysiol*, 112(1):46–51, Jan 2001.
- [178] M. Liehr and J. Haueisen. Influence of anisotropic compartments on magnetic field and electric potential distributions generated by artificial current dipoles inside a torso phantom. *Phys Med Biol*, 53(1):245–254, Jan 2008.
- [179] T. Yoshida, K. Shiga, K. Yoshikawa, K. Yamada, and M. Nakagawa. White matter loss in the splenium of the corpus callosum in a case of posterior cortical atrophy: a diffusion tensor imaging study. *Eur Neurol*, 52(2):77–81, 2004.
- [180] O. Naggara, C. Oppenheim, D. Rieu, N. Raoux, S. Rodrigo, G. D. Barba, and J.-F. Meder. Diffusion tensor imaging in early alzheimer’s disease. *Psychiatry Res*, 146(3):243–249, Apr 2006.
- [181] D. J. Werring, C. A. Clark, G. J. Barker, A. J. Thompson, and D. H. Miller. Diffusion tensor imaging of lesions and normal-appearing white matter in multiple sclerosis. *Neurology*, 52(8):1626–1632, May 1999.
- [182] R. Bammer, M. Augustin, S. Strasser-Fuchs, T. Seifert, P. Kapeller, R. Stollberger, F. Ebner, H. P. Hartung, and F. Fazekas. Magnetic resonance diffusion tensor imaging for characterizing diffuse and focal white matter abnormalities in multiple sclerosis. *Magn Reson Med*, 44(4):583–591, Oct 2000.
- [183] M. Filippi, M. Cercignani, M. Inglese, M. A. Horsfield, and G. Comi. Diffusion tensor magnetic resonance imaging in multiple sclerosis. *Neurology*, 56(3):304–311, Feb 2001.
- [184] R. G. M. Schlösser, I. Nenadic, G. Wagner, D. Güllmar, K. von Consbruch, S. Köhler, C. C. Schultz, K. Koch, C. Fitzek, P. M. Matthews, J. R. Reichenbach, and H. Sauer. White matter abnormalities and brain activation in schizophrenia: a combined dti and fmri study. *Schizophr Res*, 89(1-3):1–11, Jan 2007.

- [185] H.-J. Park, J. S. Kwon, T. Youn, J. S. Pae, J.-J. Kim, M.-S. Kim, and K.-S. Ha. Statistical parametric mapping of loreta using high density eeg and individual mri: application to mismatch negativities in schizophrenia. *Hum Brain Mapp*, 17(3):168–178, Nov 2002.
- [186] T. Youn, H.-J. Park, J.-J. Kim, M. S. Kim, and J. S. Kwon. Altered hemispheric asymmetry and positive symptoms in schizophrenia: equivalent current dipole of auditory mismatch negativity. *Schizophr Res*, 59(2-3):253–260, Feb 2003.

List of Tables

2.1.	Comparison of measured self-diffusion coefficients	30
2.2.	Calculated diagonal b -matrix elements	34
2.3.	Diffusion gradient amplitudes definition for circ. sampling	36
2.4.	Mean DT of a water phantom derived using different b -matrices.	45
3.1.	Tissue conductivities taken from literature	59
4.1.	Threshold values corresponding to the 0.8 percentile used in Fig. 4.11 .	92
4.2.	Conductivities of white matter used in the human study	97
4.3.	RDM and MAG values of the 5th, 50th and 95th percentile from the density distributions for the different anisotropic models	103
4.4.	5th, 50th and 95th percentile of the logarithmized MAG values for the different models. The fourth line within each modality shows the amount of dipoles in percent which generate a lower magnitude in the anisotropic models compared to the solution in the isotropic model.	104
4.5.	Values of dipole shift, magnitude change and orientation change from the 5th, 50th and 95th percentile of the density distributions for the different anisotropic models	109
4.6.	5th, 50th and 95th percentile of the logarithmized magnitude changes for the different anisotropic models. The fourth line within each modality shows the amount dipoles in percent which generate a lower magnitude in the anisotropic models compared to the solution in the isotropic model.110	
A.1.	Translation of Freesurfer to Simbio IDs	I

List of Figures

1.1. Edwin Smith Papyrus	3
1.2. Cover picture of Vesalius' <i>De humani corporis fabrica</i>	4
1.3. Orthogonal slices of the human head	6
1.4. Golgi stained pyramidal neuron	7
1.5. EEG registration by Hans Berger from 1928	9
1.6. Illustration of the international 10-20 system	10
1.7. Conductivity head models	13
1.8. T1, T2 and PD weighted axial MR images	14
2.1. Nuclear spin causing the particle to behave like a tiny magnet.	17
2.2. Randomly distributed spins with zero total magnetic moment.	18
2.3. Spins aligned parallel or anti-parallel with the external magnetic field. .	18
2.4. Net macroscopic magnetization	19
2.5. RF pulse applied through a rotating reference frame causing the net macroscopic.	20
2.6. Schematics of PGSE sequence	24
2.7. Signal attenuation of several liquids measured at different b-values. . .	29
2.8. Sampling scheme.	35
2.9. Simulated b-matrix calculation error maps over a spherical surface . . .	37
2.10. Diffusion weighted images for 24 sampling directions	38
2.11. b-matrix calculation - comparison of simulated data with measured data	39
2.12. Decomposition of the signal according to Neeman	41
2.13. Contour maps of estimated diffusion coefficients	44
2.14. Standard deviation maps of diagonal tensor elements from Siemens Vi- sion MR-Tomograph	46
2.15. Plot of fitted k-parameter for every series over field of view and slice thickness for the series acquired on a Siemens Magnetom Vision	47
2.16. Standard deviation maps of diagonal tensor elements from Siemens Sonata MR-Tomograph	48
2.17. Plot - k-parameters	48
2.18. Timing diagram of the diffusion weighted TSRE sequence	51

2.19. The effect of parallel image acquisition in echo planar imaging sequences	52
2.20. Ellipsoidal representation of the diffusion tensor	55
2.21. Scalar measured of diffusion tensor data	56
3.1. Relationship between conductivity and diffusion tensor eigenvalues . . .	63
3.2. Segmentation steps using a T1w data set	68
3.3. Result of the coregistration of a FA map volume to a T1w volume . . .	69
3.4. FEM grids with and without node shift	71
4.1. Schematic for inverse the inverse problem	73
4.2. Setup for FEM animal study	79
4.3. Schematic view of the positioning of the artificial anisotropic cube - animal study	82
4.4. ECoG Recordings from animal model	83
4.5. Animal study I - forward analysis - mapping	85
4.6. Animal study II - forward results - mapping	86
4.7. Animal study I - inverse analysis - mapping	88
4.8. Animal study II - inverse analysis - mapping	89
4.9. Results in animal model - influence of dipole distance with respect to anisotropic tissue in an animal model	89
4.10. Results from animal study - influence of dipole orientation with respect to anisotropic tissue	90
4.11. Visualization of regions of strong influence - animal study	91
4.12. Animal study - results of the source localization from measurements . .	92
4.13. Coronal slice: T1, segmented and with coregistered DTI	96
4.14. High resolution FE volume conductor model	98
4.15. EEG/MEG setup for the human head FEM study	99
4.16. Positioning of the dipoles in cortex used in the human simulation study	100
4.17. RDM and MAG density plots	102
4.18. Human study - EEG - log(MAG)	104
4.19. Human study - EEG - mapping forward results	105
4.20. Human study - MEG - mapping forward results	106
4.21. Human study - inverse analysis - density functions	108
4.22. Human study - inverse analysis - log(magnitude change)	110
4.23. Human study - EEG - mapping inverse results	111
4.24. Human study - MEG - mapping inverse results	112
4.25. Dipole shift human EEG study - coronar view	114
4.26. Dipole shift human MEG study - coronar view	115

A. Appendix

Tab. A.1.: Translation of subcortical brain segment ID's used by Freesurfer software packages to the reduced number of segment ID's of the Simbio software package. Un-listed Freesurfer Ids are omitted by the translation. The Simbio ID's encode as follows: 0=background, 6=white matter, 7=gray matter, 8=CSF, 9=cortical ribbon (gets the same conductivity as segments with Id 7).

Label	Freesurfer ID	Simbio ID
Unknown	0	0
Left-Cerebral-White-Matter	2	6
Left-Cerebral-Cortex	3	9
Left-Lateral-Ventricle	4	8
Left-Inf-Lat-Vent	5	8
Left-Cerebellum-White-Matter	7	6
Left-Cerebellum-Cortex	8	7
Left-Thalamus	9	7
Left-Thalamus-Proper	10	6
Left-Caudate	11	7
Left-Putamen	12	7
Left-Pallidum	13	7
3rd-Ventricle	14	8
4th-Ventricle	15	8
Brain-Stem	16	6
Left-Hippocampus	17	7
Left-Amygdala	18	7
Left-Insula	19	7
Left-Operculum	20	7
CSF	24	8
Left-Accumbens-area	26	6
Left-Substantia-Nigra	27	7
Left-VentralDC	28	6
Right-Cerebral-White-Matter	41	6
Right-Cerebral-Cortex	42	9
Right-Lateral-Ventricle	43	8
Right-Inf-Lat-Vent	44	8

A. Appendix

Label	Freesurfer ID	Simbio ID
Right-Cerebellum-White-Matter	46	6
Right-Cerebellum-Cortex	47	7
Right-Thalamus	48	7
Right-Thalamus-Proper	49	6
Right-Caudate	50	7
Right-Putamen	51	7
Right-Pallidum	52	7
Right-Hippocampus	53	7
Right-Amygdala	54	7
Right-Insula	55	7
Right-Operculum	56	7
Right-Accumbens-area	58	6
Right-Substantia-Nigra	59	7
Right-VentralDC	60	6
5th-Ventricle	72	8
Left-Lateral-Ventricles	75	8
Right-Lateral-Ventricles	76	8
WM-hypointensities	77	6
Left-WM-hypointensities	78	6
Right-WM-hypointensities	79	6
Left-non-WM-hypointensities	81	6
Right-non-WM-hypointensities	82	6
Optic-Chiasm	85	6
Corpus-Callosum	86	6
Left-Amygdala-Anterior	96	7
Right-Amygdala-Anterior	97	7
CSF-SA	122	8
Spinal-Cord	126	6
Left-Caudate/Putamen	136	7
Right-Caudate/Putamen	137	7
Left-Clastrum	138	7
Right-Clastrum	139	7
alveus	201	6
perforant-pathway	202	6
parasubiculum	203	7
presubiculum	204	7
subiculum	205	7
CA1	206	7
CA2	207	7
CA3	208	7

Label	Freesurfer ID	Simbio ID
CA4	209	7
molecular-layer-subiculum	212	7
lateral-ventricle	213	8
entorhinal-cortex	216	7
Amygdala	218	7
Cerebral-White-Matter	219	6
Cerebral-Cortex	220	7
Inf-Lat-Vent	221	8

Curriculum Vitae

Name	Daniel Güllmar
Date of birth	10. July 1976
Place of birth	Sondershausen
Marital status	single
Citizenship	German

EDUCATION

1/2002 - present	PhD research: “ <i>Anisotropic EEG/MEG volume conductor modeling based on Diffusions Tensor Imaging</i> ”, Medical Physics Group, Friedrich Schiller University Jena, Germany
04/2001 - 12/2001	diploma thesis: “ <i>Sprachcodierung</i> ”, ABS GmbH, Jena, Germany
10/1996 - 12/2001	graduate engineer in media technology (Dipl.Ing.), Technical University Ilmenau, Germany
09/1991 - 07/1995	high school graduation, Gymnasium Salzmann-Schule Schnepfenthal, Germany.

EXPERIENCE

08/2005 - 04/2006	internship, Martinos Center for Biomedical Imaging, Charlestown, MA, USA
10/1999 - 02/2000	internship, T.E.I. of Crete, Branch of Chania, Greece
08/1998 - 02/2001	student research assistant in Media Technology, Technical University Ilmenau, Germany

AWARDS

05/2007	“Poster Award in the Diffusion, Perfusion - Neuro Category” for the work “ <i>Influence of anisotropic conductivity measured using DTI on the EEG forward solution: a whole human head sensitivity analysis</i> ”, conferred on the 15. ISMRM-ESMRMB Joint Annual, Berlin, Germany, 19-25 May, 2007
09/2003	“Vortragspreis”, for the work “ <i>Beschränkte Diffusion zur quantitativen Analyse von Mikrostrukturen</i> ”, conferred on the Dreiländertagung der Gesellschaft für Biomedizinische Technik, Salzburg, Austria, 25. -28. September 2003

MEMBERSHIPS

since 12/2003	International Society for Magnetic Resonance in Medicine (ISMRM)
since 4/2004	German Chapter of the ISMRM (DS-ISMRM)

Publications

Papers

S. Böhr, **D. Güllmar**, R. Knab, J.R. Reichenbach, O.W. Witte, J. Haueisen: “*Fractional anisotropy correlates with auditory simple reaction time performance.*”, Brain Res, 2007, 1186:194-202

R.G. Schlösser, I. Nenadic, G. Wagner, **D. Güllmar**, K. von Consbruch, S. Köhler, C.C. Schultz, K. Koch, C. Fitzek, P.M. Matthews, J.R. Reichenbach, H. Sauer: “*White matter abnormalities and brain activation in schizophrenia: a combined DTI and fMRI study.*”, Schizophr Res. 2007 Jan ; 89(1-3):1-11

D. Güllmar, J. Haueisen, M. Eiselt, F. Giessler, L. Flemming, A. Anwander, T.R. Knösche, C.H. Wolters, M. Dümpelmann, D.S. Tuch, J.R. Reichenbach: “*Influence of anisotropic conductivity on EEG source reconstruction: investigations in a rabbit model.*”, IEEE Trans Biomed Eng. 2006 Sep ; 53(9):1841-50

H.J. Mentzel, D. Karadag, **D. Güllmar**, U. Löbel, J.R. Reichenbach, J. Sedlacik, J. Seidel, U. Brandl: “*Unidentified bright objects in neurofibromatosis type 1: Results of diffusion tensor imaging in children and adolescents*”, Journal of Pediatric Neurology, 2006, 4(1):27-31,

D. Güllmar, J. R. Reichenbach, A. Anwander, T. Knösche, C. H. Wolters, M. Eiselt, J. Haueisen: “*Influence of anisotropic conductivity of the white matter tissue on EEG source reconstruction – a FEM simulation study*”, Int Journal of Bioelectromagnetism, 2005, 7(1):108-9

D. Karadag, H.J.Mentzel, **D. Güllmar**, T. Rating, U. Löbel, U. Brandl, J.R. Reichenbach, W.A. Kaiser: “*Diffusion tensor imaging in children and adolescents with tuberous sclerosis*”. Pediatr Radiol, 2005, 35(10):980-3

D. Güllmar, J. Haueisen, J.R. Reichenbach: “*Analysis of b-value calculations in diffusion weighted and diffusion tensor imaging*”. Concepts in magnetic resonance, 2005, 25A(1):53-66

Conference Abstracts

D. Güllmar , J.R. Reichenbach, J. Haueisen, “*The sensitivity of the EEG and MEG forward solution to anisotropic conductivity - a whole human head simulation study*”, Biomag 2008, Sapporo, Japan

D. Güllmar , J. Langner, J. Haueisen, J.R. Reichenbach, “*Combination of distance measures for optimal fiber clustering in diffusion tensor imaging*”, ISMRM 2008, Toronto, Ontario, Canada

D. Güllmar, A. Deistung, S. Richter, J. Haueisen, J.R. Reichenbach, “*Tracking of CE-MR-Angiography data using established approaches in DTI*”, ISMRM 2008, Toronto, Ontario,

Canada

D. Güllmar, J.R. Reichenbach, J. Haueisen, “*Influence of anisotropic conductivity on the EEG forward and inverse solution*”, NFSI 2007, Hangzhou, China

D. Güllmar, J. Haueisen, J.R. Reichenbach, “*Influence of anisotropic conductivity measured using DTI on the EEG forward solution: a whole human head sensitivity analysis*”, ISMRM 2007, Berlin, German

D. Güllmar, S. Böhr, J. Haueisen, O.W. Witte, W.A. Kaiser, J.R. Reichenbach, “*Correlation of auditory simple reaction task (aSRT) performance with fractional anisotropy (FA)*”, ECR 2007, Vienna, Austria

D. Güllmar, J.R. Reichenbach, A. Anwander, C.H. Wolters, J. Haueisen, “*From DTI to CTI: The role of anisotropic conductivity of the white matter tissue - an EEG FEM simulation study*”, ISMRM 2006, Seattle (WA), USA

D. Güllmar, S. Böhr, R. Knab, J. Haueisen, J.R. Reichenbach, O.W. Witte, “*Correlation of auditory simple reaction task (aSRT) performance with fractional anisotropy (FA)*”, HBM 2006, Florenz, Italy

D. Gräbel, H. Axer, **D. Güllmar**, J.R. Reichenbach, “*Mathematische Beschreibung des Kontrastverlaufs diffusionsgewichteter MR-Bildgebung während der ersten vier Monate nach einem Hirnstamminfarkt*”, DSISMRM 2006, Jena, Germany

D. Güllmar, J.R. Reichenbach, J. Haueisen, “*Anisotropic Conductivity in EEG source reconstruction - a FEM simulation study*”, Biomedizinische Technik: Proceedings of the jointly held Congress ICMP and BMT, volume 50 (Suppl.1), p1430, 14.9. - 17.9.2005, Nürnberg, Germany

I. Nenadic, G. Wagner, S. Köhler, E. Sinsel, **D. Güllmar**, C. Fitzek, J.R. Reichenbach, H. Sauer, R. Schlösser, “*How structure determines function in schizophrenia: A combined DTI and fMRI study*”, 11th Annual Meeting of the Organization for Human Brain Mapping, p21, 12. - 16. Juni, 2005, Toronto, Ontario, Canada

D. Güllmar, J.R. Reichenbach, A. Anwander, T.R. Knösche, C.H. Wolters, J. Haueisen, “*Influence of anisotropic conductivity of the white matter tissue on EEG source reconstruction - a FEM simulation study*”, 5th International Symposium on Noninvasive Functional Source Imaging, p108-110, 12. - 15.5.2005, Minneapolis (MN), USA

D. Güllmar, J.R. Reichenbach, L. Flemming, M. Eiselt, A. Anwander, J. Haueisen, T.R. Knösche, C.H. Wolters, “*Conductivity measured by DTI: Influence on EEG source localization evaluated in a FEM model of an animal head*”, Proc. of the International Society For Magnetic Resonance in Medicine, 13th Scientific Meeting and Exhibition, p270, 7.-13. Mai 2005, Miami Beach (FL), USA

U. Löbel, **D. Güllmar**, H.-J. Mentzel, J. Sedlacik, J.R. Reichenbach, W.A. Kaiser, “*Dif-*

fusion Tensor Imaging of Healthy Neonates and Children Up to Adolescence”, Proc. of the International Society For Magnetic Resonance in Medicine, 13th Scientific Meeting and Exhibition, p253, 7.-13. Mai 2005, Miami Beach (FL), USA

U. Löbel, **D. Güllmar**, H.-J. Mentzel, J. Sedlacik, J.R. Reichenbach, P. Stoeter, W.A. Kaiser: Diffusion Tensor Imaging gesunder Neugeborener, Kinder und Jugendlicher p S201, 86. Deutscher Röntgenkongress, 4. - 7. Mai 2005, Berlin, Germany

U. Löbel, **D. Güllmar**, H.-J. Mentzel, J. Sedlacik, J.R. Reichenbach, W.A. Kaiser: Diffusion tensor imaging of healthy neonates and children up to adolescence p 280, European Congress of Radiology, 4. - 8.März 2005, Wien, Austria

D. Güllmar, J.R. Reichenbach, J. Haueisen, “*b-Matrix assesment in Diffusion Tensor Imaging using a reference phantom*”, ECR 2005, p340, Vienna, Austria

H.-J. Mentzel, **D. Güllmar**, A. Rauscher, U. Löbel, J. Sedlacik, D. Karadag, U. Brandl, J.R. Reichenbach, W.A. Kaiser: Neue MR-Verfahren in der Hirndiagnostik, Jahrestagung der Sächsisch-Thüringischen Gesellschaft für Kinder- und Jugendmedizin, 8. - 9. April 2005, Leipzig, Germany

J.R. Reichenbach, **D. Güllmar**, J. Haueisen, “*Experimental Assesment of the b-Matrix Using a Reference Phantom in Diffusion Tensor Imaging*”, DGKN 2004, Jena, Germany

D. Güllmar, J.R. Reichenbach, M. Eiselt, J. Haueisen, “*The influence of anisotropic conductivity on the EEG source localization investigated with a FEM volume conductor of an animal model*”, DGKN 2004, Jena, Germany

D. Güllmar, J. Haueisen, J.R. Reichenbach, “*Assesment of the variance of the principal direction in Diffusion Tensor Imaging*”, DGBMT 2004, Ilmenau, Germany

J. Haueisen, **D. Güllmar**, J.R. Reichenbach, P. Schimpf, C. Ramon, “*Anisotropic conductivity influences EEG/MEG source reconstruction.*”, Proceedings of the 14th International Conference on Biomagnetism, BIOMAG 2004, Boston, MA, USA

D. Güllmar, J. Haueisen, W.A. Kaiser, J.R. Reichenbach, “*Uncertainty Maps in Diffusion Tensor Imaging*”, ECR 2004, Vienna, Austria

J. Haueisen, **D. Güllmar**, L. Flemming, M. Eiselt, J.R. Reichenbach, A. Anwander, M. Dümpelmann, T. Knösche, and C.H. Wolters, “*Validation of the new SimBio Electromagnetic Source Localization Environment in an Animal Model.*”, 14th Conf. of the Int. Soc. for Brain Electromag. Top., ISBET 2003, Santa Fe, NM, USA

D. Güllmar, J. Haueisen, J.R. Reichenbach, “*In vitro Untersuchungen zur beschränkten Diffusion mit Hilfe der diffusionsgewichteten MR-Bildgebung*”, DGMP 2003, Heidelberg, Germany

D. Güllmar, L. Flemming, A. Anwander, M. Dümpelmann, T.R. Knösche, M. Eiselt,

J.R. Reichenbach, J. Haueisen, “*Comparison of the boundary element method and the finite element method in ECoG/MEG source localization in an animal model*”, NFSI 2003, Chieti, Italy

D. Güllmar, J. Haueisen, J.R. Reichenbach, “*Beschränkte Diffusion zur quantitativen Analyse von Mikrostrukturen*”, BMT 2003, Salzburg, Austria

D. Güllmar, J. Haueisen, J.R. Reichenbach, “*Optimierte Methoden zur Diffusionstensorbestimmung - Validierung am isotropen Medium*”, Röko 2003, Wiesbaden, Germany

D. Güllmar, J. Haueisen, J.R. Reichenbach, “*Investigation of techniques to optimize diffusion tensor elements using isotropic media*”, ECR 2003, Vienna, Austria

D. Güllmar, J. Haueisen, J.R. Reichenbach, “*Optimales Applikationsschema für DTI-Messungen*”, 5. Jahrestagung der DSISMRM, Book of abstracts 5, 2002, Hamburg, Germany

D. Güllmar, T. Jaap, M.E. Bellemann, J. Haueisen, J.R. Reichenbach, “*DTI Measurements of Isotropic and Anisotropic Media*”. Biomed Tech (Berl). 2002;47 Suppl 1 Pt 1:420-2

D. Güllmar, T. Jaap, M.E. Bellemann, J. Haueisen, J.R. Reichenbach, “*Investigation and Validation of Diffusion Tensor Imaging Using Model Substances*”. Proceedings of the 13th International Conference on Biomagnetism August 10-14, 2002; Jena, Germany

Invited Talks

DTI and its application to volume conductor modeling for EEG/MEG source localization, EU-COST Final Meeting, Dundee, Great Britain, 24.01.2008

Anisotrope Volumenleitermodellierung zur Verbesserung der EEG/MEG Quellenlokalisation, Medizin-Physik-Seminar WS 2007/2008, DKFZ Heidelberg, Heidelberg, Germany, 16.01.2008

Anisotropic EEG/MEG volume conductor modeling based on Diffusion Tensor Imaging, Forschungsseminar am Institut für Biomedizinische Technik und Informatik der TU-Ilmenau, Ilmenau, Germany, 21.11.2007

Diffusion Tensor Imaging, Strahlentherapie des Universitätsklinikums Jena, Jena, Germany, 11.09.2007

Conductivity Tensor Mapping of the human brain using diffusion tensor MRI, 2nd International Summer School in Biomedical Engineering, Schönburg, Germany, 13.08.2007

Anisotrope Leitfähigkeitsmodelle mit Hilfe von Diffusions Tensor Imaging zur Verbesserung der Quellenlokalisation bei EEG/MEG Experimenten, Kolloquium Biologisch und Klinische Psychologie, Jena, Germany, 23.11.2006

Anisotrope Leitfähigkeitsmodelle mit Hilfe von Diffusions Tensor Imaging, Arbeitskreis der

Deutschen Gesellschaft für Medizinische Physik, Jena, Germany, 11.10.2006

Evaluation of Source Localization WP 7.1, Final Meeting of Simbio EU-Project, Amiens, France, 30.10.2002

Danksagung

Die vorliegende Dissertation wäre nicht zustande gekommen, wenn ich nicht breite Unterstützung und Hilfe gehabt hätte. An erster Stelle sei Professor Jens Haueisen und Prof. Jürgen Reichenbach herzlichst gedankt für die Übernahme und Betreuung meiner thematischen Fragestellung. Beide haben mich in der Gesamtlaufzeit intensiv betreut, standen immer für Diskussionen zur Verfügung und haben damit einen großen Anteil an meinem wissenschaftlichen Werdegang. In den Arbeitsgruppen von Prof. Haueisen, dem Biomagnetischen Zentrum, und von Prof. Reichenbach, der Arbeitsgruppe Medizinische Physik, habe ich mich stets wohl gefühlt und die Gemeinschaft beider Gruppen haben einen großen Rückhalt bei der wissenschaftlichen Arbeit gegeben. Allen Mitarbeitern sei damit ein großer Dank ausgesprochen.

Des Weiteren möchte ich mich beim Interdisziplinären Zentrum für Klinische Forschung (IZKF) Jena für die finanzielle Unterstützung in den Teilprojekten 1.12 (2001-2004) und 1.8 (2004-2007) bedanken in denen der Großteil der Arbeit entstanden ist. Zusätzlich wurde mir durch das IZKF ein Forschungsaufenthalt am Martinos Center for Biomedical Imaging (Charlestown, MA, USA - 08/2005-04/2006) ermöglicht. Für die Betreuung während dieses Aufenthaltes durch David S. Tuch, PhD möchte ich mich hiermit ebenfalls bedanken. Mein Dank gilt an dieser Stelle auch Thomas Witzel und Matti S. Hamalainen, PhD, die es mir ermöglichten, auch nach meinem Aufenthalt die rechentechnische Infrastruktur am Martinos Center für weitere Simulationen nutzen zu können.

Neben der Unterstützung in naturwissenschaftlichen und ingenieurwissenschaftlichen Fragen, habe ich auch einen sehr guten Einblick in die medizinische Arbeit am Universitätsklinikum Jena bekommen, explizit in der MRT Abteilung des Instituts für Diagnostische und Interventionelle Radiologie. Dem ärztlichen, insbesondere PD Dr. med. Hans-Joachim Mentzel, und medizin-technischem Personal, insbesondere Ines Krumbein, möchte ich daher einen herzlichen Dank aussprechen, vor allem für die Bereitschaft zur Klärung medizinischer Fragen und der technischen Umsetzung von MR Aufnahmen.

Ebenso sei allen denen ein Dankeschön ausgesprochen, die nicht namentlich Erwähnung fanden, aber zum Gelingen dieser Arbeit beigetragen haben. Auf keinen Fall möchte ich aber versäumen meinen Eltern und Großeltern zu danken. Sie haben nicht nur in finanzieller Hinsicht mein Studium ermöglicht, sondern mir in jeder Phase des Studiums und während des Verfassens der Doktorarbeit einen starken Rückhalt gegeben. Nicht zuletzt gilt mein Dank auch meiner Freundin Susanne, die mich besonders in der letzten Phase der Arbeit moralisch unterstützte und auf viele gemeinsame Stunden verzichten musste.

Erklärung

Ich versichere, dass ich die vorliegende Arbeit ohne unzulässige Hilfe Dritter und ohne Benutzung anderer als der angegebenen Hilfsmittel angefertigt habe. Die aus anderen Quellen direkt oder indirekt übernommenen Daten und Konzepte sind unter Angabe der Quelle gekennzeichnet.

An der inhaltlich-materiellen Erstellung der vorliegenden Arbeit waren keine weiteren Personen beteiligt. Insbesondere habe ich hierfür nicht die entgeltliche Hilfe von Vermittlungs- bzw. Beratungsdiensten (Promotionsberater oder anderer Personen) in Anspruch genommen. Niemand hat von mir unmittelbar oder mittelbar geldwerte Leistungen für Arbeiten erhalten, die im Zusammenhang mit dem Inhalte der vorgelegten Dissertation stehen.

Die Arbeit wurde bisher weder im In- noch im Ausland in gleicher oder ähnlicher Form einer Prüfungsbehörde vorgelegt.

Ich bin darauf hingewiesen worden, dass die Unrichtigkeit der vorstehenden Erklärung als Täuschungsversuch angesehen wird und den erfolglosen Abbruch des Promotionsverfahrens zu Folge hat.

(Ort, Datum)

(Unterschrift)

Thesen zur Dissertation
Anisotropic EEG/MEG volume conductor modeling
based on Diffusion Tensor Imaging

Dipl.-Ing. Daniel Güllmar

- Die exakte analytische Berechnung der b-Matrix erhöht die Genauigkeit der zu berechnenden Diffusionstensoren und vermeidet damit einen systematischen Fehler.
- Liegen keine Informationen für die Berechnung der exakten b-Matrix unter Einbeziehung aller Gradienten vor, kann man mit Hilfe eines Phantomexperiments diese parameterisiert erfassen und somit für verschiedene Protokolle (unterschiedliche Aufnahmeparameter) verwenden.
- Der Segmentierungsprozess zur Generierung eines individuellen Kopfmodells mit mindestens 5 verschiedenen Gewebetypen lässt sich komplett automatisiert durchführen.
- Die Informationen zur Bestimmung des Leitfähigkeitstensors von biologischem Gewebe in-vivo können mit Hilfe von Diffusionstensorbildgebung gewonnen werden.
- Die Verwendung der Richtungsinformationen für den Tensor der spezifischen elektrischen Leitfähigkeit zusammen mit einem künstlich vorgegebenem Grad an Anisotropie, erlauben es den Einfluss der Anisotropie auf das elektrische und magnetische vorwärts Problem als auch auf die inverse Lösung systematisch zu untersuchen.
- Der Einfluss anisotropen Gewebes auf die elektrische vorwärts Lösung hängt sowohl von der Entfernung der Quelle zum Gewebe als auch von deren Orientierung relative zu diesem ab.
- Je höher der Grad der Anisotropie desto stärker ist der Einfluss auf die vorwärts als auch auf die inverse Lösung. Die Stärke des Einflusses hängt jedoch sehr stark von der Position der Quellen im Volumenleiter und damit die Lage zum anisotropen Gewebesegmente ab.
- Zur Verbesserung der Genauigkeit der EEG/MEG Quellenlokalisation müssen anisotrope Kompartimente im Volumenleitermodell berücksichtigt werden, wobei dies besonders für die Anisotropie der weißen Hirnsubstanz gilt.
- Die Verwendung realistischer Kopfmodelle für die EEG/MEG Quellenlokalisation ist bei ausreichend hoher Auflösung in der Genauigkeit den sphärischen Modellen mit konzentrischen Schalen überlegen.
- Die in den individuellen und realistischen FEM-Modellen für das Tiermodell und das Human Modell gewonnenen Erkenntnisse lassen Rückschlüsse auf die zu erwartenden Fehler in anderen Untersuchungen schließen, und können dazu beitragen, das Auftreten systematischer Fehler durch Vernachlässigung der Gewebeanisotropie zu erklären.